



Review

Selected perovskite oxides: Characterization, preparation and photocatalytic properties—A review



Ewelina Grabowska

Department of Environmental Technology, Faculty of Chemistry, University of Gdansk, Wita Stwosza 63, PL80-308 Gdansk, Poland

ARTICLE INFO

Article history:

Received 30 October 2015

Received in revised form

10 December 2015

Accepted 18 December 2015

Available online 22 December 2015

Keywords:

Perovskite oxides

Synthesis

Properties

Surface morphology

Photocatalysis

ABSTRACT

Perovskite-type oxides are a class of compounds with the general formula ABO_3 . They are a very important family of materials and exhibit properties suitable for numerous applications. In this review, the preparation, characterization, and application of selected perovskite oxides such as $SrTiO_3$, $KTaO_3$, $NaTaO_3$, $KNbO_3$, and $NaNbO_3$ in photocatalysis are described. In addition, various strategies for enhancing their photocatalytic activities are discussed, including doping with metals and nonmetals (Cr, Ni, Mn, Pb, Bi, N, Br, S, C, and F), modification with noble metal (Au, Ag, Pt, Pd, Ph, Ru) nanoparticles, and doping with rare earth elements (La). Moreover, the review summarizes the influence of different morphologies and surface properties on the photoactivity of the materials.

© 2015 Elsevier B.V. All rights reserved.

Contents

1. Introduction.....	98
2. Short overview of selected perovskite-oxides groups	98
3. Titanate perovskites: $SrTiO_3$	100
3.1. Pristine $SrTiO_3$	100
3.2. Modified $SrTiO_3$	104
4. Tantalate perovskites: $NaTaO_3$ and $KTaO_3$	106
4.1. Pristine $NaTaO_3$	109
4.2. Modified $NaTaO_3$	110
4.3. Pristine $KTaO_3$	113
4.4. Modified $KTaO_3$	114
5. Niobium perovskites: $NaNbO_3$ and $KNbO_3$	115
5.1. Pristine $NaNbO_3$	115
5.2. Modified $NaNbO_3$	118
5.3. Pristine $KNbO_3$	119
5.4. Modified $KNbO_3$	121
6. Other perovskite-based photocatalysts	122
7. Conclusion and perspectives	122
Acknowledgements	123
References	123

E-mail address: egrab@chem.univ.gda.pl

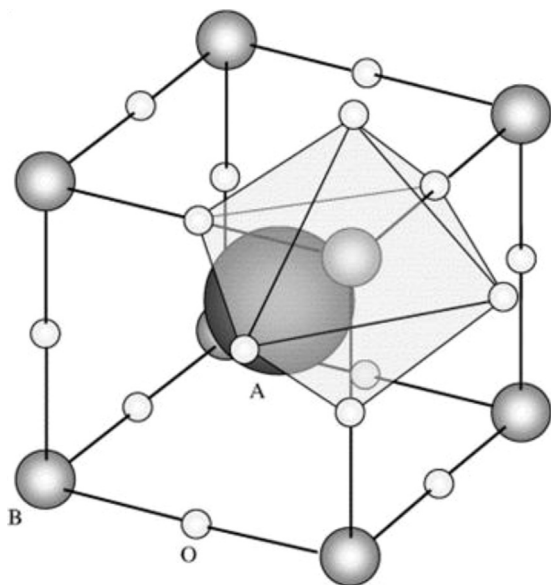


Fig. 1. Structure of perovskite (ABO_3). ●: A-site; ○(grey surface): B-site; ○: oxide ion. Reprinted from Ref. [17].

1. Introduction

Since Fujishima and Honda discovered the photocatalytic splitting of water on TiO_2 electrodes in 1972, photocatalysis using semiconductors has been widely studied [1]. Of these semiconductors, TiO_2 has become the most studied and widely used material, because of its strong oxidation capacity, physical, biological and chemical stability, non-toxicity, and low cost of production [2–10]. However, the drawback of TiO_2 in photocatalysis is that it must be excited by light with a wavelength of less than 388 nm, i.e., only by the UV region, which accounts for only ca. 4% of the intensity of solar radiation, and is inactive in the visible and infrared light regions. This is the main hurdle to its commercialization. Hence, development of visible-light-active TiO_2 has been a major research topic in the past decade, but recently scientists have dedicated more attention to looking for new types of semiconductor photocatalysts for use in the photodegradation of polluting materials [11–16].

Perovskite-type oxides, originated from $CaTiO_3$, are a family of oxides having the general formula ABO_3 (where A is a rare or alkaline earth metal and B is a first row transition metal), wherein cations with a large ionic radius coordinate to 12 oxygen atoms and occupy A-sites and cations with a smaller ionic radius are six-coordinate and occupy B-sites (see Fig. 1) [17]. Because perovskite oxides exhibit a wide range of ferro-, piezo-, and pyroelectric properties and electro-optical effects, they have been used as electronic, structural, magnetic, and refractory materials in numerous technological applications [17,18]. Tanaka and Misono have detailed the advantages of perovskite photocatalysts [17]:

1. They are formed from a wide variety of compositional and constituent elements, but their essential, basic structures are similar.
2. Their bulk structures can be characterized well, and their surface properties can be fairly well extrapolated from the knowledge of their well-defined bulk structures.
3. Their valency, stoichiometry, and vacancy can be varied widely.
4. Much information on their physical and solid-state chemical properties has been accumulated [17].

Several factors affect the photocatalytic performance of the material system under consideration. Electron and hole effective mass, exciton lifetime and diffusion length, and exciton binding

energy all affect electron–hole separation and transport within the lattice. Defects in the lattice, defect-induced energy states, and localization of electrons on specific defect sites determine the fate of the photoexcited electron–hole pair. Moreover, electron transfer across semiconductor–electrolyte interfaces is significantly affected by surface states, surface band structure (depletion region induced electric field), and band bending. Among many photocatalyst materials perovskite oxides have shown excellent promise as efficient photocatalysts under visible-light irradiation, because of their unique crystal structures and electronic properties. The perovskite crystal structure provides a good framework in which to tune the band gap values to enable visible-light absorption and band edge potentials to suit the needs of specific photocatalytic reactions. Furthermore, lattice distortion in perovskite compounds strongly influences the separation of photogenerated charge carriers. Some groups of perovskite materials such as titanate perovskites [19–27], tantalate perovskites [28–34], vanadium- and niobium-based perovskites [35–40], and ferrite perovskites [41–46] have shown visible-light activity.

Recently, there are some review papers related to use perovskite oxides in various fields [47–50]. Shi and Guo reviewed a ABO_3 -based photocatalysts for water splitting. They summarized different modification strategies based on fundamental principle and process of photocatalysis and on the crystal structure and chemical component of perovskites [16]. Zhu et al. reviewed the preparation, characterization, and application of perovskite oxides in heterogeneous catalysis. Catalytic performances of samples with different morphologies for gas, solid, and liquid-phase reactions have been overviewed [51]. Kanhere and Chen prepared a general overview focused on the visible light ($\lambda > 400$ nm) active perovskite-based photocatalyst systems [52]. They divided discussed photocatalysts into two groups: simple ABO_3 type-perovskites and complex perovskites (double, layered, etc.).

The current review is focused on selected groups of perovskites (titanate, tantalate and niobate) with particular emphasis placed on correlation between preparation methods, synthesis conditions or surface properties and photocatalytic activity under UV or visible light irradiation in several typical reactions. Preparation is an important method to obtain materials with desired structure and physicochemical property, while characterization gives the possibility to explore and understand the textural structures and properties of the synthesized photocatalysts. In this regard, this paper gives deep insight into knowledge of synthesis, characterization and application of selected ABO_3 -based photocatalysts. This review is organized in seven sections: (1) a brief introduction to perovskite oxides, (2) short overview of selected perovskite-oxides groups, (3) preparation and characterization of titanates, (4) preparation and characterization of tantalates, (5) preparation and characterization of niobates, (6) other perovskite based-photocatalysts, and (7) conclusions and perspectives.

2. Short overview of selected perovskite-oxides groups

Photocatalysts are semiconductor with a band gap between 1.4 and 3.8 eV [53]. The type, structure and morphology of photocatalysts as well as an effective electric field inducing the separation of photogenerated electron–hole pairs at the interface of the individual semiconductors reduces the probability of electron–hole recombination, are very important properties determining the degradation of organic pollutants.

Since in 1953 Parravano reported that $NaNbO_3$, $KNbO_3$, and $LaFeO_3$ can be used for CO oxidation, the application of perovskite oxides to heterogeneous photocatalysis increased [54,55]. As was mentioned above, an ideal perovskite has cubic crystal structure (space group, $Pm\bar{3}m$, corner-sharing network of BO_6

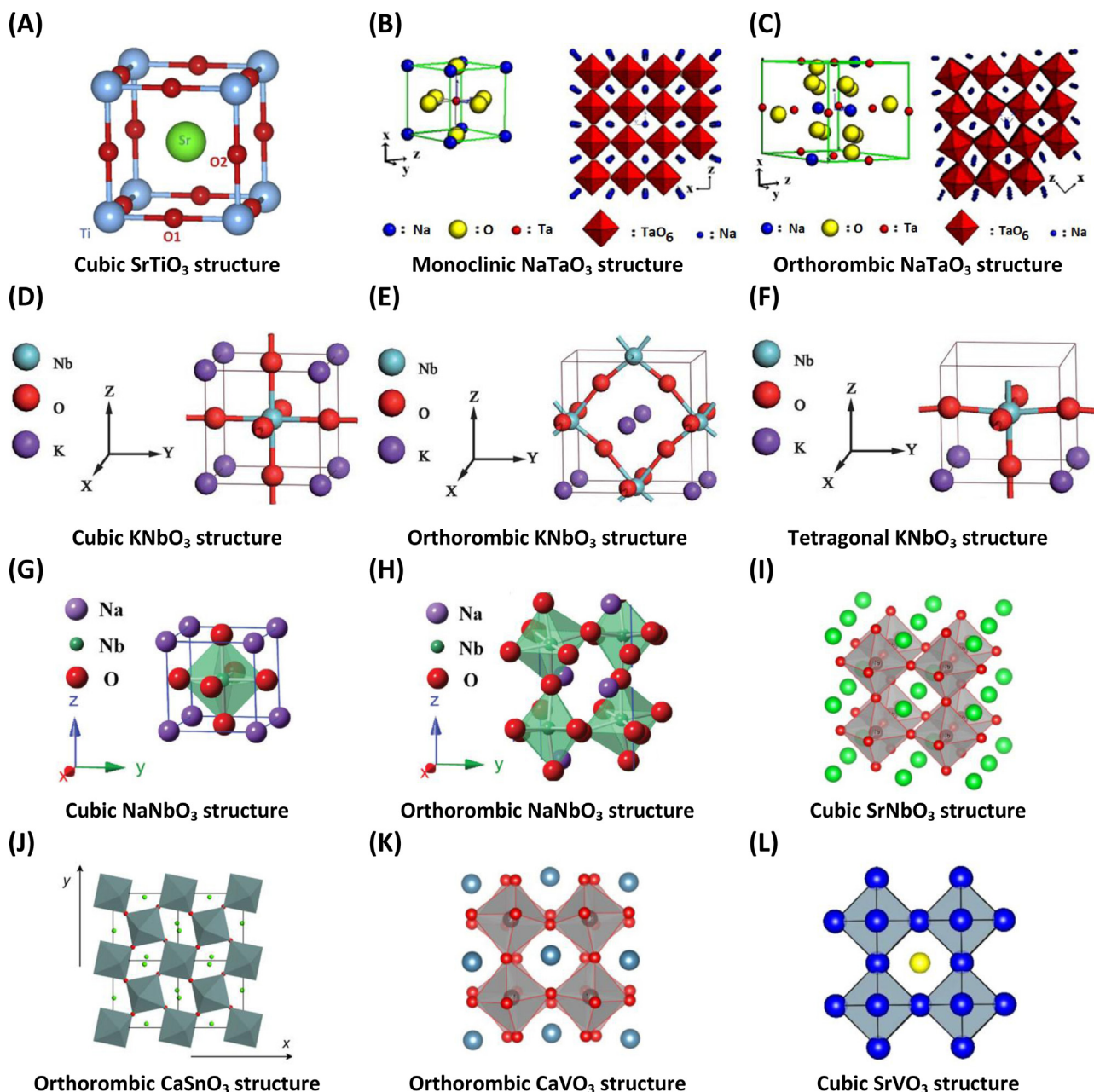


Fig. 2. Crystal structures of selected perovskite oxides: (A) SrTiO_3 [128], (B–C) NaTaO_3 [110], (D–F) KNbO_3 [112], (G–H) NaNbO_3 [129], (I) SrNbO_3 [130], (J) CaSnO_3 [127], (K) CaVO_3 [130], (L) SrVO_3 [56].

octahedra, with the B ion in its center, the A ion positioned on a dodecahedral site in the middle of the cube), shown in Fig. 1. However, the real perovskite ABO_3 exhibited lattice distortion to varying degrees (octahedra are tilted around its center), thereby resulting in the transformation of crystal phases in the following sequences: orthogonal, rhombohedral, tetragonal, monoclinic, and triclinic phase, depending on the details of the octahedral rotations (selected structures presented at Fig. 2) [16]. Moreover, it is well known that, rotations of the oxygen octahedra has important impact on crystal field and thus changes the dipole and electronic band structures, thereby influencing the behaviors of photogenerated charge carriers, including excitation, transfer, and redox reaction, in whole photocatalytic process [16]. This is due to the fact that the octahedral rotations influence the B–O bond length and B–O–B angle due to the shift of the oxygen ions from the edges of the cubic perovskite structure [56].

The structure, size and potential applications of perovskite oxides materials are strongly influenced by the synthesis process; therefore a lot of research is aimed both at its processing and application. The development of innovative processing methods through chemistry permits one to lower the preparation temperature and to improve homogeneity and reproducibility of the products for the synthesis of ultrafine and chemically pure powders of mixed-metal oxides. Most of the perovskite photocatalysts are still prepared by conventional solid state reactions where particles are typically on a micron scale, which limits their commercial applications due to lower light absorption in the visible region and short lifetimes of the excited states [57–60]. As an alternative route, several methods have been reported for the synthesis of perovskite oxides, such as: combustion synthesis [61–63], sol–gel method [64–68], thermal decomposition of bimetallic compound [69], sonochemical method [70–72], microemulsion method [73–76], polymerizable

complex method [77], the polyvinyl alcohol (PVA) route [78], electrospinning method [79], co-precipitation method [39,80–84], microwave-assisted method [85–88]. Among the various methods, hydrothermal method is a facile dominant tool for the synthesis of anisotropic nanoscale material. Significant advantages of this method are controlled size, low temperature growth, cost effectiveness and less complicated [28,42,89–94].

AVO₃ oxides were reported for most of the divalent elements as A-cation [95]. For alkali-earth elements (except Mg) their structures are three-dimensional frameworks consisting of corner-shared, regular or slightly distorted, VO₆ octahedra. Among them, extensive attention was focused on silver vanadium oxides nanomaterials due to their potential applications in photocatalysis [39,93,96]. For vanadium oxides the unique hybridized valence bands (V 3d, O 2p, and Ag 4d orbitals) lead to a narrow band gap and highly dispersed valence bands. For, example, α -AgVO₃ and β -AgVO₃ possess an intense absorption band in the visible light region (band gap 2.3–2.5 eV), which make it a potential application as visible-light-sensitive photocatalyst. Iron-based semiconductors (AFeO₃), such as BiFeO₃, LaFeO₃, YFeO₃ etc., have also drawn increasing attention in recent years as a narrow band gaps visible-light photocatalysts [86,97]. There are many evidences for the photocatalytic activity of LaFeO₃, but, there are a few reports about photoactivity of remaining AFeO₃ photocatalysts, so investigation of iron-based rare earth perovskites and impact of particular rare earth metal on electronic and photocatalytic properties of ferrites is necessary. Perovskite alkaline earth stannate with ASnO₃ (A = Ca, Sr and Ba) general formulae has very interesting properties. Among them, SrSnO₃ has been applied as a photocatalyst material [60,84,87,91]. This effective photocatalytic activity can be attributed to the spatial structure of SrSnO₃, in which the three-dimensional network of corner-sharing SnO₆ octahedra can help charge carriers to move more easily and the octahedral tilting distortion has a positive effect on local charge separation [84].

Because of the structural features, designing of perovskite-type oxides gives a possibility to use almost 90% of the metallic natural elements of the periodic table and offer the way to correlate solid state chemistry to photocatalytic properties. Table 1 presents list of selected groups of perovskite oxides, which can be used as a potential photoactive nanomaterials, taking into account their band gap energy and crystal structure. Many of them are still unexamined during photocatalytic processes.

3. Titanate perovskites: SrTiO₃

Titanate perovskites ATiO₃ (A = Ca, Sr, Ba, etc.) are wide bandgap semiconductor materials with interesting electronic, optical, magnetic and photocatalytic properties, which have been studied for photocatalytic applications for a long time. Moreover, as reported by Alammari et al., titanate perovskites are promising materials for photocatalytic processes because of their excellent resistance to photocorrosion and high thermal stability [131]. The solid-state reaction of ACO₃ and TiO₂ above 900 °C is a typical method to obtain ATiO₃ samples. However, one disadvantage of this method is that the obtained products contain agglomerated particles of different sizes and morphologies, as well as impurities owing to incomplete reaction [132]. Therefore, the challenge here is to develop new methods to prepare well-defined ATiO₃ photocatalysts of controlled size and shape.

3.1. Pristine SrTiO₃

SrTiO₃ is a well-known simple cubic perovskite (*Pm3m*, *a* = 3.9 Å) with an indirect band gap of 3.1–3.7 eV [98,133]. Moreover, strontium titanate has been widely studied as an important *n*-type

semiconductor because of its variety of outstanding physical properties (stability, wavelength response, and current–voltage response), and has found use in a variety of practical applications such as oxide electronics [134,135], H₂ production [136], solar cells [137], and resistive O₂ gas sensors [138,139]. Furthermore, it is a promising candidate for an efficient photocatalyst [140–144]. Based on the total density of states (DOS) it is known that the bands of SrTiO₃ are classified into three parts: (i) the lower-energy side consisted of O 2s + Sr 5p + Ti 4p + Ti 4s hybrid orbitals, (ii) the middle part of the bands, which is, corresponding to the valence band (VB), consists of O 2p + Sr 5s + Ti 3d hybrid orbitals and (iii) the bottom of the CB formed by the Ti 3d orbital. Thus, the highest occupied and the lowest unoccupied molecular orbital levels are composed of the hybrid orbitals of O 2p + Sr 5s + Ti 3d and the Ti 3d orbitals, respectively [145].

All these properties depend on its crystal structure and morphology; therefore, there are many synthesis methods to obtain pure and doped SrTiO₃, including the sol–gel method [146–148], hydrothermal synthesis [149–152], the polymeric precursor method [153–156], the solid-state reaction [157], and the micro-emulsion method [158,159]. A summary of preparation methods related to the photoactivity of photocatalyst is shown in Table 2.

Zheng et al. proposed a simple alkali hydrothermal synthesis to obtain hollow SrTiO₃ microspheres with diameters in the range of 3–5 μm from an anatase TiO₂ microsphere precursor, and investigated its photocatalytic activity in the photoreduction of Cr(VI) [160]. TiO₂ microspheres obtained in the first synthesis step were mixed with the appropriate amount of SrCl₂ and deionized water, which was then purged with N₂ gas. Then, NaOH was added to the solutions, followed by hydrothermal treatment at 180 °C in a Teflon autoclave for 6 h. Based on SEM analysis, Zheng et al. confirmed that the SrTiO₃ microspheres had a hollow structure, and the shell thickness was estimated to be ca. 0.7 μm. Moreover, higher-magnification SEM and TEM analyses revealed that the hollow microspheres are assembled by regular SrTiO₃ nanocubes with an edge length of 70 ± 10 nm. To investigate the possible formation mechanism of SrTiO₃ and its crystallinity, samples were obtained using different reaction times (0.5, 1, 2, and 6 h). Using XRD analysis, Zheng et al. observed that the degree of crystallization of the products increased with increasing reaction time. The hydrothermal synthesis duration also had an impact on the morphology and particle size. The average size of the SrTiO₃ nanoparticles increased from 30 through 50–70 nm with increasing synthesis time from 0.5 h through 3 h to 6 h. Simultaneously, the shape of the nanoparticles changed from sphere-like to regular nanocubes. A plausible growth mechanism was suggested, consisting of the following steps (see Fig. 3A):

- Ti–O–Ti bonds in the TiO₂ precursor are broken to form Ti–O–Na,
- Sodium titanate on the surface of the microspheres reacts with strontium ions to form SrTiO₃ nanoparticles leading to the formation of a thin layer of SrTiO₃ on the surface of the microsphere precursor.
- Strontium ions diffuse inward through the SrTiO₃ shell to its inner surface, while the titanate ions diffuse outward through the SrTiO₃ shell to its outer surface [160].

Hollow SrTiO₃ microspheres exhibit photocatalytic activity in the photoreduction of Cr(VI). After 120 min of irradiation, 90% of the Cr(VI) was reduced in the presence of SrTiO₃ microspheres. The photoactivity of the obtained samples can be explained by their intense absorption in the UV region, as hollow structures provide more efficient light harvesting [160].

The growth mechanisms of SrTiO₃ nanostructures were also explored by Dong et al. [161]. To synthesized porous SrTiO₃

Table 1
Compilation of promising and potential perovskite-oxides photocatalysts.

Perovskite-type oxides ABO ₃		Band gap (eV)	Crystal structure	Ref.
BO ₃	A			
(A)TiO ₃	SrTiO ₃	3.1–3.7	Cubic	[98]
	BaTiO ₃	3.0–3.3	Cubic	[24]
	CaTiO ₃	3.6	Cubic or orthorhombic	[99]
	MnTiO ₃	3.1	Rhombohedral	[100]
	CoTiO ₃	2.28	Rhombohedral	[101]
	FeTiO ₃	2.8	Rhombohedral	[102]
	PbTiO ₃	2.75	Tetragonal	[103]
	CdTiO ₃	2.8	Rhombohedral	[52,104]
	NiTiO ₃	2.18	Rhombohedral	[26,105]
	ZnTiO ₃	2.87–3.7	Cubic, hexagonal, rhombohedral	[106–108]
(A)TaO ₃	KTaO ₃	3.4–3.6	Cubic or orthorhombic	[33]
	NaTaO ₃	4.2	Orthorhombic, monoclinic, cubic	[109,110]
	AgTaO ₃	3.4	Rhombohedral	[28]
	LiTaO ₃	4.7	Cubic or rhombohedral	[111]
(A)NbO ₃	KNbO ₃	3.14–3.24	Cubic, orthorhombic, rhombohedral, tetragonal	[112]
	NaNbO ₃	3.0–3.5	Cubic, tetragonal, orthorhombic	[113]
	AgNbO ₃	2.7	Orthorhombic	[52], Li
	CuNbO ₃	2.0	Monoclinic	[52]
	LiNbO ₃	3.78	Rhombohedral	[53,114]
	SrNbO ₃	2.79	Cubic	[115,116]
(A)VO ₃	α-AgVO ₃	2.5	Monoclinic	[39,117]
	β-AgVO ₃	2.3	Monoclinic	[39,96]
	PbVO ₃	2.93	Cubic	[118]
	SrVO ₃	3.22	Cubic	[118]
	CaVO ₃	no data	Cubic	[119]
	BaVO ₃	3.2	Cubic	[118]
	LaVO ₃	0.9–1.2	Orthorhombic	[56]
	YVO ₃	1.6	Orthorhombic	[120]
(A)FeO ₃	LaFeO ₃	2.1	Cubic or orthorhombic	[42,70]
	BiFeO ₃	2.0–2.7	Rhombohedral	[97]
	GaFeO ₃	2.7	Orthorhombic	[65]
	YFeO ₃	2.43	Orthorhombic	[86]
	PrFeO ₃	2.08	Orthorhombic	[66]
	AlFeO ₃	2.1	Orthorhombic	[82]
(A)BiO ₃	LiBiO ₃	1.63	Orthorhombic	[89,90]
	NaBiO ₃	2.53	Trigonal	[89,121]
	KBiO ₃	2.04	Cubic	[89,90]
	AgBiO ₃	2.5	Trigonal	[122]
(A)NiO ₃	BiNiO ₃	0.73–1.96	Triclinic, orthorhombic	[123,124]
	LaNiO ₃	2.26–2.51	Cubic, rhombohedral	[63,73]
(A)SbO ₃	AgSbO ₃	2.6	Cubic	[125]
(A)SnO ₃	SrSnO ₃	4.1	Orthorhombic	[91]
	BaSnO ₃	3.0	Cubic	[126]
	CaSnO ₃	3.8–4.96	Hexagonal, rhombohedral, orthorhombic	[127]

nanostructure, appropriate amount of SrCl₂, NaOH and titanate nanotube were placed in autoclave (hydrothermal conditions: 160; 200 and 240 °C; 1; 3; 12 and 24 h). They observed that the form of the Ti precursor, i.e., nanotube or nanowire, influences the morphology of the SrTiO₃ microstructure (see Fig. 3B). Nanotube@SrTiO₃ hetero-nanostructures appeared during the quick nucleation process of the titanate nanotubes used as a precursor. However, when a long titanate nanowire precursor was used, the dissolved Ti source supplied the nucleation and growth of SrTiO₃ more slowly, and hence, it aggregated more gradually to form a solid sphere. On this basis, it can be concluded that when a titanate nanotube precursor is used during the synthesis, the porosity of the obtained material is improved through the effective separation of nucleation and growth stages [161]. Dong et al. synthesized porous and solid SrTiO₃ spheres using a free-template hydrothermal method, with titanate nanotubes or nanowires and SrCl₂ as precursors. They reported that the morphology and pore size of the obtained samples were controlled by the reaction conditions, including reaction time and reaction temperature. After 1,

3, 12, and 24 h of treatment, the particles were 150, 200, 100–300, and 200 nm in diameter, respectively [161]. Furthermore, the effect of temperature was studied at 160, 200, and 240 °C during 24 h hydrothermal treatments. At 160 °C, the surfaces of the spheres were smooth, but at 200 °C the prepared spheres had rough surfaces. When the reaction temperature was increased to 240 °C, the SrTiO₃ spheres cracked, which may have contributed to the splitting of the porous structure at high temperatures. The photocatalytic activity of the porous SrTiO₃ spheres was evaluated in the degradation of rhodamine B (RhB) under UV illumination (λ = 254 nm). After 20 min of irradiation, 100% of RhB was degraded in the presence of porous SrTiO₃ spheres [161].

It is well known that the activity of heterogeneous catalysts is influenced by their crystal phase, size, surface area, and crystallinity. Thus, control of the size and shape of SrTiO₃ structures is critically important for evaluating their shape-dependent photoreactivity and developing SrTiO₃-based high-performance photocatalysts. Huang et al. reported the precise control of SrTiO₃ nanoparticle morphology in basic aqueous solutions under differ-

Table 2
Recent publications (2010–2015) of synthesis methods and characteristics of SrTiO₃ based-photocatalyst.

SrTiO ₃ based-photocatalysts						
SrTiO ₃ precursor	Doping moiety	Synthesis parameters	Model photocatalytic reaction	Experimental conditions	Photocatalytic activity	Ref.
TiO ₂ sph, SrCl ₂	–	Procedure: hydrothermal method, 180 °C, 6 h 0.5 g anatase TiO ₂ microspheres, 1.67 g SrCl ₂ , 50 cm ³ H ₂ O, 2 g NaOH Drying: 40 °C	Photoreduction of Cr (VI)	0.1 g of photocatalyst were dispersed in glass reactor containing 100 cm ³ of K ₂ Cr ₂ O ₇ solutions (C ₀ = 30 mg/dm ³) Irradiation source: 300 W Xe arc lamp	After 120 min of irradiation 90% of Cr(VI) was reduced in the presence of SrTiO ₃ microspheres	[160]
TiO ₂ NT or NW, SrCl ₂	–	Procedure: hydrothermal method, 160; 200 and 240 °C; 1; 3; 12 and 24 h 10 cm ³ of SrCl ₂ saturated solution, NaOH and titanate nanotubes or nanowires were placed in the Teflon-lined vessel	Photodegradation of rhodamine B (RhB)	0.03 g of SrTiO ₃ was added into 30 cm ³ of RhB (C ₀ = 2 × 10 ^{−5} mol/dm ³) Irradiation source: UV illumination, λ > 254 nm	After 20 min of irradiation 100% RhB was degraded in the presence of porous SrTiO ₃ spheres	[161]
P25-TiO ₂ Sr(OH) ₂ ·8H ₂ O	–	Procedure: hydrothermal method, 100; 130; 150 and 180 °C, 24; 48; 72 and 96 h 0.1 g P25-TiO ₂ and 10 cm ³ NaOH (1, 3, 5, and 10 M) was added to 0.35 g Sr(OH) ₂ ·8H ₂ O	Photodegradation of crystal violet (CV)	0.25–1 g/dm ³ STO powder was added into 100 cm ³ of CV, pH 5; 7 and 9 Irradiation source: C-75Chromato-Vue cabinet of UVP	0.5 g/dm ³ was selected as the optimum amount of photocatalyst. Photodegradation rate of the CV dye was found to increase with the increase in the value of pH The synthesis conditions at 3 M NaOH, reaction time 72 h, and hydrothermal temperature 130 °C of STO are the optimum photocatalysts	[162]
H ₂ TiO ₃ Sr(NO ₃) ₂	–	Procedure: solvothermal synthesis, 150 °C, 5 h KOH was dissolved into the mixture solutions with different volume ratios of EtOH: H ₂ O–1:1, 1:2, 100% EtOH, and 100% H ₂ O. Then 0.44 g Sr(NO ₃) ₂ and 0.2 g H ₂ TiO ₃ were put into four KOH solutions Drying: 80 °C, 2 h	Photodegradation of methyl blue (MB)	0.0125 g of the SrTiO ₃ was added into 25 cm ³ of MB (C ₀ = 200 mg/dm ³) Irradiation source: 6 W UV lamp with a main emission peak at 254 nm	SrTiO ₃ synthesized with the volume ratio of EtOH: H ₂ O of 1:1 has the highest photoactivity. Dye was degraded in 91% after 3 h of irradiation. With the increasing of the water content, the degradation percentage of methyl blue decreased	[132]
TiB ₂ , Sr(NO ₃) ₂	Cr, B	Procedure: hydrothermal process, 200 °C, 24 or 72 h Sr(NO ₃) ₂ (0.005 mol), Cr(NO ₃) ₃ ·9H ₂ O (0.00025 mol), and TiB ₂ (0.00475 mol) were added to autoclave and mixed with 50 cm ³ of water. After stirring for 5 min, 6 g NaOH was added. The autoclave was stirred another 2 h. after the hydrothermal treatment precipitate was dried at 80 °C overnight	Hydrogen production	Photocatalytic reactions for H ₂ evolution were conducted over the Pt-loaded photocatalyst using CH ₃ OH as the sacrificial reagent. The Pt-loaded photocatalyst powders (0.25 g) were dispersed in the aqueous CH ₃ OH solution (50 cm ³ of CH ₃ OH + 220 cm ³ of H ₂ O) Irradiation source: 300 W Xe arc lamp (20 A input current) λ ≥ 420 nm	H ₂ generation rate for Cr,B-codoped SrTiO ₃ was 15.4 μmol/h	[142]
Ti(OC ₃ H ₇) ₄ , Sr(NO ₃) ₂	N	Procedure: solvothermal synthesis, 200 °C, 3 h TIP was dissolved in 2-propanol and 0.2 mol/dm ³ Sr(NO ₃) ₂ was added. Next hexamethylenetetramine (HMT) (5; 10; 15 and 20 g) and KOH were added and solution was heated at 90 °C for 1 h and placed in the autoclave	Photodegradation of methyl orange (MO)	0.1 g of the N-doped SrTiO ₃ was added into 100 cm ³ of MO (C ₀ = 0.05 g/dm ³) Irradiation source: type 40 W mercury lamp and xenon lamp λ > 290 or 400 nm	The photocatalytic activity changed depending on the amount of the hexamethylenetetramine (HMT) dosage. Sample SrTiO _{3-x} N _y with 15 g of HMT showed the highest photocatalytic activity under visible light irradiation and exhibited very stable photocatalytic activity under visible light irradiation after five cycles	[150]
Ti(OC ₃ H ₇) ₄ , Sr(NO ₃) ₂	Au	Acetylacetone and tetraisopropyl orthotitanate was mixed and added to laurylamine hydrochloride solution. 4.23 g of Sr(NO ₃) ₂ was added to LAHC solution and mixed with 0.07 g of HAuCl ₄ ·3H ₂ O LAHC/Sr(NO ₃) ₂ /HAuCl ₄ ·3H ₂ O solution was slowly dropped into the ACA/TIPT Calcination: 700 °C, 4 h	Photocatalytic hydrogen production	0.2 g of photocatalyst was suspended in an aqueous solution containing different concentrations (0–8 vol.%) of hole scavenger (methanol, formic acid, acetic acid, propanoic acid, hydrochloric acid, and sulfuric acid) and irradiated for 5 h Irradiation source: 176 W Hg lamps (Phillip Co., Ltd.)	2.5 vol.% aqueous formic acid solution system exhibited the highest specific hydrogen production rate of 647 μmol h ^{−1} g _{cat} ^{−1}	[180]
TiO ₂ Sr(OH) ₂ ·8H ₂ O	Rh, Sb	Procedure: hydrothermal method, 160 °C, 40 h Sr(OH) ₂ ·8H ₂ O, TiO ₂ , Rh(NO ₃) ₃ and Sb ₂ O ₅ was added to an autoclave and heated. Obtained precursor was washed and dried at 60 °C for 1 day. Powder was calcined at 1000 °C for 10 h	H ₂ and O ₂ evolution	0.05–0.2 g of photocatalyst was dispersed in the reactant solution (H ₂ evolution from an aqueous methanol solution (10 vol%), O ₂ evolution from an aqueous silver nitrate solution (0.02 mol/dm ³) Irradiation source: 300-W Xe lamp	The highest H ₂ evolution activity was obtained for SrTiO ₃ doped with only rhodium (Sb/Rh = 0) Loading of IrO _x cocatalyst improved the photocatalytic activity of SrTiO ₃ :Rh/Sb for the O ₂ evolution	[181]



Fig. 3. Possible mechanism formation of: (A) SrTiO₃ hollow microspheres proposed by Zheng et al. Reprinted from ref. [160], (B) SrTiO₃ proposed by Dong et al. Reprinted from Ref. [161].

ent reaction conditions, including NaOH concentration, reaction time, and temperature [162].

SrTiO₃ was prepared using NaOH concentrations of 1, 3, and 5 M. P25-TiO₂, Sr(OH)₂·8H₂O and NaOH were used as the starting material. Chen and Chen had already reported a possible mechanism for the formation of SrTiO₃ by hydrothermal synthesis based on the dissolution-precipitation method, in which there was a chemical equilibrium between TiO₂ and Ti(OH)_x^{4-x} [163]. Based on this research, Huang et al. reported an increase in the particle size of SrTiO₃ with an increase in the NaOH concentration, which was in accord with the dissolution-precipitation mechanism [162]. They explained that Ti(OH)_x^{4-x} – a highly active species – could react with Sr²⁺ to form a new nucleus. Additionally, an increase in NaOH concentration increased the possibility of forming a new Ti(OH)_x^{4-x} nucleus, which led to an increase in the SrTiO₃ particle size. It was reported that the phase formation of cubic SrTiO₃ depended on the NaOH concentration, because agglomeration of strontium titanate nanoparticles at higher NaOH concentration promoted the growth of the cubic phase [162]. The next step in investigating the formation of crystalline SrTiO₃ nanoparticles was to elucidate the effect of synthesis time at a constant NaOH concentration and temperature. Thus, the synthesis was performed with reaction times ranging from 24 to 96 h at 130 °C with a NaOH concentration of 3 M. XRD analysis confirmed the cubic phase of SrTiO₃ and indicated that when SrTiO₃ was treated for 24–96 h, a new peak assigned to SrCO₃ appeared, but was not observed after synthesis for 96 h. Using SEM analysis, Huang et al. observed differences in crystal size at 24 and 96 h, which could be attributed to the Ostwald ripening process of the precursor SrTiO₃(H₂O)_x. Smaller particles were less stable, and the growth of larger particles was energetically favorable. The crystal size was dependent on extending the processing time. At the early stage of the reaction, hydroxide ions produced more nuclei and formed smaller particles, which grew larger with prolonged reaction time. The photoactivity of the obtained samples was investigated by the degradation of crystal violet dye under UV light irradiation. SrTiO₃ produced using 3 M NaOH, a reaction time of 72 h, and a hydrothermal temperature of 130 °C was found to have optimized photocatalytic activity [162].

Based on literature data, it can be concluded that mesoporous-structured photocatalysts possess higher photocatalytic activity and better light-induced hydrophilicity than non-porous-

structured photocatalysts [164–166]. The porosity of mesoporous photocatalysts can be controlled during synthesis via the sol-gel method by using a structure-directing surfactant [165,167,168]. Puangpetch et al. obtained mesoporous SrTiO₃ nanocrystals with uniform particle size using the sol-gel method in the presence of a structure-directing surfactant [169]. Sr(NO₃)₂ and tetraisopropyl orthotitanate (TIPT) were used as strontium and titanium precursors. They assayed laurylamine hydrochloride (LAHC), cetyltrimethylammonium bromide (CTAB), and cetyltrimethylammonium chloride (CTAC) as surfactants, and used strontium nitrate (Sr(NO₃)₂) and tetraisopropyl orthotitanate (TIPT) as the SrTiO₃ precursors. Anhydrous ethanol (EtOH), ethylene glycol (EG), or EtOH/EG was selected as the solvent in which the surfactant was dissolved. XRD analysis showed that SrTiO₃ obtained in the presence of EG contained a small impurity of SrCO₃, while the use of an EtOH/EG mixture resulted in very low SrCO₃ contamination. The sample with the highest purity was synthesized when EtOH was used, but this sample had a slightly lower crystallinity than that prepared using EG. XRD diffractograms revealed that SrTiO₃ synthesized using LAHC as a structure-directing surfactant showed significantly higher purity and crystallinity than those prepared using CTAB or CTAC, and showed no SrCO₃ peaks. The pore size distribution and surface area of the synthesized SrTiO₃ photocatalysts could be controlled by the adjustment of the LAHC/TIPT molar ratio. The morphologies of the SrTiO₃ photocatalyst synthesized under the optimum conditions (EtOH as a solvent, LAHC as a structure-directing surfactant, a heating rate of 1 °C min⁻¹, and an LAHC/TIPT molar ratio of 0.25:1) were investigated using TEM analysis. An increase in the calcination temperature from 600 to 700 °C resulted in a slight decrease in particle size [169]. The same samples were selected to measure photocatalytic activity under UV irradiation using methyl orange (MO) as a model contaminant. Photoactivity reached its maximum, i.e., complete degradation of MO in 3 h, in the presence of mesoporous SrTiO₃ nanocrystals calcined at 700 °C. Puangpetch et al. reported that photocatalytic activity also depended on the LAHC/TIPT molar ratio, exhibiting the highest photocatalytic activity at a ratio of 0.25:1 [169].

Based on these results, it can be concluded that the photocatalytic activity of SrTiO₃ depends on specific surface area and crystallinity, because smaller particles have a superior ability to absorb light and also tend to provide lower opportunity for bulk

electron–hole recombination. Therefore, the synthesis conditions (mainly calcination temperature) should be optimized to achieve a good balance between the specific surface area and crystallinity of the photocatalysts.

Wang et al. proposed an inexpensive and simple solvothermal method to prepare strontium titanate using metatitanic acid (H_2TiO_3) and $\text{Sr}(\text{NO}_3)_2$ as a starting materials [132]. They also explained the influence of the EtOH to water volume ratio on the crystal growth of SrTiO_3 nanocrystals. The XRD patterns showed that when EtOH alone was used as the solvent, no SrTiO_3 peak was detected, while single-phase SrTiO_3 was observed when the solvent contained water. In addition, the size of the SrTiO_3 nanocrystals depended on the EtOH to water volume ratios. The nanoparticles changed in size from a diameter of 20–30 nm through 40–50 nm to 70 nm when the EtOH:H₂O (v/v) was 1:1, 1:2, and 0:1, respectively. This can be explained by the fact that water accelerates dissolution-recrystallization during the Ostwald ripening process, and thus results in increased crystal size [132]. Photocatalytic activity was investigated under UV light irradiation using methyl blue (MB) as a model pollutant. SrTiO_3 synthesized using an EtOH:H₂O ratio of 1:1 had the highest photoactivity, with 91% of the dye being degraded in 3 h of irradiation. With increasing water content, the degradation percentage of MB decreased, which may be related to the larger size of nanoparticles produced, and, thus, to their lower specific surface area [132].

Chen et al. prepared a series of SrTiO_3 photocatalysts via the sol–gel method to degrade nitrogen oxides (NO_x) [170]. To the mixture of strontium nitrate, citric acid (molar ratio = 1.5/1) and butyl titanate (Sr/Ti molar ratio = 1) glycol was dropped as stabilizer. Obtained sol was dried (60 °C, 6 h) and calcined at 600–800 °C for 4 h. The elimination of NO was determined under UV light or sunshine by measuring the concentration of NO gas. Strontium nitrate and butyl titanate were used as precursors, and glycol was employed as a stabilizer. XRD peaks, which increased in intensity with increasing calcination temperature (600–800 °C), confirmed that all samples consisted of single-phase SrTiO_3 , i.e., a perovskite-type structure with cubic symmetry. Calcination temperature also influenced the particle size and distribution. Only the sample calcined at 700 °C contained regular and well-dispersed particles, while SrTiO_3 calcined at 600 °C consisted of uneven particles. SrTiO_3 powders calcined at 700 °C revealed the highest photocatalytic activity. After 45 min of UV irradiation, 92% of NO_x was converted into NO. Unfortunately, light conditions affect the photoreduction of NO_x , with SrTiO_3 under UV light exhibiting better photoactivity than under solar light [170].

Concluding, SrTiO_3 is also an important *n*-type semiconductor with a basic framework of Ti–O polyhedron as TiO_2 which can be used as a promising candidate for efficient photocatalysts. Especially, the porous SrTiO_3 nanostructure, combined the shape-specific and the porous natures, lead to collective functions to improve the photocatalytic activity. The conventional way of synthesizing SrTiO_3 is based on the solid-state reaction (temperatures higher than 900 °C), which not only consumes high energy for its preparation but also does not permit a high degree of control and reproducibility of properties required for the photocatalysis application. Therefore, it would be highly desirable for developing a general approach to fabricate SrTiO_3 with controllable crystal structure, surface area, morphology (shape and size), as well as porosity and pore size distribution.

3.2. Modified SrTiO_3

Wide spectrum of modification methods, such as doping (via chemical and route) or deposition of noble metals on the semiconductor surface, have been reported to enhance the utilization of solar light for wide band gap semiconductors. In this review by the

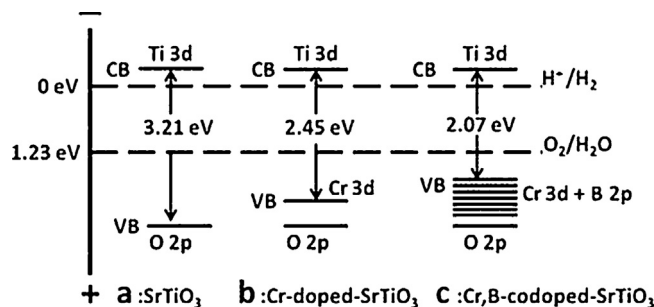


Fig. 4. The electronic band structures for (a) SrTiO_3 , (b) Cr-doped- SrTiO_3 , and (c) Cr,B-codoped SrTiO_3 . Reprinted from Ref. [142].

“modified perovskite-oxide” the author will understand both of the above mentioned methods which will be explained in detail.

The most commonly used is element doping because of the simplicity and low cost of the process. Based on literature data, it can be concluded that the change in electronic band structures proceeds in two different ways:

1. The formation of a new mid-gap state between the valence band (VB) and conduction band (CB), as seen in Rh-, Cr-, Ir-, and Ru-doped materials [20,142,171–173].
2. Changing the VB or CB through the mixing of energy levels of the dopant and host elements, as seen in N-, F-, C-, and S-doped materials [174–178].

Yu et al. synthesized SrTiO_3 photocatalysts codoped with Cr and B by a one-step hydrothermal method using TiB_2 , $\text{Sr}(\text{NO}_3)_2$, and $\text{Cr}(\text{NO}_3)_3 \cdot 9\text{H}_2\text{O}$ as precursors [142]. During the synthesis, the autoclave with appropriate amount of precursors was heated to 200 °C and maintained for 24 h or 72 h. Previous studies have reported that the visible-light response of Cr^{3+} -doped SrTiO_3 results from the formation of a new mid-gap state, which is about 1.0 eV higher than the VB maximum in SrTiO_3 [179]. XRD analysis confirmed the presence of cubic SrTiO_3 in all samples, and TiB_2 impurities in the sample synthesized for 24 h. This fact indicated that TiB_2 might directly transform into SrTiO_3 , eliminating the need to process TiO_2 as an intermediate phase. Based on the XPS results, Yu et al. reported that B atoms were incorporated into SrTiO_3 rather than existing in a separate TiB_2 or B_2O_3 phase, i.e., that B was directly substituted for O in the crystal lattice of SrTiO_3 , and that Cr^{3+} was incorporated into the Ti sites in SrTiO_3 . The B/Cr-codoped SrTiO_3 exhibited visible-light absorption, proving that Cr and B codoping had a synergetic effect on the SrTiO_3 band gap. Yu et al. calculated that the band gap for the codoped SrTiO_3 is 2.07 eV, while for Cr-doped SrTiO_3 , B-doped SrTiO_3 , and pure SrTiO_3 it is 2.45 eV, 3.18 eV, and 3.21 eV, respectively. They proposed a schematic for the electronic band structures of the obtained samples, as shown in Fig. 4. Evaluation of photocatalytic activity was measured in the hydrogen production process under visible light irradiation using a 300 W Xe arc lamp ($\lambda \geq 420$ nm). The Cr/B-codoped SrTiO_3 photocatalyst exhibited higher photocatalytic activity for hydrogen production than the Cr-doped SrTiO_3 sample. The H_2 generation rates for Cr/B-codoped SrTiO_3 and Cr-doped SrTiO_3 were 15.4 $\mu\text{mol/h}$ and 9.3 $\mu\text{mol/h}$, respectively. It is well known that defects and oxygen vacancies are usually regarded as recombination centers. It was shown that B doping was responsible for the formation of Ti^{3+} , which is not beneficial for photocatalytic water splitting, but introducing Cr^{3+} into the Ti sites in the B-doped SrTiO_3 decreased the content of Ti^{3+} [142].

Ohno et al. prepared S/C cation-codoped strontium titanium dioxide by the calcination of a mixture of thiourea and SrTiO_3 powders at 400, 500, or 600 °C under aerated conditions for 3 h [174].

All the prepared photocatalysts had a perovskite phase in which C and S atoms were incorporated into the SrTiO_3 structure, as confirmed by XRD and FT-IR spectroscopy. XPS measurements revealed the appearance of two broad peaks attributed to S 2p at around 168 and 165.7 eV, which were assigned to S^{4+} and S^{2+} ions, respectively, and two broad peaks attributed to the C 1s binding energy observed at 284 and 288 eV. UV-vis spectra of S/C cation-codoped and pure SrTiO_3 showed that the absorption edges of the codoped samples shifted to the visible-light region from 400 to 700 nm. It was also indicated that the absorption properties depended on the calcination temperature used during synthesis. The absorption in the visible region decreased with increasing annealing temperature. The absorption spectrum of doped SrTiO_3 calcined at 600 °C was almost the same as that of pure SrTiO_3 . Photocatalytic properties under UV and visible light were studied in the photodegradation of 2-propanol. The suspension was irradiated by a 500 W Xe lamp. To limit the irradiation wavelength, the light beam was passed through filters to cut off wavelengths shorter than 340, 420, 440, 500, and 540 nm. Of all the synthesized samples, doped SrTiO_3 calcined at 500 °C showed the highest photocatalytic activity. Moreover, under visible-light irradiation ($\lambda > 440$ nm) only S/C cation-codoped SrTiO_3 powders showed activity, while pure SrTiO_3 was inactive under visible light irradiation. Samples calcined at 500 °C showed higher photoactivity than the samples calcined at 400 °C under photoirradiation at wavelengths longer than 440 nm. It can be observed that, despite the fact that the sample calcined at 400 °C had the highest absorption in the visible-light region, the sample calcined at 500 °C showed higher activity. Ohno et al. suggested that this phenomenon was due to the incorporation of larger amounts of S and C cations into the crystal lattice of SrTiO_3 , which induces larger distortion of its crystal lattice, thus decreasing its photocatalytic activity [174].

Based on literature reports that suggested that the electrical properties of titanate ceramics can be improved by doping with fluorine, Wang et al. prepared F-doped SrTiO_3 powders by a mechanochemical reaction method [177,178]. Strontium titanate was synthesized by the solid-state reaction of SrCO_3 and TiO_2 at 1100 °C for 2 h, and strontium fluoride (SrF_2), lithium fluoride (LiF), and polytetrafluoroethylene (PTFE) were used as dopant sources. To obtain F- SrTiO_3 powders, SrTiO_3 and each reagent were put in a zirconia pot together with zirconia balls and milled for different times. The XRD results showed that all the SrTiO_3 -based photocatalysts had a perovskite-type structure having cubic symmetry [177]. XPS analysis was performed to confirm that F was doped into the SrTiO_3 lattice. Wang et al. calculated the concentration of F in various F-doped SrTiO_3 samples from the XPS peak areas. They observed that fluorine had been doped into the SrTiO_3 lattice, and that SrF_2 was a more effective fluorine dopant than PTFE. TEM studies showed that the particle size of pure SrTiO_3 was in the range of ca. 0.2–0.5 μm diameter, while F-doped samples comprised two fractions of particles: spherical nanoparticles of ca. 20 nm and larger particles in the size range of 0.1–0.2 μm . The photocatalytic activity in the oxidative decomposition of nitrogen monoxide was determined by measuring the concentration of NO gas at the outlet of a reactor using a 450 W high-pressure mercury arc as the light source. The light beam was passed through filters to cut off wavelengths shorter than 290 or 400 nm. Under visible light, the highest photocatalytic ability was observed for the sample prepared with SrF_2 as the doping source. In the presence of SrTiO_3 - SrF_2 and pure SrTiO_3 , ca. 43% and 14% NO was decomposed, respectively. All of the F-doped SrTiO_3 samples showed high photocatalytic activity under UV light ($\lambda > 290$ nm). It was found that 60% of NO was degraded in the presence of SrTiO_3 - SrF_2 , which was about 50% and 20% higher than pure SrTiO_3 and a commercial TiO_2 catalyst (P-25), respectively [177]. The diffuse reflectance spectra showed that an absorption edge is located at 390 nm for SrTiO_3 ,

which is related to a band gap energy of 3.18 eV. Such a large value of the band gap could be responsible for lower photocatalytic activity under visible light. It was observed that for samples prepared with SrF_2 and SrF_2 with LiF, the absorption edge was shifted by 21 nm and 15 nm, respectively, and the band gap energies were 3.02 eV (411 nm) and 3.06 eV (405 nm), respectively. Thus, it was concluded that F-doping shifted the absorption edge of SrTiO_3 to the visible-light range and narrowed its band gap [177].

To improve the visible-light photocatalytic properties of SrTiO_3 - SrF_2 , Wang et al. investigated the influences of milling time, F-dopant content, and post-grinding heat treatment temperature [178]. SrTiO_3 - SrF_2 samples were prepared with different molar amounts of SrF_2 , i.e., 1, 2, 3, 5, 8, and 10 mol%. The photoactivity was measured under irradiation of light with $\lambda > 290$, > 400 , and > 510 nm. Photocatalytic activity increased with increasing SrF_2 amount up to 5 mol%, and then started to decrease. Wang et al. explained that the photocatalytic activity of F-doped samples might be due to the formation of Ti^{3+} ions, which leads to high visible-light absorption capability in the photocatalysts. Moreover, the substitution of lattice O by F led to a decrease in the amount of lattice O. It was suggested that doping with F species might cause an increase in the effective electron mobility, resulting in an easier transfer of photogenerated electrons in $\text{SrTiO}_{3-x}\text{F}_x$ from the interior of the grains to their surfaces [178]. The influence of heat treatment on photocatalytic activity was also investigated. Samples were heated to 150, 200, 300, and 400 °C. Wang et al. reported that grinding resulted in the formation of defects in the sample that could become electron-hole recombination centers. Conversely, heat treatment reduced the number of hydroxyl groups on the surface of the photocatalyst, and hydroxyl groups easily reacted with holes to form peroxides, which could also become recombination centers [178]. Photoelectrons generated in the CB of SrTiO_3 react with molecular oxygen to form $\bullet\text{O}_2^-$, and generate highly active $\bullet\text{OOH}$ radicals. Wang et al. reported that NO reacts with these reactive O radicals, holes, O_2 , and water, to produce HNO_2 and HNO_3 . Because of the fact that higher temperatures led to the growth of the grains, decrease in specific surface area, and loss of F in the sample, the optimum temperature for the photoactivity was found to be in the range 150–200 °C. NO elimination activity was also dependent on the grinding time (10, 60, 120, 180, and 240 min) of the samples during synthesis. The highest photocatalytic activity was observed for the sample with the highest specific surface area, which was prepared by grinding a mixture of 5 mol% SrF_2 - SrTiO_3 for 60 min. Results indicated that a long grinding time (240 min) decreases the specific surface area, which in turn decreases the photoactivity, because a larger specific surface area improves the adsorption of NO. It can be concluded that the sample prepared by grinding 5 mol% SrF_2 and 95 mol% SrTiO_3 for 1 h followed by heat treatment at 150 °C for 2 h showed ca. three times higher photocatalytic activity for the oxidative decomposition of NO under irradiation with visible light ($\lambda > 510$ nm) than that shown by pure SrTiO_3 [178].

Mechanochemical synthesis has also been shown to be an efficient method to obtain nitrogen and lanthanum co-doping SrTiO_3 [176]. $(\text{NH}_2)_2\text{CO}$ and La_2O_3 were used as N and La sources, respectively. All precursors were put in the crucible and heated at 600 °C or were charged in zirconia pot and ball-milled for 2 h. Wang et al. reported that La^{3+} has nearly the same ionic radius (0.115 nm) as Sr^{2+} (0.113 nm), and can thus replace Sr^{2+} in SrTiO_3 without causing high lattice strain. Samples were prepared in two different ways: by the heating method and by the mechanochemical reaction method. All obtained samples consisted of perovskite-type SrTiO_3 . Samples synthesized by mechanochemical means had a crystallite size of 20.2 nm. Based on TEM analysis, it was observed that samples obtained via the heating method consisted of relatively large particles of about 0.2–0.4 μm in diameter, while samples obtained by the mechanochemical reaction consisted of spherical particles of

two different sizes—tiny particles of *ca.* 20 nm and large particles of *ca.* 100–200 nm. XPS analysis was used to confirm that both N and La were incorporated into the SrTiO₃ lattice. In both methods, N was incorporated into the SrTiO₃ lattice. However, there were differences in the shape of the La 3d peak depending on the preparation method. Compared with the La 3d peak from pure La₂O₃, the peak shape from the sample prepared by the mechanochemical reaction changed, while the sample prepared by the heating method exhibited a La 3d peak shape similar to that of pure La₂O₃. Wang et al. concluded that the mechanochemical reaction is an efficient method to prepare samples where the SrTiO₃ lattice is codoped with N and La, whereas heating at 600 °C could only be used for doping with N [176]. Pure SrTiO₃ with a band gap energy of 3.17 eV has an absorption edge at 390 nm. Diffuse reflection spectra of codoped samples showed that they had two absorption edges at 390 and 450 nm, which may be attributed to those of pure SrTiO₃ and N-doped SrTiO₃, respectively, while the mixture of SrTiO₃ and La₂O₃ exhibited only one absorption edge at 390 nm. Based on this analysis, it can be concluded that La-doping increases the N-doping content, which is very beneficial due to the fact that N-doping generates an absorption edge in the visible-light range, and results in the improvement of NO photo-oxidation activity under visible light. Undoped SrTiO₃ exhibited little photocatalytic activity in the NO degradation process under visible light ($\lambda > 400$ nm). The sample prepared by the mechanochemical reaction using 77.8 mol% SrTiO₃, 22.0 mol% (NH₂)₂CO, and 0.2 mol% La₂O₃ showed the highest photoactivity under UV ($\lambda > 290$ nm) and visible light ($\lambda > 400$ nm), with 63.2% and 35.8% NO degradation, respectively [176].

Konta et al. obtained SrTiO₃ samples doped with Mn, Ru, Rh, Pd, Ir, and Pt ions [20]. SrCO₃ and TiO₂ powders were used as strontium titanate precursors. Samples were obtained by the calcination of a mixture of SrCO₃ and TiO₂ with appropriate metal precursors, such as: MnO₂, RuO₂, Rh₂O₃, PdO, IrO₂ and PtO₂ (900–1300 °C for 5–25 h). XRD analysis confirmed that a SrTiO₃ phase was present in all samples, but peaks assigned to metallic Pd were observed in SrTiO₃:Pd(0.5%). Konta et al. reported that doping with Pd²⁺ is difficult because the ion radius of Pd²⁺ (0.86 Å) is larger than that of Ti⁴⁺ (0.605 Å). SrTiO₃:M(0.5%) (where M = Mn, Ru, Rh, Pd, Ir, or Pt) samples showed that the absorption edges shifted to the visible light region. Additionally, it was reported that SrTiO₃:Rh powder exhibited two absorption bands: one around 420 nm and the second around 580–1000 nm, which can be attributed to the existence of two different oxidation states of doped Rh: Rh³⁺ and Rh⁵⁺. The photocatalytic activity was measured in H₂ evolution from an aqueous methanol solution and O₂ evolution from an aqueous silver nitrate solution under visible light. It was observed that only Ru-, Rh-, and Ir-doped SrTiO₃ were active for H₂ evolution, and Mn- and Ru-doped SrTiO₃ for O₂ evolution. The highest activity in H₂ evolution (17.2 $\mu\text{mol h}^{-1}$) was exhibited by SrTiO₃:Rh(0.5%); therefore, the optimum preparation condition was examined. Konta et al. prepared SrTiO₃:Rh(*x*) samples (where *x* = 0.1%, 0.5%, 1%, 2%, or 3%) and found that SrTiO₃:Rh(1%) showed the highest activity in H₂ evolution. Subsequently, the influence of the calcination conditions on SrTiO₃:Rh(1%) was examined. The results demonstrated that the optimum preparation temperature for SrTiO₃:Rh(1%) was 1000 °C for 10 h. The maximum rate of H₂ evolution was 90 $\mu\text{mol h}^{-1}$ [20].

A mesoporous Au-loaded (1 wt%) SrTiO₃ photocatalyst was synthesized via a sol-gel process by Puangpetch et al. [180]. Sr(NO₃)₂ and tetraisopropyl orthotitanate (TIPT) were used as strontium and titanium precursors, laurylamine (LAHC) was used as a structure-directing surfactant and hydrogen tetrachloroaurate (III) trihydrate (HAuCl₄·3H₂O) as a gold source. XRD analysis confirmed the cubic phase of SrTiO₃ with high purity and high crystallinity. Additionally, no peaks of Au were detected probably because of the low Au concentration and the well-dispersed Au NPs on the SrTiO₃ matrix. Based on the TEM images Puangpetch et al. observed that syn-

thesized SrTiO₃ nanoparticles were in the approximate range of 25–40 nm and the Au particle size was found to be in the approximate range of 10–15 nm. N₂ adsorption-desorption isotherms confirmed that synthesized photocatalyst had very narrow pore size distribution indicating an advantage of the investigated sol-gel process in obtaining a good-quality product with a controlled porosity. The photoactivity of Au-SrTiO₃ was estimated by measuring H₂ production via photocatalytic water splitting under UV irradiation. Puangpetch et al. investigated the effects of the molecular structure and chemical properties of hole scavengers used during the photocatalytic process on the efficiency of hydrogen production. The hole scavengers were classified into three categories: positive-effect hole scavengers (formic acid), negative-effect hole scavengers (propanoic acid), and non-affecting hole scavengers (methanol and acetic acid), and employed in a concentration range of 0–8 vol%. Photocatalytic water splitting process was found to depend on the molecular structure, chemical properties, and concentration of the investigated hole scavengers in the order: water < formic acid \cong methanol < acetic acid < propanoic acid. Without the addition of any hole scavenger, the hydrogen production rate in the presence of 1 wt% Au-SrTiO₃ was 468 $\mu\text{mol h}^{-1} \text{ g}_{\text{cat}}^{-1}$. In the presence of formic acid at 2.5 vol% hydrogen production increased to 647 $\mu\text{mol h}^{-1} \text{ g}_{\text{cat}}^{-1}$. It was formic acid, which is the smallest and completely-dissociated water-soluble carboxylic acid, exhibited the highest hydrogen production enhancement ability [180].

Summarizing, SrTiO₃ only responds to UV light because of its relatively large band gap (3.2 eV), which greatly restricts its energy conversion efficiency. For the purpose of improving the SrTiO₃ photocatalytic efficiency, the most popular approach is to modify the energy band structure of SrTiO₃ to shift its optical absorption edge from the UV region to the visible light region. Doping foreign elements (S, C, F, N, La, or both N and La, Rh, Sb etc.) into a semiconductor with wide band gap to create a new optical absorption edge is known to be one of the primary strategies for developing visible light-driven photocatalysts. Additionally, an effective technique to retard the rate of the recombination reaction between photo-generated electrons and holes in SrTiO₃ was the loading of noble and transition metal (Au, Pt). Consequently, the preparation of fine particles of small band gap semiconductor with high crystallinity is desired to obtain visible light active photocatalysts.

4. Tantalate perovskites: NaTaO₃ and KTaO₃

The high photocatalytic activity of tantalates (ATaO₃, A = Na, K, Ag, Li) is most often attributed to their suitable CB level, consisting of Ta_{5d}, and the efficient carrier delocalization caused by the proper distortion of TaO₆ connections [110,182,183]. These factors are associated with the crystalline structure, which can be synthesis route-dependent. Until recently, popular methods of obtaining tantalates were the solid-state reaction (SSR) [182,184–187] and polymerized complex (PC) method [188,189]. However, in solid-state synthesis, it is difficult to control crystallinity and particle size, localized segregation of components, and stoichiometry because of high temperatures. In order to achieve better photocatalytic performance, tantalate-based photocatalysts are currently more commonly synthesized by methods such as templating [190], sol-gel synthesis [191], hydrothermal synthesis [192,193], and the hydrothermal-electrochemical method [194]. Of all the tantalate perovskites, NaTaO₃ and KTaO₃ are the most efficient photocatalysts; however, work on the development of UV-vis- and visible-light-driven KTaO₃-based photocatalysts is uncommon. A brief summary of recent publications on NaTaO₃ and KTaO₃ photocatalysts is provided in Table 3.

Table 3
Recent publications (2010–2015) of synthesis methods and characteristics of NaTaO₃ and KTaO₃ based-photocatalysts.

NaTaO ₃ based-photocatalysts						
NaTaO ₃ precursor	Doping moiety	Synthesis parameters	Model photocatalytic reaction	Experimental conditions	Photocatalytic activity	Ref.
Ta ₂ O ₅	S	Procedure: hydrothermal method, 180 °C, 12 h 0.442 g of Ta ₂ O ₅ , 1.2 g of NaOH and certain amount of Na ₂ S ₂ O ₃ ·5H ₂ O were mixed with water and added to an autoclave. After hydrothermal processing washed with deionized water and dried at 80 °C for 2 h	Photodegradation of methyl orange (MO) and phenol	0.001 g of S-NaTaO ₃ or pure NaTaO ₃ was added into 10 cm ³ of MO or phenol aqueous solution (C ₀ = 20 mg/dm ³) Irradiation source: UV —light-low pressure mercury lamp 8 W, Philips, visible light-high pressure mercury lamp (250 W, Philips) with suitable cutoff filters ($\lambda < 420$ nm)	S-doped NaTaO ₃ exhibits superior visible-light photocatalytic activity for the degradation of MO ((0.306 h ⁻¹) After irradiated for 8 h about 60% of phenol was degraded in the presence of S doped NaTaO ₃	[213]
Ta ₂ O ₅	N	Procedure: hydrothermal method, 550–1000 °C, 12 h Mixture of Ta ₂ O ₅ and NaOH (molar ratio 1:2) was heated in an autoclave. Obtained NaTaO ₃ was mixed with C ₃ H ₆ N ₆ and was heated at 270 °C for 3 h	Photodegradation of methyl blue (MB)	0.1 g of N-NaTaO ₃ was added into 100 cm ³ of MB aqueous solution (C ₀ = 20 mg/dm ³) Irradiation source: 250 W high pressure mercury lamp (Philips)	NaTaO _{2.961} N _{0.039} showed the highest photodegradation rate for MB solution (complete decolorization of MB in less than 40 min)	[206]
Ta ₂ O ₅	N	Procedure: hydrothermal method, 160, 180, 200 °C, 12 h Mixture of Ta ₂ O ₅ , NaOH, and NH ₃ ·H ₂ O was heated an autoclave	Photodegradation of methyl orange (MO)	0.06–0.14 g of N-NaTaO ₃ was added into 100 cm ³ of MO aqueous solution (C ₀ = 20 mg/dm ³) Irradiation source: 250 W high pressure mercury lamp (Philips) $\lambda > 400$ nm	Complete decolorization of MO aqueous solution was achieved over 100 mg/100 cm ³ loading of N-doped NaTaO ₃ at the pH 4.0 within 14 h irradiation	[209]
Ta ₂ O ₅	N	Procedure: hydrothermal method, 160, 180, 200 °C, 3; 6; 9 and 12 h 0.441 g of Ta ₂ O ₅ , 1.2 g of NaOH and 200 μ l of NH ₃ ·H ₂ O were heated in an autoclave	Photodegradation of methyl blue (MB)	0.1 g of N-NaTaO ₃ was added into 100 cm ³ of MB aqueous solution (C ₀ = 20 mg/dm ³) Irradiation source: 250 W high pressure mercury lamp	Sample obtained at 180 °C had the highest photoactivity: about 100% of MB was degraded after irradiation for 40 min and 5 h under UV and vis light irradiation, respectively	[208]
Ta ₂ O ₅	Bi	Procedure: solid-state reaction Ta ₂ O ₅ , Bi ₂ O ₃ and Na ₂ CO ₃ (different synthesis conditions: mildly Na-rich, strongly Na-rich, Na-deficient) were mixed then pressed into pellets, and heated at 900 °C for 10 h, then washed with deionized water and dried in air in 100 °C	Photodegradation of methyl blue (MB)	0.025 g of Bi-NaTaO ₃ was added into 50 cm ³ of MB aqueous solution (C ₀ = 20 mg/dm ³) Irradiation source: 300 W, $\lambda > 420$ nm	Correlation between photoactivity and synthesis route can be presented as follows: mildly Na-rich > strongly Na-rich > Na-deficient	[202]
Ta ₂ O ₅	La	Procedure: hydrothermal method, 160 °C, 24 h La(NO ₃) ₃ , NaOH and Ta ₂ O ₅ were mixed according to the ratio Na:La:Ta = 1 – X:X:1 (X = 0, 1, 2, 3, 4, 5% mol, respectively) added to an autoclave and heated	Photodegradation of safranin T (ST)	0.1 g of La-NaTaO ₃ was added into 100 cm ³ of ST aqueous solution (C ₀ = 10 mg/dm ³) Irradiation source: 10 W UV-light lamp	The highest degradation rate of ST dye was achieved when the amount lanthanum doped was 2 mol%. 90% of dye was degraded after 2 h of irradiation	[203]
Ta ₂ O ₅	Au, La	La-NaTaO ₃ Procedure: solid-state reaction Na ₂ CO ₃ , Ta ₂ O ₅ , La ₂ O ₃ were mixed and calcined at 897 °C for 1 h and 1147 °C for 10 h Au/NaTaO ₃ :La Procedure: photodeposition method Photodeposition of Au was carried out using an aqueous solution containing a certain amount of HAuCl ₄ , <i>in situ</i> , during the photocatalytic reaction Procedure: impregnation method Aqueous HAuCl ₄ solution was mixed with NaTaO ₃ :La powder and treated with H ₂ at 100–300 °C for 1–2 h	H ₂ and O ₂ evolution (water splitting process)	0.3–0.5 g Au/NaTaO ₃ :La powder was dispersed in water (350 cm ³). Irradiation source: 400-W high-pressure Hg lamp (SEN; HL400EH-5)	NaTaO ₃ :La loaded with Au by an impregnation method showed higher and more steady activity for water splitting than that by a photodeposition method	[217]
Ta ₂ O ₅	Ag	NaTaO ₃ Procedure: hydrothermal method, 140 °C, 12 h 0.60 g of NaOH, 0.221 g of Ta ₂ O ₅ and 20 cm ³ water was heated in an autoclave Ag-NaTaO ₃ Procedure: photodeposition method NaTaO ₃ was added into 25 cm ³ of an AgNO ₃ solution and irradiated by 500 W Xe lamp for 1 h. The molar ratios of Ag: Ta = 0.2, 0.6, 1 and 1.4	Photodegradation of rhodamine B (Rh B)	0.1 g of Ag-NaTaO ₃ was added into 100 cm ³ of RhB aqueous solution (C ₀ = 10 mg/dm ³) Irradiation source: 300 W Xe lamp $\lambda > 425$ nm	The highest photoactivity was observed for Ag-NaTaO ₃ sample at the nominal atomic ratio of silver to tantalum as 0.6 ($k_{RhB} = 0.56$ h ⁻¹), which is more than 3 times that of pure NaTaO ₃ ($k_{RhB} = 0.20$ h ⁻¹)	[219]

Table 3 Continued.

KaTaO ₃ based-photocatalysts						
KaTaO ₃ precursor	Doping moiety	Synthesis parameters	Model photocatalytic reaction	Experimental conditions	Photocatalytic activity	Ref.
Ta ₂ O ₅	–	Procedure: hydrothermal method, 200 °C, 24 h KTaO ₃ : 30 g of KOH, 11 g of Ta ₂ O ₅ and 3 cm ³ of PEG-400 were dissolved in 60 cm ³ H ₂ O. The solution was stirred about 1 h and transferred to autoclave KTaO ₃ + CdSe + SrTiO ₃ ; KTaO ₃ + CdS + WO ₃ ; KTaO ₃ + CdS + MoS ₂ : One-pot synthesis rout—all reagents in specified molar ratio of products were mixed, transferred into autoclave and thermally treated. In two-step hydrothermal reaction, solution containing appropriate semiconductor precursors was mixed with previously synthesized KTaO ₃	Photodegradation of toluene	Suspension photocatalyst (about 0.1 g) in water was loaded as a thick film on a glass plate. TiO ₂ -coated support was then placed at the bottom side of the photoreactor (V = 30 cm ³) equipped with a quartz window. The concentration of toluene in a gas mixture was about 200 ppm Irradiation source: 25 UV LEDs (λ_{max} = 375 nm, 63 mW per diode)	The highest photoactivity was observed for the KTaO ₃ + CdS + MoS ₂ (10:5:1) sample obtained via two-steps preparation route. After 60-min of irradiation about 60% of toluene was degraded	[33]
Ta ₂ O ₅	–	Procedure: hydrothermal method, 200 °C, 24 h KTaO ₃ : 30 g of KOH, 11 g of Ta ₂ O ₅ and 3 cm ³ of PEG-400 were dissolved in 60 cm ³ H ₂ O. The solution was stirred about 1 h and transferred to autoclave KTaO ₃ –CdS, KTaO ₃ –MoS ₂ and KTaO ₃ –CdS–MoS ₂ : Calcination method—powder mixture of KTaO ₃ and CdS or/and MoS ₂ were mixed together and calcined at 500 °C for 3 h Hydro/solvothermal method: required amounts of solutions were mixed together, stirred and heated in the autoclave at 200 °C for 24 h	Photodegradation of toluene and phenol	Suspension photocatalyst (about 0.1 g) in water was loaded as a thick film on a glass plate. TiO ₂ -coated support was then placed at the bottom side of the photoreactor (V = 30 cm ³) equipped with a quartz window. The concentration of toluene in a gas mixture was about 200 ppm Irradiation source: 25 UV LEDs (λ_{max} = 375 nm, 63 mW per diode) 125 mg of photocatalyst was added into 25 cm ³ of phenol aqueous solution (C ₀ = 500 mg/dm ³) Irradiation source: 1000 W Xenon lamp, $\lambda > 420$ nm	Toluene degradation: In the presence of KTaO ₃ 64% of toluene was degraded after 60 min Phenol degradation: In the presence of KTaO ₃ –CdS = 10:1 about 59% of phenol was degraded under UV–vis light, while under vis light irradiation in the presence of KTaO ₃ –CdS–MoS ₂ 10-5-1—about 42% after 60 min of irradiation	[220]
Ta ₂ O ₅	La	Procedure: hydrothermal method, 200 °C, 24 h KOH and La(NO ₃) ₃ and Ta ₂ O ₅ were dissolved in 17 cm ³ deionized water, to obtained K _{1-x} La _x TaO ₃ (x = 0, 0.02, 0.04, 0.06, 0.08, 0.10) samples and added to an autoclave	Photodegradation of methyl orange (MO)	0.025 g of La–KTaO ₃ or pure KTaO ₃ was added into 50 cm ³ of MO (C ₀ = 2 × 10 ⁻⁵ M) Irradiation source: UV light—300 W Hg lamp	The highest photocatalytic activity was observed for K _{0.08} La _x TaO ₃	[34]

4.1. Pristine NaTaO₃

Compared to other kinds of perovskite-like photocatalysts, NaTaO₃ attracts more attention due to its stable, layered structure and excellent charge-separation effectiveness, which promote the efficiency of photoelectrochemical and photocatalytic systems [110,195–198].

At room temperature, the NaTaO₃ is orthorhombic, with space group *Pcmn* [109]. The Ta cation is 6-fold coordinated with six oxygen anions, forming a tilt octahedral, where Na cations are located in the central position among these octahedral. The calculated lattice constants are $a = 5.428 \text{ \AA}$, $b = 5.510 \text{ \AA}$, and $c = 7.750 \text{ \AA}$ [109,199]. Additionally, on the basis of the data documented in the powder diffraction files of the JCPDS monoclinic NaTaO₃ materials had space group *P2₁/m* with $a = 3.8995 \text{ \AA}$, $b = 3.8965 \text{ \AA}$ and $c = 3.8995 \text{ \AA}$, which is close to that of the cubic phase (*Pm3 \bar{m}* with $a = b = c = 3.929 \text{ \AA}$) [110].

However, NaTaO₃ is not active under visible-light irradiation because the VB of NaTaO₃ predominantly consists of O_{2p} orbitals whose potential energy levels are located at a deep position of about 3 V versus a normal hydrogen electrode (NHE) [200]. For NaTaO₃ the bands with the lowest energy between -15.74 and -17.68 eV are mainly the contribution of O 2s, Ta 6s and Ta 5d. The valence bands lying between -5.60 eV and the Fermi level are mainly due to O 2p states hybridized with Ta 5d, so there is a covalent bond between the O and the Ta and finally, the conduction bands are mainly the contribution of Na 3s, 3p and Ta 5d, 6p and O 2p [201]. In order to narrow the band gap of NaTaO₃ and utilize visible-light irradiation, doping with species such as Bi, Cu, N, Fe, La, Sm, RuO₂, and LaFeO₃ has been studied [30,186,187,202–210]. These studies reported that both anion and cation doping is useful for visible-light photocatalytic applications. Because electronic structure calculations have become an indispensable tool for understanding the band structure of a photocatalytic material, Han et al. performed a computational study on anionic (N, F, P, Cl, and S) doping, and reported that anions like N and P may be beneficial for visible-light absorption [211]. Also, Kanhere et al. investigated the effect of anionic dopants N, C, and I; cationic dopants Cu, V, W, Ti, Zn, In, Sn, Sb, La, and Ce; and codopants N–W, N–I, Pb–I, La–C, Sn–Cu, W–Ti, and Ce–W on the band structure of NaTaO₃ using density functional theory (DFT)-based calculations [32]. They confirmed that N doping can reduce the value of the band gap enough to absorb visible light. Moreover, they reported that doping with C and Cu at the Na site, Cu at the Ta site, and codoping with N–W and Pb–I increased the photocatalytic activity under visible light. DFT was also used by Wang et al. to calculate the electronic structure of anionic N-, P-, C-, or S-doped NaTaO₃ [199]. They noticed that N and S shifted the VB edge of the material upward without affecting its ability to split water into H₂ and O₂.

Hu et al. investigated the influence of the synthesis method (sol–gel or solid-state) on the structure and photoactivity of NaTaO₃ [110]. In the sol–gel synthesis sodium acetate (CH₃COONa), tantalum chloride (TaCl₅), and hydrated citric acid (C₆H₈O₇·H₂O) were used as the starting materials. Prepared gel with a Na/Ta/citric acid molar ratio of 1/1/5 was calcined at 350 °C for 1 h and 500 °C for 3 h. In the solid-state method sodium carbonate (Na₂CO₃) and tantalum oxide (Ta₂O₅) were mixed with Na in 5% excess and was calcined at 1200 °C for 10 h. Using SEM analysis, they observed that samples synthesized by the sol–gel method (here on designated as SG) had irregular surface morphology with a size of 30–50 nm, while samples obtained by solid-state (here on designated as SS) were cube-like with a size of 2–3 μm . Their photocatalytic activity was measured in the water-splitting reaction. H₂ evolution was much greater with SG (2050 $\mu\text{mol h}^{-1} \text{ g}^{-1}$) than with SS (13 $\mu\text{mol h}^{-1} \text{ g}^{-1}$). The high photoactivity of SG samples was explained by the fact that the SG samples had a larger surface area than the SS sam-

ples, and therefore, the surface of SG was more active than that of SS. Additionally, Lin et al. calculated the band structure and density of states in monoclinic and orthorhombic NaTaO₃ [212]. They concluded that their difference in photoactivity was associated with their gap transition type. Monoclinic SG and orthorhombic SS have indirect and direct bandgaps, respectively. There are two reasons why monoclinic NaTaO₃ is better for applications in photocatalytic reactions. Firstly, because phonons are involved in the gap transition the recombination rate for the photo-induced electron–hole pairs is smaller than that in orthorhombic NaTaO₃. Secondly, the monoclinic phase has a larger number of effective states available for the photo-induced electrons and holes [110].

The influence of reaction temperature and time, as well as alkali concentration, on the morphology of the photocatalysts was investigated by Li et al. [192]. It is known that the concentration of alkali solution used during the hydrothermal process, is a crucial parameter to obtain well crystallized samples. NaTaO₃ nanocubes were prepared using NaOH concentration of 0.25; 0.50 and 0.75 M and Ta₂O₅. Based on the XRD patterns Li et al. noticed that when the concentration of NaOH was 0.25 M only the Ta₂O₅ phase was detected. Diffraction peaks of the raw Ta₂O₅ were still observed when the concentration increased to 0.5 M and pure orthorhombic NaTaO₃ structure was assigned when the NaOH concentration was 0.75 M. Li et al. explained that higher NaOH concentration lead to form alkaline hydroxylated Ta–O ionic groups which are the building blocks for NaTaO₃. To determine the influence of hydrothermal temperatures for NaTaO₃ formation, the precursor suspension was heated for 12 h at different temperatures from 60 to 140 °C (NaOH = 0.75 M). The XRD patterns confirmed that NaTaO₃ did not form when the reaction temperature was as low as 60 °C. When the temperature was increased to 120 °C Ta₂O₅ phase started to decrease. Pure NaTaO₃ was obtained at 140 °C. It can be concluded that under high temperature and pressure Ta₂O₅ powders can be partly dissolved and hydroxylated (Ta–O covalent bond in Ta₂O₅ was broken) to form hydroxylated Ta–O ionic groups. In the final step NaTaO₃ samples were synthesized at 140 °C with 0.75 M NaOH solution for various reaction times—3; 6; 9 and 12 h. When the reaction time was less than 3 h only diffraction peaks attributed to Ta₂O₅ were observed. A well crystallized NaTaO₃ phase was formed when the reaction time reached 12 h. Additionally, based on the SEM images, Liu et al. noticed that after 6 h of hydrothermal treatment NaTaO₃ nanocubes start to emerge and when the reaction time was extended to 12 h NaTaO₃ nanocubes with the size of 200–400 nm were synthesized. The photocatalytic activity of obtained samples was measured as the decomposition rate of Safranin T solution and gaseous formaldehyde under UV irradiation. After 60 min of irradiation in the presence of NaTaO₃ nanocubes prepared at 140 °C Safranin T was completely degraded. The degradation process of formaldehyde over the NaTaO₃ nanocubes showed that photocatalysts synthesized at different temperatures shows similar photocatalytic activity [192].

The influence of NaOH concentration on formation of NaTaO₃ with cubic morphology during hydrothermal process (120 °C, 12 h) was also reported by He et al. [197]. Ta₂O₅ and NaOH were used as a starting materials. They observed that pure NaTaO₃ was obtained at 120 °C for 12 h when the NaOH concentration was about 0.5 M. TEM analysis showed that obtained NaTaO₃ was in the form of well crystallized cubic morphology with the particle size of about 200 nm. He et al. explained that during the hydrothermal treatment, Ta₂O₅ dissolves into the solution and then reacts with the NaOH and form NaTaO₃ particles which increases with the time. The E_g of the obtained NaTaO₃ was estimated to be about 3.96 eV. The photoactivity was measured during gaseous formaldehyde and rhodamine B (RB) solution degradation under UV light irradiation. In both cases NaTaO₃ photocatalysts showed a relatively high activ-

ity. Formaldehyde and rhodamine (B) was decomposed over 30 min and 3.5 h of UV light irradiation, respectively [197].

In conclusion, NaTaO₃ photocatalyst has gained significant attention as one of the most efficient photocatalytic material systems e.g. for stoichiometric water splitting under UV irradiation because it possesses conduction band consisting of a Ta 5d orbital at a more negative position than that of titanates (Ti 3d). This property suggests that NaTaO₃ is photoactive material with good photophysical properties. It is known that preparation method and conditions largely affect the photocatalytic activity. Traditionally, NaTaO₃ is produced from high temperature solid state reactions which has many disadvantages such as inhomogeneous product and lack of control over crystallinity and particle sizes, which results in a change in the photocatalytic activity of catalyst. Since excellent photocatalyst always requires homogeneous and high-purity, an alternative synthesis procedure such as hydrothermal or sol-gel method were proposed.

4.2. Modified NaTaO₃

As discussed in the previous paragraph, S-doping can shift the VB edge of NaTaO₃ upward by 1.35 eV because S has the same valence electrons as O, meaning that the substitution of S into the O sites would not introduce undesirable holes or defects into the NaTaO₃ structure [199]. Based on this fact, Li et al. obtained a S-doped NaTaO₃ photocatalyst by the hydrothermal method [213]. Ta₂O₅, NaOH and certain amount of Na₂S₂O₃·5H₂O were added into autoclave and heated at 180 °C for 12 h. SEM analysis confirmed that the obtained structures were nanocubic with sizes between 200 and 500 nm. XRD patterns revealed that all reflection peaks originated from pure, monoclinic NaTaO₃, but it was also observed that, with increasing amount of S, the monoclinic NaTaO₃ altered in structure toward a cubic phase. This tendency can be explained by the fact that the radius of S²⁻ (1.84 Å) is much larger than that of O²⁻ (1.4 Å). Red shift of the absorption edges was observed for all doped NaTaO₃ samples. Moreover, increasing the amount of S-doping resulted in a stronger absorption edge shift to longer wavelengths. The photocatalytic activities of S-doped NaTaO₃ samples were measured under UV and visible-light irradiation in the photodegradation of methyl orange (MO). All S-NaTaO₃ samples showed a similar photoactivity under UV light to that of pure NaTaO₃. However, the decolorization efficiency with the S-doped samples under visible-light was ca. 4.5 times greater than with the pure NaTaO₃, due to the narrower band gap caused by S-doping. To eliminate the sensitization effect of MO under visible light, phenol was also used as a model compound for photocatalytic testing under visible light. The results showed that after irradiation for 8 h in the presence of S-doped NaTaO₃, ca. 60% of the phenol was degraded. Lie et al. presented a possible catalytic mechanism for S-doped NaTaO₃ to explain the photocatalytic activity of the obtained samples. The 3p orbital energy of S is higher than O 2p orbitals and is close to the top of the VB of NaTaO₃. During the doping process, O atoms are substituted with S atoms, which results in an interaction between the 3p orbitals of the S atom and the Ta 5d orbitals (see Fig. 5A). This process leads to generation of several discrete mid-gap bands just above the valence band [199,213]. In summary, S anion doping caused narrowing of the NaTaO₃ band gap and enhanced its photocatalytic activity.

N-doped NaTaO₃ has also displayed remarkable improvement in visible-light photocatalytic activity [206–209]. Liu et al. synthesized N-doped NaTaO₃ photocatalysts by an improved solid-state reaction method and tested their photocatalytic activity in the degradation of methylene blue (MB) aqueous solution under UV light [206]. Firstly, NaTaO₃ was synthesized by heating Ta₂O₅ and NaOH (molar ratio = 1:2, 550–1000 °C, 12 h). Secondly, NaTaO₃ was heated with C₃H₆N₆ at 270 °C for 3 h. The molar ratio of

C₃H₆N₆/NaTaO₃ was varied from 0 to 50%. All of the photocatalyst particle sizes were in the range of 100–150 nm. UV–vis diffuse reflectance spectra of the NaTaO_{3-x}N_x powders showed that all samples had an absorption edge in the range of 312–328 nm, which corresponds to band gap values of around 3.9 eV. Based on their results, Liu et al. reported that NaTaO_{3-x}N_x photocatalysts are only sensitive to UV-light irradiation. Among all the obtained samples in which the molar ratio of C₃H₆N₆/NaTaO₃ was varied from 0% to 50%, the sample with an empirical formula of NaTaO_{2.961}N_{0.039} showed the highest photodegradation rate for MB solution, achieving complete decolorization of MB after 40 min irradiation [206]. Liu et al. reported that the preparation conditions and method had a significant impact on photocatalytic activity, because the solid-state reaction method has many disadvantages such as the formation of inhomogeneous products and lack of control over crystallinity and particle size [206]. In this regard they proposed a one-step hydrothermal process to obtain N-doped NaTaO₃ nanocubic photocatalysts [209]. Ta₂O₅, NaOH, and desired amounts of NH₃·H₂O (100–500 μl) were heated in the temperature range of 160, 180, 200 °C for 12 h. The molar ratio of Ta/OH⁻ was varied from 1/5 to 1/20. They investigated the influence of catalyst dose, initial pH, and N content on the degradation, and performed kinetic studies on the decoloration of methyl orange (MO) under visible-light irradiation. Based on XRD and XPS analyses, they reported that the replacement of O with N in the NaTaO₃ lattice did not result in significant structural changes, with all samples exhibiting pure perovskite structure. In addition, they observed N 1s peaks in the XPS spectra, which were characteristic of N³⁻, indicating the presence of Ta–N bonds. The highest photocatalytic activity was reported for the NaTaO_{2.953}N_{0.047} sample. The complete decolorization of MO (20 mg l⁻¹) was achieved using a 100 mg/100 cm³ loading of N-doped NaTaO₃ at pH 4.0 [209]. Liu et al. explained that the higher number of O vacancies in the N-doped NaTaO₃ compared to pure NaTaO₃ was responsible for the higher photoactivity of N-doped samples, and proposed a possible degradation mechanism of MO by N-doped NaTaO₃ under visible light (see Fig. 5B). Absorption of photons by N-NaTaO₃ leads to the generation of electron-hole pairs. Excited electrons will react with O₂ dissolved in the solution, while holes will be captured by OH⁻ or H₂O species adsorbed on the surface of the catalyst and produce OH radicals [209].

Zhao et al. investigated how hydrothermal synthesis reaction time influenced the morphology and photocatalytic activity of NaTaO_{3-x}N_x photocatalysts, and presented a possible mechanism for the formation of the cubic structure [208]. Moreover, they investigated the effect of hydrothermal reaction temperature (160, 180, and 200 °C) on the crystallization of N-doped NaTaO₃. Ta₂O₅, NaOH and NH₃·H₂O were used as starting materials. They observed that all XRD diffraction peaks originating from the NaTaO₃ crystal appeared when the temperature was higher than 180 °C. In order to investigate the reaction time, the synthesis was performed at 180 °C for 3, 6, 9, and 12 h. A highly crystalline phase was formed after 9 h of hydrothermal treatment. Zhao et al. proposed the schematic diagram of N doped into NaTaO₃ presented in Fig. 6. A NaTaO₃ layer is formed by the reaction between Ta₂O₅ and Na⁺ ions. When the reaction time was increased, Na⁺ reacted with Ta₂O₅ through the NaTaO₃ layers, and N³⁻ substituted the O²⁻ in NaTaO₃ to form NaTaO_{3-x}N_x [208]. The photocatalytic activity of the NaTaO_{3-x}N_x samples was measured in the decomposition of methylene blue under ultraviolet and visible-light irradiation. The sample obtained at 180 °C had the highest photocatalytic activity under UV irradiation, with ca. 100% of MB being degraded after irradiation for ca. 40 min or 5 h under UV or visible-light irradiation, respectively.

Yang et al. prepared N/F-NaTaO₃ powders by the hydrothermal method for 12 h at 160 °C through controlling the NaOH/NH₄F molar ratios and investigated the N/F co-doping on the crystal structure, morphology and photocatalytic activity [214]. Ta₂O₅,

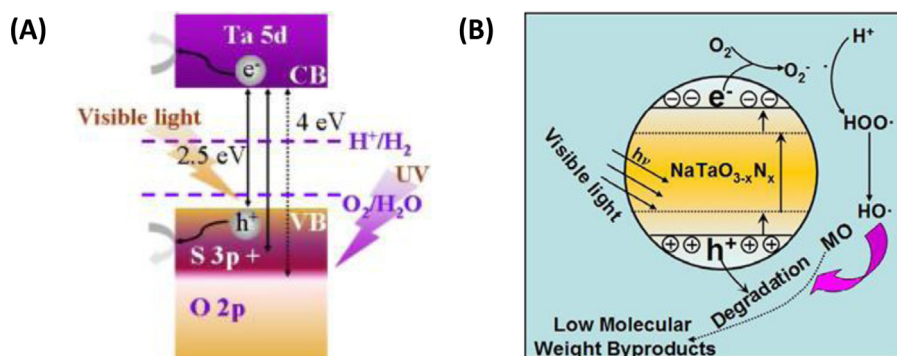


Fig. 5. Schematic drawings mechanism for the photocatalytic activity of: (A) S anion-doped NaTaO₃ photocatalysts proposed by Li et al. Reprinted from ref. [213]; (B) NaTaO_{3-x}N_x photocatalysts proposed by Liu et al. Reprinted from ref. [209].

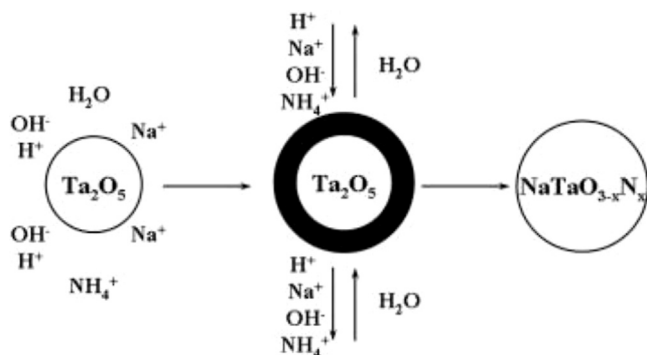


Fig. 6. The schematic diagram of N doped into NaTaO₃ during one-step hydrothermal process proposed by Zhao et al. Reprinted from Ref. [208].

NaOH and NH₄F were used as precursors. Using XRD analysis, Yang et al. noticed that pure NaTaO₃ and the N/F-NaTaO₃ powders obtained by doping N/F (NaOH/NH₄F = 1.0/1.5) had orthorhombic structure. When the doping content of N/F increased to 1.5/1.0, the crystal structure transformed from orthorhombic into monoclinic. Based on TEM images, Yang et al. reported that increase of NaOH concentration was responsible for synthesis of NaTaO₃ crystal with regular cubic block monoclinic phase in the range of 0.33–0.74 μm. All of obtained photocatalysts showed strong absorption in the UV region. The band gap values were calculated to be 3.93 eV for pure NaTaO₃ and in the range 3.87–3.98 eV for N/F-NaTaO₃ powders. PL spectra of NaTaO₃ powders excited at 453 nm due to the recombination of the excited electrons and holes. PL intensity decreased for N/F-NaTaO₃ photocatalysts which was related to the fact, that N/F act as a trapping site to capture photogenerated electrons from the conduction band, separating photogenerated electron–hole pairs. Photocatalytic activity of synthesized samples was measured as a decomposition rate of rhodamine B under UV-light irradiation. After 210 min of UV irradiation the highest photocatalytic activity was observed for NaTaO₃ photocatalyst with NaOH/NH₄F = 1.5/1.0, owing to its narrow band gap, the weak photoluminescence intensity and the low electrons and holes recombination [214].

Literature data confirm that the band structure of NaTaO₃ can be modified also by doping with appropriate cations at Ta sites in the NaTaO₃ lattice, which results in an increase in visible-light absorption. Bismuth-doped NaTaO₃ nanoparticles have been characterized and studied for photocatalytic reactions [202,215,216]. Li et al. prepared Na(Bi_xTa_{1-x})O₃ photocatalysts that were active in H₂ production under visible light, with Na(Bi_{0.08}Ta_{0.92})O₃ showing the highest photocatalytic activity [215]. They reasoned that the photocatalytic activity was due to a hybrid band structure formed by Bi 2s, Bi 2p, and Ta 5d orbitals in the CB.

Kanhere et al. investigated the visible-light photocatalytic activities and optical properties of Bi³⁺-doped NaTaO₃ [202]. Samples were synthesized *via* the solid-state route under different stoichiometric conditions. The starting materials (Ta₂O₅, Bi₂O₃ and Na₂CO₃), were mixed and heated at 900 °C for 10 h. The ionic radii concerned are Bi³⁺ (1.03 Å), Bi⁵⁺ (0.76 Å), Na⁺ (1.02 Å), and Ta⁵⁺ (0.64 Å), suggesting that, during the synthesis, Bi³⁺ can replace Na⁺, and Bi⁵⁺ can replace Ta⁵⁺. Kanhere et al. proved that substitutional doping with Bi at either Na or Ta sites preferentially, or both Na and Ta sites together, is possible under appropriate synthesis conditions. The location of Bi in the lattice is correlated with strongly Na-rich, mildly Na-rich, and Na-deficient conditions during the synthesis, *i.e.*, different molar ratios of Na₂CO₃ and Ta₂O₅. Based on XRD analysis, Kanhere et al. observed that: (i) under Na-deficient conditions Bi ions occupy Na sites, (ii) under strongly Na-rich conditions Bi ions occupy Ta sites, and (iii) under mildly Na-rich conditions Bi ions occupy both Na and Ta sites. Samples prepared under mildly Na-rich conditions showed visible-light absorption extending to 550 nm, samples prepared under strongly Na-rich conditions exhibited visible-light absorption limited to 450 nm, and samples prepared under Na-deficient conditions showed little visible-light absorption. The photocatalytic activity of the samples in the degradation of methyl blue (MB) under visible light was investigated. The highest degradation rates were observed for samples prepared under mildly Na-rich conditions, and the correlation between photoactivity and synthesis route can be presented as follows: mildly Na-rich > strongly Na-rich > Na-deficient [202].

Doping rare-earth metal oxides into perovskite-type NaTaO₃ can increase its ability to trap and transfer electron–hole pairs, which improves its photocatalytic activity [185–187,203–205,217,218].

Porob et al. synthesized La-doped (2%) NaTaO₃ photocatalysts using a 1:1 molar ratio Na₂SO₄/K₂SO₄ molten flux at different reaction times (0.5–1.0 h) [187]. The obtained particles were aggregated into irregular block-like structures in the size range 100–500 nm. The particle size decreased with an increase in the NaTaO₃:flux ratio from 1:1 through 1:2–1:3, and with a shorter reaction time (0.5 h). The photocatalytic activity of the obtained samples for H₂ generation was measured in an aqueous methanol solution. It was reported to be in the range 535–1115 mmol H₂ h⁻¹ g⁻¹, and increased with increasing particle size and decreasing amounts of flux used in the synthesis [187].

Li et al. synthesized nanosized cube-like NaTaO₃ and La-doped NaTaO₃ photocatalysts by the hydrothermal method [203]. La(NO₃)₃, NaOH and Ta₂O₅ (Na:La:Ta = 1 – X:X:1, (X = 0, 1, 2, 3, 4, 5% mol, respectively) were mixed and heated at 160 °C for 24 h. XRD patterns showed that pure and La-doped NaTaO₃ samples exhibited orthorhombic phase character. Moreover, they noted that increasing the La amount caused a slight shift to larger angles. This

suggests that some of the La was homogeneously doped into the NaTaO₃ lattice, while the other portion was localized near the surface. Additionally, a slight shift to larger angles can result from the substitution of La ions (12-coordinated La³⁺ ion = 1.36 Å; 6-coordinated La³⁺ ion = 1.032 Å) for bulk Na ions (Na⁺ ion = 1.39 Å) in the perovskite structure [203]. Based on diffuse reflectance UV–vis analysis, Li et al. estimated that the band gaps of pure NaTaO₃ and La-doped NaTaO₃ were about 3.94 and 3.86 eV, respectively, which suggests that La³⁺ doping caused narrowing of the band gap. Photocatalytic activity was measured in the decomposition of safranin T solution under UV light. The highest degradation rate was achieved when the amount of La used for doping was 2 mol%. Around 90% of the dye was degraded in 2 h in the presence of the La-doped sample [203].

Torres-Martínez et al. compared the photoactivity of NaTaO₃ samples doped with Sm and La prepared by two different methods: sol–gel and solid-state reactions [204]. In the solid-state method sodium carbonate (Na₂CO₃) and tantalum oxide (Ta₂O₅) were mixed and calcined at 850 °C for 12 h. For the case of the doped oxides, rare earth oxides, Sm₂O₃ and La₂O₃ were added (1 M%). In the sol–gel synthesis tantalum ethoxide and ethanol were mixed. Subsequently, a stoichiometric amount of a solution containing sodium acetate was added simultaneously with a solution of rare-earth salts. Prepared gel was calcined at 600 and 800 °C during 6 h. The samples synthesized by both sol–gel and solid-state reactions exhibited a NaTaO₃ phase with the orthorhombic structure. However, the samples prepared by the solid-state reaction contained Na₂TaO₁₁ as a second phase. XRD results showed that the crystallinity of the La-doped NaTaO₃ materials was higher than that of the Sm-doped materials. The *E_g* values for sol–gel and solid-state photocatalysts were in the range of 3.6–4.0 and 3.7–3.9 eV, respectively. The photoactivities of the Sm–NaTaO₃ and La–NaTaO₃ samples were measured in the degradation of aqueous methylene blue solutions under UV radiation. The results showed that the presence of La and Sm improved the photocatalytic performance of NaTaO₃. The highest photoactivity was reported for the sample doped with Sm, prepared by the sol–gel method, and calcined at 600 °C. Torres-Martínez et al. observed that this photocatalytic behavior was similar to that reported for the degradation of RhB under UV light using NaTaO₃ and NaTaO₃ doped with La and Sm, whereas the Sm–NaTaO₃ photocatalyst prepared by the sol–gel method and calcined at 600 °C showed the highest photocatalytic activity [218].

Recently, the surface plasmon resonance of noble metal nanoparticles (such as Au and Ag) has found to be excited under visible-light and exhibits photocatalytic activity in the whole solar spectral region. In this regard, La-doped NaTaO₃ photocatalysts loaded with Au NPs were prepared by Iwase et al. [217]. La-doped NaTaO₃ was prepared by a solid state reaction [186]. Au NPs were loaded by photodeposition and impregnation methods using an aqueous solution of HAuCl₄·4H₂O. They investigated the effect of the loading method of the Au cocatalyst, *i.e.*, photodeposition or impregnation, on the photoactivity of La–NaTaO₃ in the water splitting process. For complete characterization, Iwase et al. selected samples of La–NaTaO₃ loaded with 1 wt% of Au NPs because of their high photocatalytic activity, there by producing samples designated Au(1 wt%)/NaTaO₃:La-photo (obtained by photodeposition) and Au(1 wt%)/NaTaO₃:La-imp (obtained by impregnation). Based on SEM and TEM analyses they observed differences between the particle size and shape of the Au NPs loaded onto the La–NaTaO₃ surfaces. The photodeposited and impregnated Au NPs were hemispherical and spherical, respectively. The size of the hemispherical Au particles was in the range of 5–20 nm, while the spherical Au particles were larger, with sizes ranging from 5 to 40 nm. The particle size showed good correlation with the surface plasmon absorption bands. The smaller hemispherical Au

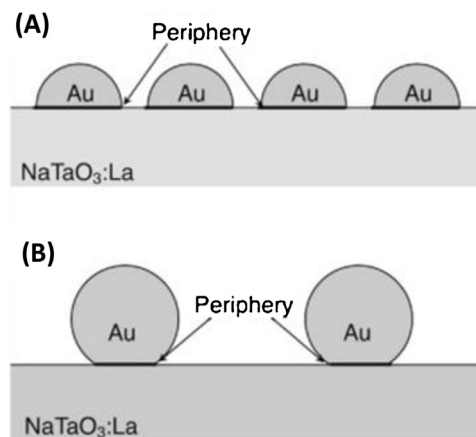


Fig. 7. Schematic views of (A) photodeposited and (B) impregnated Au on NaTaO₃:La proposed by Iwase et al. Reprinted from Ref. [217].

NPs in Au(1 wt%)/NaTaO₃:La-photo showed a sharp surface plasmon absorption band at *ca.* 530 nm, while the larger spherical Au NPs in Au(1 wt%)/NaTaO₃:La-imp exhibited a broad surface plasmon absorption band at *ca.* 550 nm [217]. XPS analysis confirmed that the photodeposited Au NPs were better dispersed on the La–NaTaO₃ surface than the impregnated type. The Au/Ta ratio for Au(1 wt%)/NaTaO₃:La-photo and Au(1 wt%)/NaTaO₃:La-imp was 0.054 and 0.040, respectively. This indicated that the number of photodeposited Au islands on NaTaO₃:La was larger than that for the impregnated sample. Iwase et al. proposed a schematic view of the photodeposited and impregnated Au NPs on the La–NaTaO₃ surface (see Fig. 7), and related these observations with the photoactivity of the obtained samples. Au/NaTaO₃:La prepared by the impregnation method showed higher and more stable activity in the water-splitting process. Iwase et al. claimed that the photocatalytic activity was directly related to O₂ reduction on the loaded Au NPs, where O₂ reduction on photodeposited Au/NaTaO₃:La was more efficient than that on impregnated Au/NaTaO₃:La. Because the periphery of the interface between Au and NaTaO₃:La is important for O₂ activation, the larger-perimeter interface in the Au(1 wt%)/NaTaO₃:La-imp sample led to its higher activity [217].

Visible-light-driven plasmonic Ag–NaTaO₃ photocatalysts were prepared by Xu et al. [219]. Pure NaTaO₃ was obtained by hydrothermal method (140 °C, 12 h) and photochemical reduction process was used to modified NaTaO₃ surface with silver NPs. Ta₂O₅, NaOH and AgNO₃ were used as precursors. XRD patterns of obtained samples were indexed to the orthorhombic phase of NaTaO₃ and no signal about silver can be detected. Based on the SEM and TEM images it can be observed that synthesized photocatalysts had cube morphology with an average size of around 100 nm with small Ag nanoparticles (about 5–10 nm) separately loaded on the surface of NaTaO₃. Reduction of Ag on NaTaO₃ was also confirmed by XPS analysis. The two peaks in at 367 and 372.9 eV can be attributed to Ag 3d_{5/2} and Ag 3d_{3/2}. Additionally, Ta 4f peak the value of about 25.99 eV, confirming that Ta exists mainly in the Ta⁵⁺. UV–vis diffuse reflectance spectrum revealed that Ag–NaTaO₃ sample showed a shallow peak with higher intensities at about 520 nm which was attributed to the surface plasmon resonance (SPR) effect of the Ag NPs. The photocatalytic activity of the Ag–NaTaO₃ was evaluated in the degradation of rhodamine B (RhB) under visible-light illumination ($\lambda > 425$ nm). The highest photoactivity was observed for Ag–NaTaO₃ sample at the nominal atomic ratio of silver to tantalum as 0.6 (*k*_{RhB} = 0.56 h^{−1}), which is more than 3 times that of pure NaTaO₃ (*k*_{RhB} = 0.20 h^{−1}). Xu et al. explained that enhanced plasmonic photocatalytic activity of the Ag–NaTaO₃ nanocomposite should be attributed to the effi-

cient charge separation and transfer. Under visible light irradiation Ag–NaTaO₃ photocatalyst is excited due to the localized SPR of the Ag nanoparticles and generated electron–hole pairs in the NaTaO₃ nanocrystal. Excited electrons move and accumulate on the surface of the Ag NPs, while holes form on the surface of NaTaO₃ nanocrystal and oxidize the RhB molecules. At the same time, due to the a Schottky barrier formed at the Ag–NaTaO₃, excited electrons from the silver inject into the NaTaO₃ conduction band. Subsequently, electrons react with molecular oxygen to form superoxide radical anions, O₂^{•−} and finally HO• radicals which are responsible for RhB degradation [219].

Summarizing, due to the fact that valence band of NaTaO₃ predominantly consists of O 2p orbitals whose potential energy levels are located at a deep position of about 3 V versus NHE it is not active under visible-light irradiation. In order to improve its optical properties, several methods were employed to modify the interface of NaTaO₃ in a way that alters the mechanism of the recombination rate of electron–hole pairs. Doped NaTaO₃ compounds, with the dopants like Bi, La, Sm, Co, Cr, Cu, N, S, and F, have been studied for visible light photocatalysis. These studies show that doping is a promising way to induce visible light absorption in NaTaO₃. Although a few modified systems are reported in the literature, efficient photocatalytic system which works under visible light is lacking among the family of NaTaO₃ materials. In order to design such a system, the effect of various dopants on the band gap of NaTaO₃ should be studied in detail so potential of NaTaO₃ as a host material is not fully explored.

4.3. Pristine KTaO₃

KTaO₃, (space group *Fd3m*), has attracted attention because of its interesting dielectric, photoconductive, and optical properties, as well as its nonlinear performance at low temperatures [201]. For KTaO₃, the bands between −17.45 and −15.72 eV are mainly the contribution of O 2s, Ta 6s and Ta 5d, the second region below the Fermi level is between −11.19 and −10.65 eV is only the contribution of K 3p. The valence bands lying between −5.51 eV and the Fermi level are mainly due to O 2p states hybridized with Ta 5d, which means the existence of a covalent type bond between the O and the Ta [201]. Nanocrystalline KTaO₃ can be synthesized via reactive magnetron sputtering, and solvothermal and sol–gel process [33,221,222]. Zou et al. obtained octahedral nanocrystalline KTaO₃ particles using the hydrothermal method [223]. The edge size of the NPs was ca. 500 nm and the band gap was 4.06 eV. Zou et al. suggest that the large band gap may improve its suitability for photonic and optoelectronic applications, and other functional devices.

He et al. synthesized perovskite and pyrochlore KTaO₃ nanostructures in mixed water/EtOH and water/hexane systems by solvothermal reaction [222]. The results showed that the ratio of inert solvent (EtOH or hexane) to active solvent (water) played a significant role in manipulating the crystalline behavior of KTaO₃ to form pyrochlore or perovskite nanocrystals.

Marchelek et al. prepared KTaO₃-based binary and ternary semiconductor composites through hydrothermal reaction [33]. They analyzed the effect of the composition and molar content of the semiconductors on the morphology and photocatalytic activity of KTaO₃-based nanocomposites in gaseous-phase toluene degradation using light-emitting diodes (LEDs, 375 nm). KTaO₃ + CdSe + SrTiO₃; KTaO₃ + CdS + WO₃; and KTaO₃ + CdS + MoS₂ composites were synthesized using one-step or two-step hydrothermal methods. In one-pot synthesis route, all reagents in specified molar ratio of products were mixed, transferred into auto-clave and thermally treated under the selected conditions. In 2-step hydrothermal reaction, solution containing appropriate semiconductor precursors was mixed with previously

synthesized KTaO₃. SEM analysis of the morphology of pure KTaO₃ samples showed that, depending on the reaction medium, amount of KOH, and hydrothermal synthesis temperature, octahedral or cubic KTaO₃ was obtained. The average edge size of the octahedral nanostructures was ca. 160 nm (ca. 160–240 nm in length), and the average size of the cubic structures was in the range 4–6 μm. Detailed analysis of the KTaO₃ + WO₃ structures showed that KTaO₃ occurred in octahedral and cubic forms, depending on the molar ratio of semiconductors, i.e., 2:1 or 10:1. The XRD analysis confirmed that the sample prepared with a ratio of 2:1 comprised almost pure pyrochlore-like K₂Ta₂O₆, while increasing the amount of tantalate changed the morphology to a cubic structure [33]. Using diffuse reflectance spectroscopy, Marchelek et al. observed that octahedral and cubic KTaO₃ absorb light in different ranges. Octahedral KTaO₃ exhibited an absorption band centered at ca. 310 nm, while the adsorption spectra of cubic KTaO₃ shifted to the visible region. Two different absorption spectra were observed for KTaO₃ + WO₃ samples with molar ratios of 2:1 and 10:1. Furthermore, the KTaO₃ + WO₃ (10:1) sample containing cubic KTaO₃ exhibited a shift toward visible light. It can also be noticed that KTaO₃ with CdS and CdSe showed decreased absorption in the visible-light range compared to that with pure KTaO₃ semiconductors. Marchelek et al. reported that KTaO₃-based nanocomposites were effective for toluene degradation over four subsequent cycles. In the first cycle of toluene degradation, the highest photocatalytic activity (64% after 1 h irradiation) was observed for KTaO₃ with a cubic structure. Octahedral KTaO₃ exhibited lower efficiency for toluene removal. After a 60 min process, 46% of toluene was degraded. Of the binary and ternary nanocomposites, the highest photoactivity was observed for KTaO₃ + WO₃ = 2:1 and KTaO₃ + CdS + MoS₂ = 10:5:1, with ca. 60% of toluene being degraded in each case. The best stability and the highest toluene degradation efficiency during all four cycles of photodegradation was observed for KTaO₃ + CdS + MoS₂ (10:5:1) synthesized using a two-step hydrothermal route. Marchelek et al. proposed that the higher activity resulted from multi-photon excitation of photoactive materials with lower-energy photons and utilization of the heterojunction to drive electronic processes in the desired direction [33].

KTaO₃, KTaO₃-CdS, KTaO₃-MoS₂, and KTaO₃-CdS-MoS₂ nanocomposites were obtained by the hydro/solvothermal or calcination method by Bajorowicz et al. [220]. They investigated the effect of the preparation method, type, and amount of the composite components on the surface properties and photocatalytic activity during phenol degradation in the aqueous phase, as well as activity and photostability in toluene degradation in the gas phase. The obtained KTaO₃ structures were cubic in two different ranges of particle size: small nanocubes in the size range 0.2–1 μm, and larger ones in the range 5–8 μm. Based on the SEM analysis of binary KTaO₃-CdS and KTaO₃-MoS₂ composites, Bajorowicz et al. observed differences in the sample structures depending on the method of sample preparation. The samples prepared by calcination comprised predominantly cubes, which proved the presence of KTaO₃, while the solvothermal method led to the formation of other nanostructures such as K₂Ta₁₅O₃₂, Ta₂O₅, TaS₂, and K₂Ta₂O₆, which were further confirmed by XRD analysis. Moreover, in samples KTaO₃-MoS₂ = 10:1 and KTaO₃-CdS-MoS₂ = 10:1:1 obtained by solvothermal mixed solutions, the cubic KTaO₃ structure transformed to octahedral. Diffuse reflectance spectroscopy UV–vis absorption spectra of pure KTaO₃ showed an absorption band centered at ca. 310 nm, which was consistent with the result obtained by Marchelek et al. [33,220]. Based on the diffuse reflectance spectra, it was concluded that binary composites loaded with small amounts of CdS or MoS₂ exhibit absorption maxima that shifted to shorter wavelengths, while for ternary composites, loading with MoS₂ and CdS shifts absorbance peaks to longer

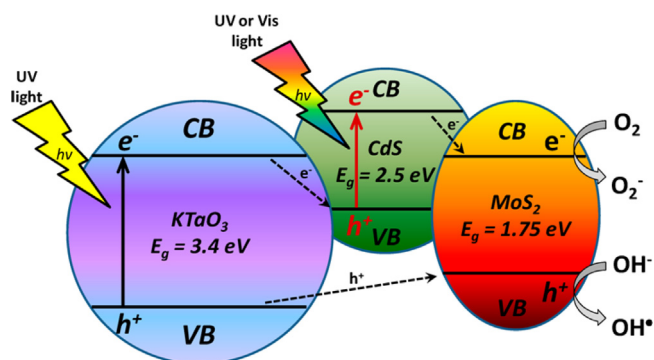


Fig. 8. Probable UV-vis two-photon excitation cycle of KTaO₃-CdS-MoS₂ composite proposed by Bajorowicz et al. Reprinted from Ref. [220].

wavelengths. The photocatalytic activity of the composites was measured for phenol degradation under UV-vis and visible-light irradiation. Bajorowicz et al. reported that the photoactivity of KTaO₃ increased with CdS loading. In the presence of pure KTaO₃, only 18% of the phenol was degraded after 60 min of irradiation under UV-vis light, while in the presence of KTaO₃-CdS=10:1, ca. 59% of phenol was degraded. Moreover, they observed that for binary composites containing MoS₂, photoactivity depended on the preparation technique. Phenol degradation after 60 min of irradiation in the presence of KTaO₃-MoS₂ samples obtained by hydrothermal and calcination was 48% and 30%, respectively. For ternary KTaO₃-CdS-MoS₂ nanocomposites, it was noted that higher amounts of CdS enhanced the photocatalytic activity. In the presence of KTaO₃-CdS-MoS₂ with molar ratios of 10:1:1 and 10:5:1, the degradation of phenol reached ca. 35% and 60%, respectively. Also, the KTaO₃-CdS-MoS₂ 10:5:1 sample showed the highest photoactivity under visible-light irradiation, with 42% of the phenol being degraded after 60 min of irradiation [220]. The photocatalytic activity was also measured in the degradation of the toluene in the gas phase under UV irradiation using LEDs ($\lambda_{\text{max}} = 375 \text{ nm}$) as a source of light. In the presence of KTaO₃, 64% of the toluene was degraded after 60 min. In the case of binary and ternary KTaO₃-based composites, Bajorowicz et al. observed that photocatalytic activity depended not only on the type and content of the composite components, but also on the preparation method. Based on their results, the authors offered a possible mechanism involving UV-vis two-photon excitation cycle in the KTaO₃-CdS-MoS₂ composite, as presented in Fig. 8. UV light causes excitation in solid KTaO₃ ($E_g = 3.4 \text{ eV}$) and generates free electrons and holes. Because the VB position of KTaO₃ and MoS₂ is +3.1 V and +1.8 V, respectively, h^+ will be transferred from KTaO₃ to MoS₂. Moreover, UV or visible light can be absorbed at the same time by CdS ($E_g = 2.5 \text{ eV}$) to generate e^- and h^+ . The CB position of CdS (−0.6 V) is higher in energy than that of MoS₂ (+0.05 V); therefore, electron transfer can occur from CdS to MoS₂. This causes charge separation at the CdS-MoS₂ junction. Finally, because the CBs of KTaO₃ and CdS are −0.3 V and +1.8 V, respectively, e^- will be transferred from KTaO₃ to CdS, and recombination of e^- in KTaO₃ with h^+ generated in CdS can occur, thus completing the photoexcitation cycle in which the excited state of MoS₂ has been achieved via a two-photon process [220].

Progress of nano-engineering, requiring knowledge of the effects controlled by size and confinement geometry, depends highly on the development of new synthesis technologies and studies of KTaO₃ nanocrystalline powders and KTaO₃-based composites. However, despite theoretical predictions of unique properties of KTaO₃ nanoparticles, only a few experimental articles on synthesis of KTaO₃ photocatalysts, characterization and size-dependent properties in relation to photocatalysis processes

are published by several scientific groups. The first theoretical and experimental studies suggested a strong dependence of the properties of KTaO₃ nanoparticles on structural quality, presence of defects and impurities. This calls for sufficient progress in the development of technology and synthesis of high-quality KTaO₃ nanopowders.

4.4. Modified KTaO₃

It is well known that doped nanocrystals obtained by the incorporation of impurity ions into semiconductors exhibit enhanced light response. Liu et al. synthesized KTaO₃ and K_{1-x}La_xTaO₃ (where $x = 0, 0.02, 0.04, 0.06, 0.08$, or 0.10) nanocrystals with cubic morphology via a hydrothermal method [34]. A certain amount of KOH and La(NO₃)₃ and Ta₂O₅ were heated at 200 °C for 24 h. TEM images of pure KTaO₃ showed that the nanocrystals had an average size of ca. 100 nm, while La³⁺ doping caused a decrease in the particle size to ca. 70 nm for K_{0.04}La_xTaO₃ and 30 nm for K_{0.08}La_xTaO₃. Liu et al. suggested that incorporation of La³⁺ ions into KTaO₃ has an influence on the primary growth stage and the intraparticle ripening process, which leads to the generation of smaller NPs. By analyzing the XPS results, the presence of La³⁺ and mixed-state Ta⁵⁺ and Ta⁴⁺ was confirmed in the K_{1-x}La_xTaO₃ nanocrystals. The ionic radii of La³⁺, K⁺, and Ta⁵⁺ are 1.06 Å, 1.33 Å, and 0.69 Å, respectively; therefore, it is highly possible that La³⁺ will substitute K⁺ rather than Ta⁵⁺ sites in the prepared samples. Moreover, the Pauling's electronegativity of La³⁺ is 1.30, close to that of 0.93 for K⁺, but much smaller than that of 1.80 for Ta⁵⁺ [34]. Investigation of the optical properties of K_{1-x}La_xTaO₃ photocatalysts showed that all samples exhibited a strong absorption band in the UV region. The estimated values of the energy band gap for pure KTaO₃ and K_{1-x}La_xTaO₃ ($x = 0.02$) were 3.62 and 3.65 eV, respectively. It can be concluded that La³⁺ doping leads to a blue shift of the absorption edge of K_{1-x}La_xTaO₃ nanocrystals. Photocatalytic activity of K_{1-x}La_xTaO₃ was measured in the decomposition of methyl orange (MO) under UV irradiation. La³⁺-doped samples showed increasing activity with an increase in the La³⁺ doping concentration to 0.08. When the amount of La³⁺ increased to 0.10, a decrease in photoactivity was observed. To understand the mechanism of MO degradation in the presence of K_{1-x}La_xTaO₃ nanocrystals, Liu et al. added active-species scavengers to the MO solution, including benzoquinone (BQ) as a radical scavenger, *tert*-butyl alcohol (TBA) as a hydroxyl radical scavenger, ammonium oxalate (AO) as a hole scavenger, and AgNO₃ as an electron scavenger. They observed that both BQ and TBA inhibited the photodegradation of MO. In addition, AgNO₃ and AO slightly inhibited the photodegradation of MO. The authors explained that AgNO₃ and AO enhanced the separation of electrons and holes and more photogenerated holes and the following active species were generated, which promoted the degradation rate. The enhancement in the photocatalytic activity was also explained by the fact that with an increase in the La³⁺ dopant concentration, particle size reduction with enhanced BET surface area was observed, thereby providing more photoactive sites and faster interfacial charge transfer to the reaction sites for the degradation of the dyes. Moreover, based on the XPS analysis, Liu et al. suggested that the presence of Ta⁴⁺ ions can promote effective separation of the photogenerated electrons and holes by suppressing the formation of cationic vacancies [34].

It is known that controlling the size of noble metal nanoparticles deposited on the semiconductors surface can enhance light adsorption and photocatalytic activity. Xu et al. proposed an efficient enhancement of the H₂ generation under simulated sunlight and visible light irradiation in the presence of Ag-KTaO₃ [193]. KTaO₃ was obtained by hydrothermal method and Ag NPs (0.025; 0.05; 0.1 and 0.2 wt%) were deposited by an *in situ* photodeposition method. The XRD patterns showed that all peaks of KTaO₃ can be indexed to

the orthorhombic phase and no signal about silver can be detected. SEM and TEM analysis confirmed that size of deposited Ag nanoparticles increased with the increasing of the amount of weight ratio of Ag to KTaO_3 . The average size of Ag nanoparticles was from 6 to 10 nm. UV–vis diffuse reflectance spectra showed that pure KTaO_3 presented the photoresponse property in the UV light region, while Ag– KTaO_3 sample had broad peak from 400 to 600 nm attributed to the surface plasmon resonance (SPR) effect of the Ag nanoparticles. The photocatalytic water splitting process of KTaO_3 and Ag– KTaO_3 under simulated sunlight showed that after 7 h, the average rates of H_2 production for pure KTaO_3 and 0.025; 0.05; 0.1 and 0.2 wt% Ag– KTaO_3 were 98.48, 164.13, 185.60, 149.59, and 109.88 $\mu\text{mol/h g}$, respectively. At the same time, water-splitting activity under visible light for H_2 production for pure KTaO_3 and 0.025; 0.05; 0.1 and 0.2 wt% Ag– KTaO_3 were 0, 4.92, 25.94, 9.27, and 6.18 $\mu\text{mol/h g}$, respectively. Xu et al. explained that decreasing in photoactivity with increasing the amount of Ag NPs can be related to the fact, that increasing the silver content led to the aggregation of the nanoparticles and the Ag NPs were large and limited the transfer of photogenerated charge carriers. Photoluminescence spectra used to measure the electron–hole recombination, showed that the PL intensity at 468 nm for the Ag– KTaO_3 nanocomposite was weaker than for the KTaO_3 nanocubes [193].

Concluding, KTaO_3 is a promising photocatalytic material. However, its wide band gap (3.4–3.6 eV) is too large to be activated under visible-light irradiation. Thus, doping with the foreign ions in the different sites of KTaO_3 may provide a optional technology to design the active photocatalysts. Actually, there are few reports about KTaO_3 -based photocatalysts active under visible irradiation, so development of highly efficient photocatalysts is still needed.

5. Niobium perovskites: NaNbO_3 and KNbO_3

Similar to tantalum-based photocatalysts, niobium-based perovskites (ANbO_3 , A=Na, K, Ag, Cu) show good photocatalytic activity. NaNbO_3 and KNbO_3 have band gap energy values of ca. 3.08 and 3.14 eV, respectively, and hence, they show excellent photocatalytic properties under UV irradiation. However, modification of the band gap structure can enhance their photoactivity under visible light [35]. N doping in NaNbO_3 and KNbO_3 has been studied for the degradation of 2-propanol, water splitting, and organic pollutant degradation [224,225]. Moreover, perovskite alkaline niobates exhibit many other useful properties such as ferroelectricity, piezoelectricity, ionic conduction, and photorefractive [226,227]. Table 4 presents NaNbO_3 and KNbO_3 photocatalysts prepared via different preparation methods and their application to photocatalytic processes.

5.1. Pristine NaNbO_3

Sodium niobate is a well-known perovskite oxide that possesses attractive physical properties such as low density and high sound velocity, and is useful for ferroelectric and piezoelectric applications [228]. Moreover, NaNbO_3 is nontoxic and highly stable, and therefore, it can be used in photocatalytic processes [129,224,229–236]. The basic perovskite NaNbO_3 has a cubic structure with the space group of $Pm\bar{3}m$, but it is stable only at high temperature (>913 K), while at room temperature, the common phase of NaNbO_3 is an antiferroelectric orthorhombic phase (space group of $Pbcm$, $a = 5.506 \text{ \AA}$, $b = 5.566 \text{ \AA}$, and $c = 15.52 \text{ \AA}$) [129]. Additionally, valence band tops of cubic and orthorhombic NaNbO_3 are constructed from O $2p$ orbitals, and they are located at similar energy levels. At the same time, the bottoms of conduction band are significantly different. The energy level of the conduction band bottom in cubic NaNbO_3 is lower than that in orthorhombic NaNbO_3

which is directly related to the fact that, the variant octahedral ligand field of orthorhombic NaNbO_3 that changes Nb–O bond lengths and O–Nb–O bond angles of the basic cubic crystal structure [129]. NaNbO_3 was first proposed as a photocatalyst by Kato in a comparison study with NaTaO_3 [237]. Alkali niobates have been synthesized via the solid-state reaction of alkali metal carbonates and Nb_2O_5 [236]. Over a temperature range varying from room temperature to 1000 K, several phases of NaNbO_3 can be formed, such as tetragonal and cubic structures, while higher-temperature calcination of alkaline niobates can lead to the undesirable volatilization of alkaline species [228,238]. Despite the fact that cubic, tetragonal, and orthorhombic NaNbO_3 are all constructed from the basic perovskite unit, most of the photocatalytic investigations reported were carried out using the orthorhombic form. NaNbO_3 with special morphologies such as nanowires, nanorods, or plate-like structures have been shown to exhibit higher photoactivity in comparison with samples prepared by the solid-state reaction method [234,239,240].

Li et al. studied photocatalytic hydrogen evolution over NaNbO_3 prepared by three different methods: the solid-state reaction (SSR), hydrothermal (HT) and polymerized complex (PC) methods [229]. Based on the synthesis technique, the samples were designated SSR, HT, PC.600, and PC.900 (where the samples obtained by the PC method were calcined at 600 or 900 °C). The SSR sample was obtained by mixing Na_2CO_3 and Nb_2O_5 and then heating the mixture at 900 °C for 10 h. In the HT method Nb_2O_5 and an aqueous NaOH solution were heated at 200 °C for 250 min. During the PC preparation NbCl_5 and citric acid were mixed with Na_2CO_3 and ethylene glycol. The mixture was heated at 120–130 °C until it turned solid and finally heated at 300 °C for 20 min and at 600 °C for 1 h. Li et al. observed that the morphology of NaNbO_3 is strongly dependent on the preparation method. The HT sample consisted of cubic particles, while the others consisted of spherical particles. Additionally, PC.600 had the smallest particle size (ca. 40 nm), the PC.900 particles were ca. 400 nm in size, and the SSR and HT samples had the largest particle size of 700 nm. The band gaps of the synthesized NaNbO_3 samples were estimated from the optical absorption spectra and were ca. 3.3–3.4 eV. From density of states (DOS) measurement, Li et al. observed that the bottom of the CB was located at 0.3–0.4 eV, which is more negative than the H^+/H_2 potential of 0 eV, and simultaneously the potential of the VB top was +2.94 eV, which is more positive than the $\text{O}_2/\text{H}_2\text{O}$ potential (+1.23 eV). Based on these calculations, they suggested that NaNbO_3 can be successfully used in the water splitting process [229]. The photocatalytic activity in H_2 evolution from both an aqueous methanol solution and pure water under UV irradiation was investigated. The authors reported that the sample prepared by PC with the smallest particles exhibited the highest photocatalytic activity in both reactions. Among the photocatalysts with spherical particles, the photoactivity increased with a decrease in the particle sizes in the order PC.600 > PC.900 > SSR. This dependence may be explained by the fact that smaller particles have shorter diffusion distances that the photogenerated electrons need to travel to reach the surface reaction sites, hence increasing the number of electrons that reach these sites. The high activity of the HT sample maybe further explained by the fact that this sample had more edges and corners on the surface, which can work as active sites for catalytic reactions and favorable sites for the adsorption of molecules [229,241,242]. The amounts of hydrogen obtained from pure water in the presence of NaNbO_3 produced by the SSR or HT and PC methods were 13 and 65 $\mu\text{mol/h}$, respectively [229].

Reducing the crystal size of photocatalysts can enhance their photocatalytic activity. Therefore, Shi et al. synthesized NaNbO_3 nanowires by a surfactant-assisted hydrothermal method [230]. Mixture of P123, $\text{Nb}(\text{OC}_2\text{H}_5)_5$ and NaOH were thermally treated at 200 °C for 24 h. The white precipitate was calcined at 550 °C for

Table 4Recent publications (2010–2015) of synthesis methods and characteristics of NaNbO₃ and KNbO₃ based-photocatalysts.

NaNbO ₃ based-photocatalysts						
NaNbO ₃ precursor	Doping moiety	Synthesis parameters	Model photocatalytic reaction	Experimental conditions	Photocatalytic activity	Ref.
Nb(OC ₂ H ₅) ₅	–	Procedure: <i>c</i> -NaNbO ₃ by polymerization–oxidation (FAPO) process, <i>o</i> -NaNbO ₃ by a polymerized complex (PC) method FAPO—1 g of (C ₂ H ₅ O) ₅ Nb, 0.24 g of C ₂ H ₅ ONa were added into 10 cm ³ of 2-methoxyethanol and 2.5 g of P-123 and heated to 95 °C PC—1 g of NbCl ₅ and 0.20 g of Na ₂ CO ₃ were added into 10 cm ³ of EtOH and added into 50 cm ³ EtOH containing 12 g of citric acid and 2 cm ³ of ethylene glycol, mixture was heated to 120 °C and oxidized in air at 600 °C for 2 h	H ₂ evolution (water splitting process)	0.3 g of NaNbO ₃ was dispersed in an aqueous methanol solution (50 cm ³ of CH ₃ OH + 220 cm ³ of H ₂ O) Irradiation source: 300 W Xe arc lamp, λ > 300 nm	In photocatalytic H ₂ generation, <i>c</i> -NaNbO ₃ (127 μmol h ^{−1}) shows higher activity than <i>o</i> -NaNbO ₃ (72.3 μmol h ^{−1})	[129]
Nb ₂ O ₅	–	Procedure: solid-state reaction Na ₂ CO ₃ and Nb ₂ O ₅ were mixed according to the ratio Na/Nb = 1.05 and calcined at 800 °C, 4 h	H ₂ evolution (water splitting process)	0.05 g NaNbO ₃ was dispersed into 50 cm ³ 20 vol% aqueous methanol solution in a 100 cm ³ glass reactor under air, H ₂ /Ar and O ₂ atmosphere Irradiation source: 300 W Xe arc lamp	The H ₂ evolution rate was 14 μmol/h for A (air), 27 μmol/h for B (H ₂) and 43 μmol/h for C (O ₂)	[231]
Nb ₂ O ₅	N	Procedure: one- and two-step molten salt processes One-step: heating a mixture of Bi ₂ O ₃ , Na ₂ CO ₃ , and Nb ₂ O ₅ with molar ratio of 5:7:10 in molten NaCl at 1225 °C, 12 h Two-step: Bi _{2.5} Na _{3.5} Nb ₅ O ₁₈ was firstly obtained was firstly obtained and then reacting with Na ₂ CO ₃ in molten NaCl at 960 °C, 3 h Pure NaNbO ₃ were mixed with urea at a weight ratio of 1:2.5 and heated at 400 °C, 1 h	Photodegradation of Rhodamine B (RhB)	0.1 g of NaNbO ₃ was added into 100 cm ³ of RhB (C ₀ = 5 mg/dm ³) Irradiation source: 300 W Xe lamp	The N-NaNbO ₃ prepared by the one-step molten salt process shows the highest activity in all the prepared samples	[232]
Nb(OC ₂ H ₅) ₅	In ₂ O ₃	Procedure: coprecipitation method InCl ₃ and Nb(OC ₂ H ₅) ₅ were dissolved in EtOH and added to a 8.4 M NaOH. After filtration and drying at 80 °C, obtained precursor were calcined at 500 °C, 12 h	H ₂ evolution (water splitting process)	0.3 g of In ₂ O ₃ /NaNbO ₃ was dispersed in an aqueous methanol solution (50 cm ³ of CH ₃ OH + 220 cm ³ of H ₂ O) Irradiation source: 300 W xenon lamp, λ > 420 nm	For In ₂ O ₃ /NaNbO ₃ containing 37.5 at% of In, the amount of evolved hydrogen was 13.2 and 44.6 μmol h ^{−1} g ^{−1} for visible and ultraviolet light irradiations	[234]
NbCl ₅	Ag	Procedure: polymerized complex method Pure NaNbO ₃ prepared as reported in [202] For Na _{0.6} Ag _{0.4} NbO ₃ two precursors were used: silver acetate + sodium carbonate and silver nitrate + sodium nitrate. Sample was obtained by calcination at 700 °C, 1 h	Water splitting process and photodegradation of 2-propanol	0.1 g of NaNbO ₃ was dispersed in 370 cm ³ of pure water 0.15 g of NaNbO ₃ was placed on the base of a 500 cm ³ reactor, IPA concentration—about 370 ppm	The highest photocatalytic activity was observed for sample calcined at 700 °C—H ₂ and O ₂ evolution rate was 70 and 24 μmol h ^{−1} , respectively Sample prepared from silver acetate and sodium carbonate showed higher photoactivity in 2-propanol photodegradation—acetone evolution rate was 220 ppm h ^{−1} g ^{−1}	[235]
Nb ₂ O ₅	Fe, Ni, Co, Ag	Nb ₂ O ₅ was suspended in NaOH (molar ratio 2:1). Suspension was dried at 70 °C for 24 h and calcinated at 550 °C Me/NaNbO ₃ preparation: NaNbO ₃ and metallic nitrates were mixed and calcinated at 400 °C, 4 h	H ₂ evolution (water splitting process)	Irradiation source: medium pressure mercury lamp of 150 W	In the presence of Ag/NaNbO ₃ about 200 μmol of H ₂ was obtained after 2 h of UV–vis irradiation The observed trend during photocatalysis process was as follows: Ag/NaNbO ₃ > NaNbO ₃ > Fe/NaNbO ₃ > Co/NaNbO ₃ > Ni/NaNbO ₃	[236]

Table 4 Continued.

KNbO ₃ based-photocatalysts						
KNbO ₃ precursor	Doping moiety	Synthesis parameters	Model photocatalytic reaction	Experimental conditions	Photocatalytic activity	Ref.
Nb ₂ O ₅	N	Procedure: hydrothermal method, 200 °C, 12 h Mixture of Nb ₂ O ₅ (2 mmol) in 10 cm ³ aqueous KOH (10–30 M) was heated in autoclave N-doped KNbO ₃ : heating a mixture of KNbO ₃ (0.3 g) and urea (1.0 g) at 425 °C for 4 h	Photodegradation of rhodamine B (RhB), orange G (OG), bisphenol A (BPA) and pentachlorophenol (PCP)	0.02 g of KNbO ₃ was added into 30 cm ³ of RhB, OG, BPA or PCP (C ₀ = 20 mg/dm ³) Irradiation source: 200 W xenon arc lamp	Under UV all pure KNbO ₃ samples (nanorods, mixture of cubes and nanorods, microcubes and nanocubes) showed photoactivity in follows the order: nanorods > nanocubes > microcubes > mixture of cubes and nanorods	[225]
Nb ₂ O ₅	–	Procedure: hydrothermal method o-KNbO ₃ : 0.5 g of Nb ₂ O ₅ was added into 20 cm ³ of KOH, then 0.0025 mol SDS was added and placed in autoclave and heated at 180 °C, 48 h c-KNbO ₃ : 3.57 g Nb ₂ O ₅ and 37.69 g KOH water solution were placed in autoclave and heated at 160 °C, 12 h	Water splitting process	0.05 g of KNbO ₃ was dispersed in an aqueous methanol solution (20 cm ³ of CH ₃ OH + 60 cm ³ of H ₂ O) Irradiation source: 250 W Xe arc lamp (λ > 300 nm)	c-KNbO ₃ showed the highest rate for H ₂ generation (1242 μmol h ^{−1} g ^{−1}) than o-KNbO ₃ (677 μmol h ^{−1} g ^{−1})	[246]
Nb ₂ O ₅	–	Procedure: hydrothermal method, 180 °C, 12 h t-KNbO ₃ : 20 g of KOH, K ₂ CO ₃ and 1.89 g Nb ₂ O ₅ were mixed and placed in autoclave o-KNbO ₃ : 22.6 g of KOH, K ₂ CO ₃ and 2.5 g Nb ₂ O ₅ were mixed and placed in autoclave	Water splitting process	0.1 g of KNbO ₃ was dispersed in an aqueous methanol solution (20 cm ³ of CH ₃ OH + 60 cm ³ of H ₂ O) Irradiation source: 300 W Xe arc lamp (λ > 300 nm)	Comparing all three KNbO ₃ phases the photoactivity follows the order cubic > orthorhombic > tetragonal	[112]
Nb ₂ O ₅	–	Procedure: hydrothermal method, 200 °C, 12 h 0.01 mol Nb ₂ O ₅ and KOH (1–10.6 M) were dissolved in 70 cm ³ H ₂ O and transferred into a autoclave	Photodegradation of rhodamine B (RhB)	0.03 g of KNbO ₃ was added into 200 cm ³ of RhB (C ₀ = 40 mg/dm ³) Irradiation source: 300 W Xe lamp	Photoactivity strongly depend on the KNbO ₃ microstructure and follows the order of KNbO ₃ nanocubes (89%) > nanowires (71%) > nanorods (54%) > nanotowers (41%)	[244]
Nb ₂ O ₅	Au	Procedure: hydrothermal method, 180 °C, 48 h 0.5 g of Nb ₂ O ₅ was added into 20 cm ³ of KOH, then 0.0025 mol SDS was added and transferred into a autoclave Au-KNbO ₃ : 0.5 g KNbO ₃ was dispersed in 100 cm ³ of H ₂ O, 2 cm ³ of NH ₃ ·H ₂ O and 5 cm ³ HAuCl ₄ ·3H ₂ O. Suspension was stirred at 80 °C for 1 h and dried, and calcined at 300 °C, 1 h	Photodegradation of rhodamine B (RhB)	0.05 g of KNbO ₃ was added into 50 cm ³ of RhB (C ₀ = 0.01 mM) Irradiation source: 300 W Xe lamp, λ > 420 nm	Au/KNbO ₃ samples showed enhanced photoactivity under either UV or visible-light illumination correlated with size of gold NPs For Au NPs with 10.8 nm in size, the reaction rate under UV and vis light is k = 0.01622 min ^{−1} and 0.0040 min ^{−1} , respectively	[250]
Nb ₂ O ₅	Au	Procedure: hydrothermal method, 160 °C, 12 h KNbO ₃ prepared as reported in [219] Au-KNbO ₃ prepared as reported in [223]	Photodegradation of methylene blue (MB)	0.05 g of KNbO ₃ was added into 20 cm ³ of MB (C ₀ = 4.0 × 10 ^{−5} M) Irradiation source: 300 W Xe lamp, λ > 420 nm	With the increasing size of Au NPs from 4.2 to 10.0 nm, the decomposition rate of MB increased from about 50% to 60% under visible light	[249]

4 h to form the NaNbO₃. The obtained nanowires were straight and smooth with a uniform diameter of about 100 nm and lengths up to several tens of micrometers. Shi et al. reported that adding P123 as a surfactant leads to the formation of uniform single-crystalline NaNbO₃ nanowires and plays a critical role in constructing the uniform nanowires. Their proposed mechanism, as presented in Fig. 9A, involved four steps in the following sequence: (1) aggregation of surfactant micelles, (2) adsorption of niobium hydroxide (Nb₂O₅·xH₂O) and Na⁺ ions onto the surface of the P123 micelles and the interbonding of Na⁺ and Nb₂O₅·xH₂O in the solution, (3) nucleation and crystal growth of Na₂Nb₂O₆·H₂O, leading to the formation of the uniform Na₂Nb₂O₆·H₂O nanowires, and (4) formation of NaNbO₃ nanowires through calcination of the corresponding Na₂Nb₂O₆·H₂O. The photocatalytic activity of NaNbO₃ samples was estimated in H₂ evolution from a methanol/water

solution under UV light irradiation. Compared with NaNbO₃ cubes and NaNbO₃ bulk powders, which were used as reference photocatalysts, NaNbO₃ nanowires showed a much higher photocatalytic activity. The average H₂ evolution rate in the presence of NaNbO₃ nanowires was ca. 13.5 mmol/h under UV light irradiation (λ = 300 nm) [230].

Li et al. reported that, along with the crystal size of the photocatalysts, the crystal structure (particularly crystallographic symmetry) also affects the photocatalytic properties of sodium niobate [129]. They synthesized cubic NaNbO₃ (c-NaNbO₃) and orthorhombic NaNbO₃ (o-NaNbO₃) by furfural alcohol-derived polymerization–oxidation (FAPO) process and the polymerized complex (PC) method, respectively. In furfural alcohol derived polymerization–oxidation process mixture of (C₂H₅O)₅Nb, of C₂H₅ONa and P123 was heated at 95 °C for 120 h and obtained

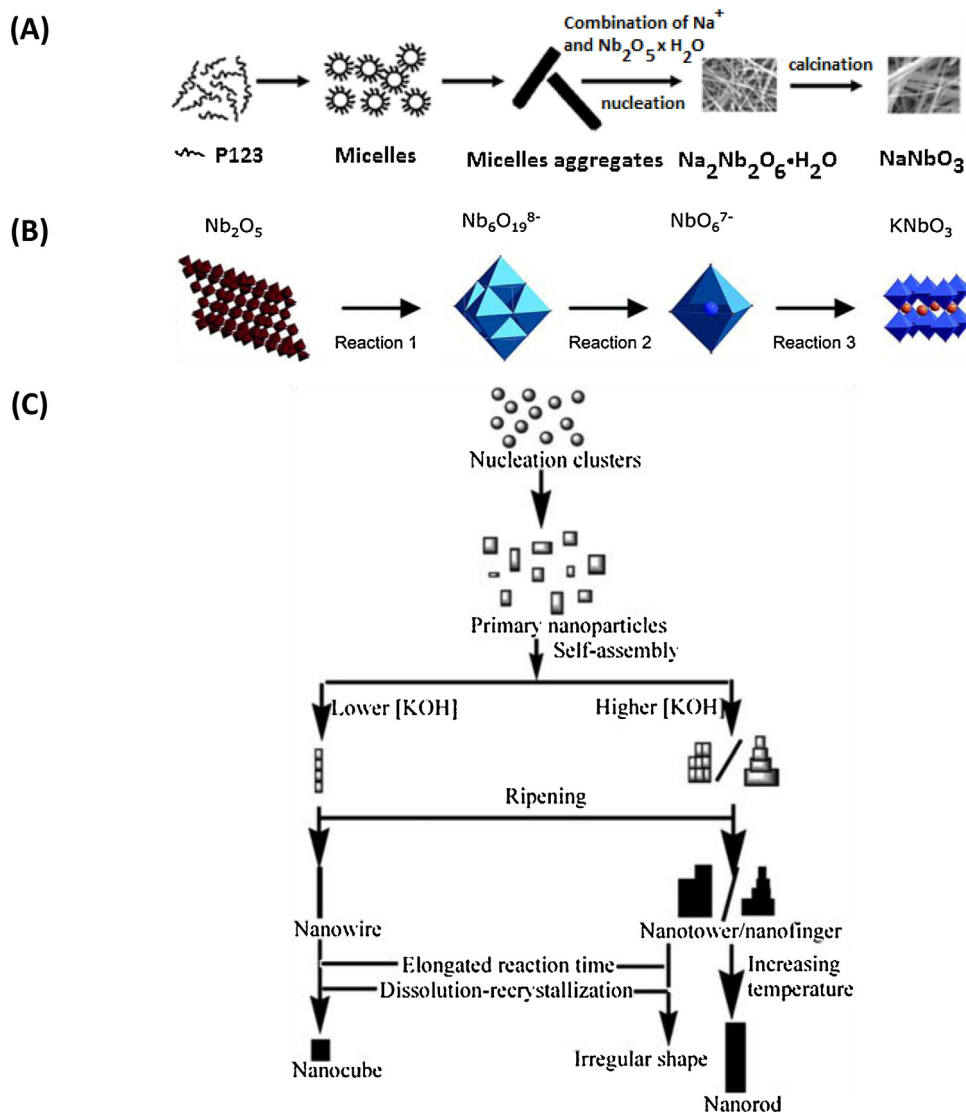


Fig. 9. Possible mechanism of: (A) growth of NaNbO₃ nanowires proposed by Shi et al. Reprinted from Ref. [230], (B) structural transformations of Nb-containing species along the chemical mechanism of KNbO₃ proposed by Magrez et al. Reprinted from Ref. [243], (C) growth of KNbO₃ nanostructures proposed by Jiang et al. Reprinted from Ref. [244].

black solid was oxidized in air at 600 °C for 5 h. While, in the polymerized complex method solution containing NbCl₅, Na₂CO₃, citric acid and ethylene glycol was heated at 120 °C for 20 h and was oxidized in air at 600 °C for 2 h. The UV–vis absorption spectra of c-NaNbO₃ exhibited a slight red shift, suggesting that the cubic form of NaNbO₃ absorbs longer wavelength light. The energy band gaps of c-NaNbO₃ and o-NaNbO₃ are 3.29 and 3.24 eV, respectively. The photocatalytic activity was measured in H₂ evolution from aqueous methanol solution and CO₂ photoreduction in the gas phase. In both cases, Li et al. observed that c-NaNbO₃ showed nearly twice the photoactivity of o-NaNbO₃. The difference in the photoactivity may be due to differences in the electronic structure of the two phases of NaNbO₃, which is caused by the variant octahedral ligand field. Moreover, the high symmetry in c-NaNbO₃ results in the photogenerated electrons having a smaller effective mass and higher migration ability [129].

Concluding, NaNbO₃ with the special morphology, such as nanowire, has been reported that it exhibited higher activity in comparison with the sample prepared by the solid state reaction method. Probably, the photocatalytic activity of the solid solutions was low because of the small surface area of the sample caused

by high sintered temperature in the SSR method. Further efforts on reducing particle sizes by selecting an appropriate synthesizing method are indispensable to enhance photocatalytic activity of these materials. Additionally, most of reported photocatalytic measurements were carried out over orthorhombic NaNbO₃ few research has been done over the other phases of NaNbO₃ so a systematic research is still needed for better understanding the effects of surface morphology on photocatalytic properties.

5.2. Modified NaNbO₃

Nitrogen doping is an effective method for modifying light absorption behavior. In view of this, N-doped NaNbO₃ (NaNbO_{3-x}N_x) powders were obtained by Shi et al. [224]. Na₂CO₃ and Nb₂O₅ were used as a starting materials. NaNbO₃ powders were doped with N under gaseous ammonia flow over the temperature range 545–590 °C for 3 h. UV–vis diffuse reflectance spectra indicated that, nitrogen doping caused an increase in the optical absorption of the samples in the visible-light region. Pure NaNbO₃ and N-doped NaNbO₃ had absorption edges at 365 nm and 480 nm, respectively. Moreover, Shi et al. observed that the visible light

absorption increased with increase in the temperature used during nitriding. XPS results showed that N atoms were substituted at the O sites in NaNbO_3 . Additionally, based on the intensity of N 1s peak, it was observed that the amount of N doping increased with increasing reaction temperature. The photocatalytic activity of $\text{NaNbO}_{3-x}\text{N}_x$ samples was measured in the photodecomposition of 2-propanol, used as a model organic compound, into acetone, and mineralization of acetone into CO_2 . The highest visible-light photocatalytic activity was observed for the sample annealed at 560°C . Shi et al. suggested that differences in the photoactivity of the N-doped samples could be attributed to the amount of N doping. Nitrogen doping improves visible-light absorption, but higher amounts of N can generate more electron–hole recombination centers, which leads to a decrease in photoactivity [224].

The photocatalytic activity of $\text{In}_2\text{O}_3/\text{NaNbO}_3$ in H_2 evolution under visible and ultraviolet light was studied by Lv et al. [234]. $\text{In}_2\text{O}_3/\text{NaNbO}_3$ samples were synthesized by a coprecipitation method. InCl_3 and $\text{Nb}(\text{OC}_2\text{H}_5)_5$ were used as precursors. The morphology analysis of samples indicated that pure NaNbO_3 was rod-like, exhibiting rods of ca. 100 nm width and length of more than $1\text{ }\mu\text{m}$. In_2O_3 was in the form of nanoparticles, while both rods and particles could be found in $\text{In}_2\text{O}_3/\text{NaNbO}_3$ composites. In_2O_3 appeared to have grown on the surface of the NaNbO_3 rods. Lv et al. reported that $\text{In}_2\text{O}_3/\text{NaNbO}_3$ was a good photocatalyst for H_2 evolution under visible-light irradiation. Moreover, they observed that on increasing the In concentration from 0 to 37.5 at%, the activity of $\text{In}_2\text{O}_3/\text{NaNbO}_3$ increased. For $\text{In}_2\text{O}_3/\text{NaNbO}_3$ containing 37.5 at% In, the amounts of H_2 evolved under visible or ultraviolet light irradiation were 13.2 and $44.6\text{ }\mu\text{mol h}^{-1}\text{ g}^{-1}$, respectively [234].

Li et al. prepared NaNbO_3 and $\text{Na}_{0.6}\text{Ag}_{0.4}\text{NbO}_3$ powders using the PC method, following previous promising results in which $\text{NaNbO}_3\text{--AgNbO}_3$ samples obtained by the SSR method exhibited good visible-light photocatalytic activities [235,245]. Pure NaNbO_3 was synthesized similarly to the earlier work, and was finally calcined at different temperatures from 500 to 900°C for 1 h in air [229,235]. For the $\text{Na}_{0.6}\text{Ag}_{0.4}\text{NbO}_3$ samples, different starting materials were used: silver acetate ($\text{Ag}(\text{Ac})$) with sodium carbonate (Na_2CO_3), and silver nitrate (AgNO_3) with sodium nitrate (NaNO_3). Li et al. reported that the average particle size directly depended on the calcination temperature, and increased from 40 to 540 nm on increasing the thermal treatment temperature from 600 to 900°C . The photocatalytic activity of NaNbO_3 was evaluated in the water splitting reaction in the presence of a RuO_2 co-catalyst. The highest photocatalytic activity was observed for the sample calcined at 700°C , which had a nanocrystallite size of ca. 34 nm , and exhibited H_2 and O_2 evolution rates of 70 and $24\text{ }\mu\text{mol h}^{-1}$, respectively. It is well known from the literature that the nanocrystallite size has a strong influence on photocatalytic activity. Moreover, Li et al. reported that critical nanocrystallite size may be relevant to the Debye length (L_{Deb}), which is defined as the distance between an electron and a hole formed during photoirradiation. The electrons and holes can more easily reach the surface and be trapped in the surface active sites when the nanocrystallite size is smaller than L_{Deb} [235]. The photocatalytic activity of $\text{Na}_{0.6}\text{Ag}_{0.4}\text{NbO}_3$ was measured in 2-propanol decomposition by measuring the acetone evolution rate. It was observed that the sample prepared from $\text{Ag}(\text{Ac})$ and Na_2CO_3 showed higher photoactivity, with an acetone evolution rate of $220\text{ ppm h}^{-1}\text{ g}^{-1}$ [235].

M/NaNbO_3 ($\text{M}=\text{Fe}, \text{Ni}, \text{Co}, \text{or Ag}$) photocatalysts were synthesized by Zielińska et al. by a wet impregnation method [236]. Nb_2O_5 and NaOH were used as precursors for the preparation of NaNbO_3 and $\text{Fe}(\text{NO}_3)_3\cdot 9\text{H}_2\text{O}$, $\text{Co}(\text{NO}_3)_2\cdot 6\text{H}_2\text{O}$, $\text{Ni}(\text{NO}_3)_2$ and AgNO_3 as metal sources. Phase analysis of Fe/NaNbO_3 , Ni/NaNbO_3 , Co/NaNbO_3 , and Ag/NaNbO_3 showed that the characteristic diffraction peak of NaNbO_3 was detected in all samples. Additionally, in the case of the Ag/NaNbO_3 and Ni/NaNbO_3 samples,

the diffraction peaks of Ag_2O and NiO phases were also detected. Based on TEM images, it was noted that all the photocatalysts exhibited high crystallinity. To calculate the band gap energy, Zielińska et al. used the Kubelka–Munk method based on UV–vis spectra. For pristine NaNbO_3 and Ni/NaNbO_3 , the estimated values of E_g were 3.34 and 3.62 eV , respectively. In the case of the Co/NaNbO_3 sample, three E_g values were calculated (3.16 , 2.38 , and 1.60 eV). The E_g values of 3.16 and 1.60 eV are characteristic of Co_3O_4 . Similarly, three band gap values of 3.20 , 2.29 , and 1.48 eV for Fe/NaNbO_3 were observed. The E_g of 2.29 eV can be attributed to Fe_2O_3 . For Ag/NaNbO_3 , two band gaps of 1.08 and 3.34 eV were observed. Based on literature data, the Ag_2O band gap values range from 1.20 to 3.4 eV [236]. The photocatalytic activity of the obtained samples was measured in the H_2 generation reaction. Only the sample modified with Ag exhibited higher photoactivity than pure NaNbO_3 . In the presence of Ag/NaNbO_3 , ca. $200\text{ }\mu\text{mol}$ of H_2 was obtained after 2 h of UV–vis irradiation. The photocatalytic activity of the samples followed the trend $\text{Ag}/\text{NaNbO}_3 > \text{NaNbO}_3 > \text{Fe}/\text{NaNbO}_3 > \text{Co}/\text{NaNbO}_3 > \text{Ni}/\text{NaNbO}_3$ [236].

Concluding, among many Nb-based mixed metal oxides, sodium niobate is a promising photocatalytic material. However, its wide band gap (3.4 eV) is too large to be activated under visible-light irradiation. In view of this, it is a challenge to successfully prepared a visible-light-sensitive photocatalysts based on NaNbO_3 . Actually, there are few reports about Nb-based photocatalysts active under visible irradiation, so development of highly efficient photocatalysts is still needed.

5.3. Pristine KNbO_3

Potassium niobate is a perovskite with low toxicity characterized by high stability under light irradiation. KNbO_3 presents temperature-dependent crystalline phases, including orthorhombic, tetragonal, and cubic. The cubic phase of KNbO_3 is crystallized at temperatures higher than 437°C , while the orthorhombic phase is formed at 200°C . KNbO_3 has been mainly studied in photocatalytic water splitting and dye photodegradation [35,37,112,225,246–248]. KNbO_3 in orthorhombic phase has $\text{Cm}2m$ space group with lattice constants of $a=0.5695$, $b=0.5721$, and $c=0.3973\text{ nm}$, cubic phase KNbO_3 has $\text{Pm}3m$ space group with a lattice constant of $a=0.4022\text{ nm}$, while tetragonal KNbO_3 has $\text{P}4mm$ space group [112,225,243,246,248,249].

The photocatalytic properties of KNbO_3 nanowires were investigated by Ding et al. in water splitting [37]. Photocatalysts was obtained via hydrothermal method where Nb_2O_5 was mixed with KOH solution, heated in autoclave at 150°C for 1 week and finally and dried at 120°C for 10 h. Nanowire structures of several micrometers in length and ca. 100 nm in diameter were confirmed using SEM images. The band gap of orthorhombic KNbO_3 was estimated to be 3.2 eV . The photocatalytic water splitting process in the presence of KNbO_3 was carried out under UV–vis irradiation. As a reference material, KNbO_3 powder synthesized via solid state reaction and KNbO_3 nanocubes obtained by the hydrothermal method, were used. The H_2 evolution for nanowires, nanocubes, and powder were 1.03 , 0.42 , and 0.79 mmol h^{-1} , respectively. The high photoactivity of KNbO_3 nanowires was probably due to its higher surface area ($8.50\text{ m}^2\text{ g}^{-1}$) than that of nanocubes and KNbO_3 powder (6.13 and $2.31\text{ m}^2\text{ g}^{-1}$, respectively) [37].

Hayashi et al. obtained potassium niobate powders by hydrothermal synthesis under various subcritical (300°C) and supercritical (400°C) water conditions [247]. Nb_2O_5 and KOH were used as starting materials. XRD analysis showed that the sample obtained under subcritical water conditions exhibited only a single $\text{K}_4\text{Nb}_6\text{O}_{17}$ phase, while mixed phases of $\text{K}_4\text{Nb}_6\text{O}_{17}$ and KNbO_3 were obtained under supercritical water conditions. Moreover, it

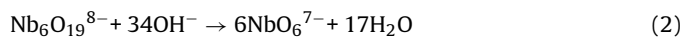
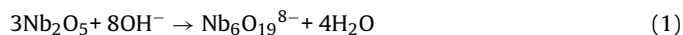
was observed that transformation from the $K_4Nb_6O_{17}$ phase to the $KNbO_3$ phase depended on heating duration. When heating time at 400 °C was increased from 2 to 8 h, the K/Nb molar ratio increased from 0.63 to 0.96. Heating time also influenced the absorption properties of $KNbO_3$. The absorption edges for $KNbO_3$ heated for 2 and 4 h were observed at ca. 380 nm, while the corresponding values were between 350 and 400 nm for samples heated for 8 and 24 h. Photocatalytic activity was measured in H_2 evolution from water decomposition. The highest photoactivity was observed for the sample synthesized at 400 °C for 4 h under supercritical conditions, which afforded a H_2 evolution rate of ca. $17.7 \mu\text{mol g}^{-1} \text{h}^{-1}$ [247].

Yan et al. prepared $KNbO_3$ with cubic (c- $KNbO_3$) and orthorhombic (o- $KNbO_3$) phases by hydrothermal process and tested the obtained powders in photocatalytic water splitting [246]. In the synthesis of o- $KNbO_3$ submicro-rods mixture of Nb_2O_5 , KOH and sodium dodecyl sulfate (SDS) was heated at 180 °C for 48 h. For the synthesis of c- $KNbO_3$ submicro-cubes Nb_2O_5 and KOH were heated at 160 °C for 12 h. Analysis of their morphology showed that the average lengths of o- $KNbO_3$ and c- $KNbO_3$ were 200 and 300 nm, respectively, while their average widths were ca. 150 and 250 nm, respectively. Both cubic and orthorhombic $KNbO_3$ showed higher photoreactivity than commercial bulk $KNbO_3$ powders. c- $KNbO_3$ showed a higher rate of H_2 generation ($1242 \mu\text{mol h}^{-1} \text{g}^{-1}$) than o- $KNbO_3$ ($677 \mu\text{mol h}^{-1} \text{g}^{-1}$). Yan et al. calculated that the band gaps of o- $KNbO_3$ and c- $KNbO_3$ were 3.25 and 3.24 eV, respectively. Moreover, based on XPS analysis, they observed a difference in Nb 3d binding energy between c- $KNbO_3$ and o- $KNbO_3$ (0.2 eV). Based on these results, it was suggested that the electronic structure of these samples was different. Cubic and orthorhombic $KNbO_3$ have the same valence band level, but the bottom of the conduction band could be different. From the literature data, it is known that the surface properties of a photocatalyst, especially those of the exposed crystal facets, play an important role in heterogeneous photocatalysis; therefore, c- $KNbO_3$ with high crystallographic symmetry can facilitate the excitation and transfer of photogenerated electrons. Differences in active sites between these two phases have an influence on the separation, mobility, and lifetime of their photogenerated charges, and thus on their resulting photocatalytic activities [246].

The photoreactivity of cubic, orthorhombic, and tetragonal $KNbO_3$ microcubes was also investigated in hydrogen evolution from aqueous methanol under UV light by Zhang et al. [112]. Tetragonal $KNbO_3$ microcubes were hydrothermally synthesized by heating Nb_2O_5 and KOH solution at 180 °C for 12 h. Orthorhombic $KNbO_3$ microcubes were obtained using the same procedure, where only difference was the amounts of KOH and Nb_2O_5 were used. The band gap values of hydrothermally synthesized orthorhombic (o- $KNbO_3$) and tetragonal (t- $KNbO_3$) microcubes were 3.15 and 3.08 eV, respectively. SEM images showed that the average edge lengths of o- $KNbO_3$ and t- $KNbO_3$ microcubes were ca. 1.0 and 3.3 μm , respectively. To enhance the photocatalytic activity in water splitting for H_2 production, Pt NPs were deposited on the $KNbO_3$ surface to act as a co-catalyst. Moreover, Zhang et al. reported that, under UV irradiation, Pt NPs react as electron-trapping centers and prevent charge recombination. A comparison of all three $KNbO_3$ phases shows that the photoactivity follows the order cubic > orthorhombic > tetragonal. These results are similar to data obtained by Yan et al. [246]. Higher symmetry in the crystal structure of cubic $KNbO_3$ led to higher photocatalytic activity. Moreover, Zhang et al. reported that photogenerated electrons cannot be transferred isotropically in o- $KNbO_3$ and t- $KNbO_3$ [112].

Jiang et al. investigated the influence of KOH concentration, reaction temperature, and reaction time on the formation of different $KNbO_3$ morphologies, including nanowires, nanotowers, nanocubes, and nanorods [244]. $KNbO_3$ samples were prepared

by hydrothermal synthesis (200 °C, 12 h; precursors: Nb_2O_5 and KOH). They reported that, by differing these synthesis conditions, the morphology of $KNbO_3$ could be easily controlled [244]. They prepared various $KNbO_3$ nanostructures such as nanowires, nanotowers, nanocubes, and nanorods, and a possible growth mechanism for the obtained structures was suggested. Analysis of the relationship between KOH concentration (1, 5, 6.6, 7.5, 9.5, 10.6, and 12.75 M) and the $KNbO_3$ crystallinity showed that when the concentration increased over 5 M, all XRD diffraction peaks originate from the pure $KNbO_3$ phase. The reactions occurring in solution can be summarized as follows [243,244]:



The structure of the Nb-containing species is presented in Fig. 9B [243].

Moreover, Jiang et al. observed that the reaction time in which pure $KNbO_3$ phase was achieved was shorter at higher KOH concentration. For example, when the concentration of KOH was 6.5 and 10.6 M, the same amount of pure phase $KNbO_3$ was obtained after 12 and 6 h of thermal treatment at 200 °C, respectively. The KOH concentration also had a significant influence on the morphology of the obtained samples. With increasing KOH concentration, the following structures were obtained: (i) KOH = 6.5 M: a large quantity of aggregated nanowires 200–300 nm in length and 10–20 nm in diameter; (ii) KOH = 7.5 M: nanotowers started to form; (iii) KOH = 10.6 M: nanotowers consisting of stacked cube-shaped particles of different sizes appeared, and the cube size decreased in a stepped way with random step heights toward the nanofinger tip; and (iv) KOH = 12.75 M: nanotowers composed of nanocubes with non-uniform sizes were observed.

To evaluate the effect of reaction temperature on $KNbO_3$ formation, hydrothermal reaction was carried out for 12 h at different temperatures from 120 to 250 °C at a constant KOH concentration of 10.6 M. Pure $KNbO_3$ phase was obtained at 150 °C and higher. Additionally, with increasing reaction temperature, the intensity of the XRD diffraction peaks also increased. Moreover, at 150 °C, nanotowers with long nanofingers of up to several micrometers at the tip were observed. After increasing the temperature to 250 °C, the tips of the nanofingers disappeared and irregular $KNbO_3$ aggregates mixed with nanorods (1 μm in length and 200 nm in diameter) were obtained. Finally, the influence of reaction time was investigated. The suspension was hydrothermally treated for 3 h, 6 h, 12 h, 36 h, and 7 days at 200 °C employing a KOH concentration of 10.6 M. A pure crystal $KNbO_3$ phase was obtained after 6 h of reaction, and the crystallinity was enhanced by increasing the reaction time to 7 days [244]. Based on these results, Jiang et al. proposed a growth mechanism for the $KNbO_3$ nanostructures (Fig. 9C). They suggested that, based on Eqs. (1)–(3), the synthesis takes place via a dissolution–precipitation process where Nb_2O_5 first dissolves into $Nb_6O_{19}^{8-}$ and next into single octahedral NbO_6^{7-} anions. Finally, the $KNbO_3$ forms according to equation (3). Because the HT reaction took place in the pure Nb_2O_5 and KOH solution, the mechanism formation of different $KNbO_3$ nanostructures is neither catalyst-assisted nor a template-assisted. In the first step after mixing the reactants at high temperature, the cube-shaped NPs started to form. With 6.5 M KOH, cubic crystals started to aggregate along the (110) or (001) direction and nanowires were formed. At higher KOH concentrations (>6.5 M), nanotowers formed from cubic particles of different sizes. Further increasing the KOH concentration led to a shortening of the nanotowers, and structures similar to the previous cubes, which were the basic forms for the growth of the next cubes, were clearly observed. $KNbO_3$ nanorods were obtained from nanofingers/nanotowers upon increasing the tem-

perature to 250 °C. Because of the difference in solubility between the large and small particles, the nanorods and the irregular aggregates grew at the cost of the smaller ones on the tips of the nanotowers [244]. The photocatalytic activity of the obtained structures was measured in the decomposition of Rhodamine B under UV–vis irradiation. Jiang et al. reported that the photoactivity strongly depended on the KNbO_3 microstructure, and followed the order KNbO_3 nanocubes (89%) > nanowires (71%) > nanorods (54%) > nanotowers (41%) [244].

Concluding, hydrothermal synthesis, which involves heating Nb_2O_5 in various concentrations of aqueous KOH to 120–200 °C, appears to be the most convenient and versatile method to obtain KNbO_3 photocatalysts. Depending on the reaction conditions, KNbO_3 of various sizes and shapes have been obtained, including micro and nanorods, wires and cubes.

5.4. Modified KNbO_3

Wang et al. investigated the influence of KOH concentration (10–30 M) on the morphology of KNbO_3 synthesized by hydrothermal method (200 °C, 12 h; precursors: Nb_2O_5 and KOH) [225]. N-doped KNbO_3 was prepared by heating a pure KNbO_3 and urea at 425 °C in air for 4 h. Field emission scanning electron microscopy analysis showed that different shapes were obtained under different KOH concentration. Nanorods of 1.7–6.5 μm in length and 90–230 nm in diameter were obtained using 10 M KOH; a mixture of irregular cubes and nanorods with side lengths in the range 0.2–0.9 μm were produced when the KOH concentration was increased to 13 M; microcubes with 600–1300 nm side lengths formed when 16 M KOH solution was used; and nanocubes with sizes ranging from 150 to 450 nm were synthesized using 30 M KOH. XRD showed that all the obtained photocatalysts exhibited the orthorhombic phase of KNbO_3 . Moreover, N-doped KNbO_3 nanocubes were prepared using urea as a N source. The results showed that the surface of nanocubes changed after doping and became slightly rough, and that N doping occurred on the surface of the nanocubes. The band gap of pure KNbO_3 (3.01–3.22 eV, depending on the particle shape) and N- KNbO_3 (2.28 eV), calculated on the basis of UV–vis diffuse reflectance spectra, indicated that N doping resulted in a decreased band gap and enhanced visible-light absorption of the semiconductor. The photocatalytic activity of KNbO_3 photocatalysts was measured by the photodegradation of four organic contaminants (RhB, orange G, bisphenol A, and pentachlorophenol) under UV–vis and visible-light ($\lambda > 420 \text{ nm}$) irradiation. Under UV irradiation, all pure KNbO_3 photocatalysts (nanorods, mixture of cubes and nanorods, microcubes, and nanocubes) showed photoactivity in the following order nanorods > nanocubes > microcubes > mixture of cubes and nanorods. Wang et al. explained that the low photoactivity of the mixture of cubes and nanorods is a result of their small surface area and lower number of active sites on the photocatalyst surface. The higher photoactivity of pure nanorods corresponded to more efficient light scattering and absorption of the rods (due to their high length-to-diameter ratio) and more rapid electron transport along the rods. All pure KNbO_3 photocatalysts were inactive under visible-light irradiation ($\lambda > 420 \text{ nm}$), while all organic compounds were efficiently decomposed in the presence of N- KNbO_3 . Wang et al. proposed a mechanism for the visible-light photocatalytic activity of N- KNbO_3 (Fig. 10). They suggested that nitrogen doping leads to N 2p states isolated above the VB of KNbO_3 , which are responsible for absorption enhancement in the visible region. Under visible light, electron and hole pairs are generated between the surface N 2p states and the CB of Nb 4d, which produces $\cdot\text{OH}$ radicals [225].

One-dimensional KNbO_3 nanowires modified with gold NPs were obtained by Lan et al. using hydrothermal treatment [250]. In

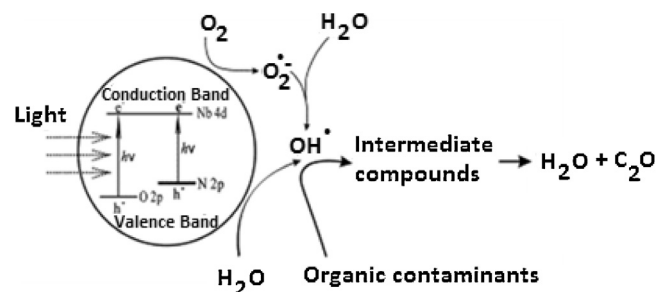


Fig. 10. Possible mechanism of visible light activity and band structure of N- KNbO_3 photocatalyst proposed by Wang et al. Reprinted from Ref. [225].

the synthesis of KNbO_3 mixture of Nb_2O_5 , KOH and sodium dodecyl sulfate (SDS) was heated at 180 °C for 48 h. Gold modified KNbO_3 nanostructures were prepared using the deposition–precipitation method where tetrachloroaurate (III) trihydrate ($\text{HAuCl}_4 \cdot 3\text{H}_2\text{O}$) was used as a gold precursor. Rod-like KNbO_3 and commercial bulk-like powder were used as reference photocatalysts. The XRD peaks indicated that no other phases except orthorhombic KNbO_3 were present. The band gap for nanowires, nanorods, and commercial KNbO_3 were 3.81, 3.74, and 3.37 eV, respectively. Characteristic surface plasmon resonance with an absorption maximum of ca. 550 nm was observed for gold NPs supported on KNbO_3 nanowires. SEM images showed that KNbO_3 nanowires had length and width of up to 2 and 0.15 μm , respectively. The photocatalytic activity of the obtained samples was measured in the decomposition of RhB under UV and visible-light irradiation. Pure nanorods and commercial KNbO_3 exhibited a lower degradation rate of RhB than nanowires under UV irradiation. Based on this result, KNbO_3 nanowires were selected as a substrate for Au NP modification (5–10 wt%). Lan et al. reported that Au/ KNbO_3 samples showed enhanced photoactivity under both UV and visible-light illumination correlated with the size of the Au NPs. Increasing the size of the Au NPs from 5.8 to 10.8 nm enhanced the photoreactivity under UV and visible-light illumination. It is also worth mentioning that the photocatalytic activity under UV irradiation of Au/ KNbO_3 nanocomposites is much greater than that under visible-light. Lan et al. explained that interfacial charge transfer between Au and KNbO_3 under light irradiation, surface plasmon resonance, and interband transitions on Au NPs are responsible for its enhanced photocatalytic activity [250].

The influence of Au NPs on the surface of KNbO_3 microcubes (average side length ca. 700 nm) on their photocatalytic activity of methylene blue (MB) degradation under visible-light ($\lambda > 420 \text{ nm}$) was investigated by Yan et al. [249]. Based on XPS measurements, it was reported that Nb 3d_{5/2} and Nb 3d_{3/2} are located at 206.5 and 209.3 eV, respectively, but after Au NP deposition on the KNbO_3 surface, the Nb 3d core-level binding energy increased by 0.4 eV. Yan et al. suggested that this shift corresponded to electron transfer from KNbO_3 microcubes to Au NPs, which was responsible for enhancing the photocatalytic activity. Pure KNbO_3 samples showed absorption only at wavelengths less than 400 nm. For samples loaded with 3 wt% and 6 wt% gold NPs, characteristic photoabsorption at ca. 550 and 570 nm was observed, related to the intrinsic surface plasmon resonance effects of Au NPs. Differences in absorption corresponded to differences in the size of Au particles deposited on the KNbO_3 . High-resolution TEM images confirmed that spherical Au NPs were highly dispersed on the KNbO_3 surface. Moreover, the mean sizes of the Au NPs for 3 wt% and 6 wt% Au deposited on KNbO_3 were $4.2 \pm 0.6 \text{ nm}$ and $10.0 \pm 1.3 \text{ nm}$, respectively. The photocatalytic activity of the obtained samples was dependent on the size of the Au NPs. On increasing the size of Au NPs from 4.2 to 10.0 nm, the decomposition of MB increased. Yan et al. explained that D–sp interband transitions and the surface plasmon

Table 5
Perovskite-based photocatalysts for organic compounds degradation and hydrogen or oxygen evolution.

Type of photocatalyst	Band gap (eV)	Crystal structure	Degradation effect and comments	Ref.
Rh-BaTiO ₃	3.3	Cubic	Rh-BaTiO ₃ achieved stoichiometric water splitting into H ₂ and O ₂ under visible light according to the Z-scheme principle.	[24]
Cu-CaTiO ₃	3.6	Cubic or orthorhombic	CaTiO ₃ -doped with 2 mol% Cu ²⁺ exhibits the highest activity to the photocatalytic decomposition of water. New band gap in the visible-light range was obtained by copper-doped CaTiO ₃	[253]
Ag/La-CaTiO ₃		Cubic	Co-doping of Ag and La at CaTiO ₃ narrowed the band gap and enhanced visible light absorption and photocatalytic activity under visible light ($\lambda > 400$ nm) during water splitting process	[99]
NiTiO ₃	2.18	Rhombohedral	NiTiO ₃ nanorods exhibit better photocatalytic activity under visible light irradiation ($\lambda > 420$ nm) than commercial TiO ₂ (Degussa P25)	[26]
CdTiO ₃	2.8	Orthorhombic	CdTiO ₃ nanofibers were studied during photodegradation of Rhodamine 6G (R6G) dye under UV irradiation	[104]
AgTaO ₃	3.4	Rhombohedral	NiO/AgTa _{0.7} Nb _{0.3} O ₃ photocatalyst achieved stoichiometric water splitting into H ₂ and O ₂ under visible light irradiation	[28]
β -AgVO ₃	2.25	Monoclinic	β -AgVO ₃ nanowires showed excellent photoactivity in degradation of Rhodamine B dye under simulated sunlight	[260]
Ag- β -AgVO ₃	2.0	Monoclinic	Ag/AgVO ₃ exhibited higher photocatalytic activity than bare β -AgVO ₃ under visible light ($\lambda > 420$ nm) irradiation during the degradation of bisphenol A	[94]
LaFeO ₃	2.1	Cubic or orthorhombic	LaFeO ₃ cubes, rods and spheres were synthesized. The photocatalytic activities of LaFeO ₃ nanostructures in degradation of RhB under visible light irradiation ($\lambda > 400$ nm) was higher than commercial TiO ₂ (Degussa P25)	[42]
YFeO ₃	2.58	Orthorhombic	YFeO ₃ showed photocatalytic activity four times that of TiO ₂ -P25 under >400 nm visible light irradiation ($\lambda > 400$ nm) (Rh B degradation)	[86]

resonance of Au NPs can generate electrons that are transferred to the CB of KNbO₃. In the next step, O molecules capture electrons and generate HO₂[•] or OH[•] radicals, which are directly involved in the MB degradation process [249].

Concluding, pure KNbO₃ can only be excited by UV light due to its large band gap (3.14–3.24 eV). Aiming at utilizing the full solar spectrum in photocatalytic processes, modifications of KNbO₃ by doping non metallic species such as nitrogen and loading metal nanoparticles (e.g. Au NPs) can enhanced the photocatalytic activity. However to date, systematic studies on photocatalysis by modified KNbO₃ nanostructures are still lacking.

6. Other perovskite-based photocatalysts

Among the large number of perovskite-based compounds (over 80), other titanates (ATiO₃, where A = Ba, Ca, Mn, Co, Fe, Pb, Cd, or Ni), tantalates, niobates, vanadates, and ferrites show promising photocatalytic performance under visible irradiation ($\lambda > 400$ nm) because of their unique properties, but detailed studies of these materials still need to be performed.

BaTiO₃, a wide-gap metal oxide having perovskite structure, has attracted extensive attention due to its excellent photocatalytic performance in the splitting of water into H₂ and O₂ [24,251,252]. Recently, CaTiO₃ perovskite has received particular attention as a promising material for photoelectrochemical water splitting because it has a similar band structure to TiO₂, matches the energy levels of water splitting, and has no defects or recombination centers [253–255]. NiTiO₃, ($E_g = 2.18$ eV), has been widely investigated for its suitable band gap and unique photoresponse in the visible-light region for photocatalysis [105,256]. NiTiO₃ has a structure in which both Ni and Ti prefer octahedral coordination with alternating cation layers occupied by Ni and Ti alone [26]. CdTiO₃ is regarded as an intelligent material with promising applications because of its excellent dielectric, ferroelectric, pyroelectric, piezoelectric, photorestrictive, magnetorestrictive, and electro-optical properties, and has also been used as a photocatalyst [104,257,258]. Among vanadium oxides, AgVO₃ has potential applications in rechargeable high-energy density lithium batteries and photocatalysts due to its excellent elec-

trochemical and photophysical properties [259]. Ag-containing perovskite materials have been used as a good visible-light responsive photocatalysts in the photocatalytic splitting of water into H₂ and O₂ [39]. Because α -AgVO₃ and β -AgVO₃ possess an intense absorption band in the visible-light region (band gap <2.5 eV), they can be used in photocatalytic processes under visible-light irradiation [39,93,94,260–262]. Semiconducting perovskite lanthanum orthoferrite (LaFeO₃) nanostructures are one of the most common perovskite-type oxides and are a promising material that can act as an efficient visible-light photocatalyst due to its narrow band gap energy and unique optoelectronic properties [42,70,75,85,263–266]. Pure YFeO₃ is a *p*-type indirect semiconductor ($E_g = 2.58$ eV). Literature data show that YFeO₃ can be used as a photocatalyst [67,86,88,267]. In Table 5, a short summary of promising photocatalytic materials for organic compound degradation and H₂ or O₂ evolution are presented.

7. Conclusion and perspectives

The object of this article was to provide a brief review of the advances in the design of selected perovskite oxides, including several methods for their preparation with different morphologies, complex characterization, and the applications of perovskites in photocatalysis.

The perovskite crystal structure offers an excellent framework upon which to tune band gap values to enable visible-light absorption and band edge potentials to suit the needs of specific photocatalytic reactions. Moreover, lattice distortion in perovskite compounds strongly influences the separation of photogenerated charge carriers. These bulk and surface properties significantly affect the separation, mobility, and lifetime of the photogenerated electrons and holes. Because the VBs of perovskite oxides consisting of *d*⁰ transition metal ions are usually formed with O 2*p* orbitals (the CBs of ATaO₃ (A = Na, K) and ANbO₃ (A = Na), consist of Ta 5*d* and Nb 4*d*, respectively), the difference in band gaps is mainly attributed to the potential difference in CBs (see Fig. 11). Based on these data, it can be expected that the higher the CB level is, the higher the photocatalytic activity is. In this regard, engineering nano-, submicro- and microcrystalline photocatalysts in terms of their structure and mor-

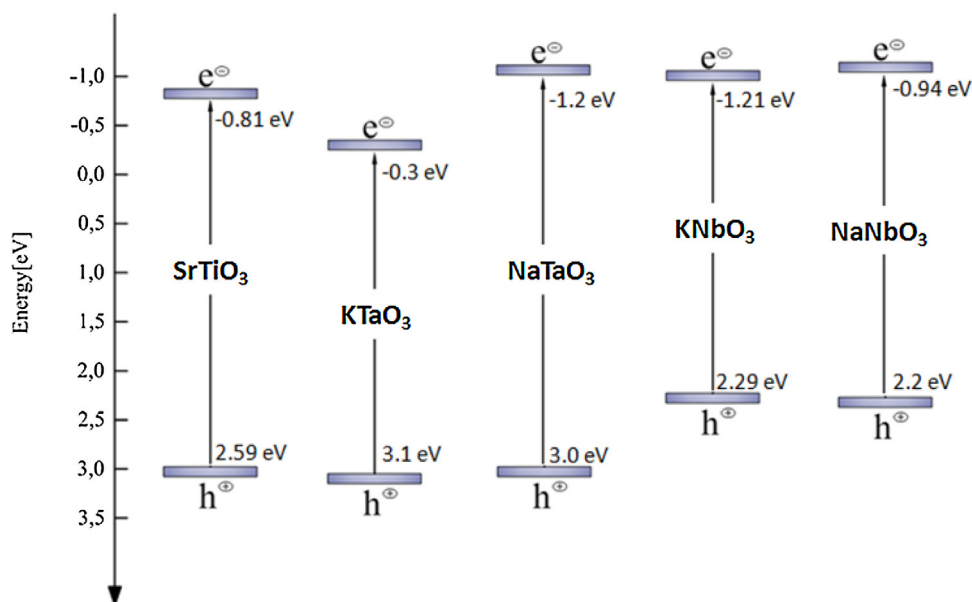


Fig. 11. Band structures of SrTiO₃, KTaO₃, NaTaO₃, KNbO₃ and NaNbO₃.

phology is one of the most promising approaches to highly efficient photocatalytic processes.

Tanaka et al. proposed the basic strategies for designing perovskite (ABO₃, where A is a rare earth metal and B is a first row transition metal) materials for photocatalytic performance [17]:

- Selection of B-site elements.
- Valency and vacancy controls.
- Synergistic effects, mainly of B-site elements.
- Enhancement of surface area by forming fine particles or dispersing on supports.
- Addition of precious metals with their regeneration method.

Most of the characterized perovskite photocatalysts were obtained by the hydrothermal method, which is widely used to generate samples with high crystallinity and purity. Presented results confirmed that ABO₃-photocatalysts synthesized by hydrothermal/solvothermal reactions have fewer defects, smaller sizes, larger surface areas, and special micro-/nano-structures, which is extremely important from the photocatalysis point of view. To enhance the photoactivity of perovskite-based photocatalysts, different modifications of ABO₃-photocatalysts have been performed to optimize the absorption of photons and excitation of the photogenerated charge carriers, separation and migration of the photogenerated charge carriers, and redox reactions during the photocatalytic reaction.

However, to better understand the properties of ABO₃-materials and their role in photocatalysis processes, novel preparation methods need to be developed. Additionally, perovskite oxides have not yet been applied as commercial photocatalysts; therefore, in the future, researchers must pay much attention to obtaining more efficient photocatalysts for industrial use. Moreover, perovskite photocatalytic mechanisms and relationships among the structure, surface photoelectric character and photocatalytic activity have been poorly understood and investigated. Photoluminescence spectrum and surface photovoltage spectroscopy should be used to investigate the photophysics of excited states, providing some important information, such as surface oxygen vacancy and defect, surface states and charge separation and/or recombination processes, which are of great significance to photocatalytic reaction. Finally, studies that investigate the correlation between the fer-

roelectric, ferromagnetic, and piezoelectric properties; electronic structure of perovskites; and photocatalytic activity of these materials should be more widely and thoroughly undertaken.

Acknowledgements

This work was supported by Ministry of Science and Higher Education (contract No.: UMO-0132/IP2/2015/73).

References

- [1] A. Fujishima, *Nature* 238 (1972) 37–38.
- [2] A. Cybula, G. Nowaczyk, M. Jarek, A. Zaleska, *J. Nanomater.* 2014 (2014) 1–9.
- [3] A. Zaleska, *Recent Patents Eng.* 2 (2008) 157–164.
- [4] J. Reszczyńska, T. Grzyb, J.W. Sobczak, W. Lisowski, M. Gazda, B. Ohtani, A. Zaleska, *Appl. Catal. B-Environ.* 163 (2015) 40–49.
- [5] J. Santiago-Morales, A. Agüera, M. del Mar Gómez, A.R. Fernández-Alba, J. Gimeno, S. Esplugas, R. Rosal, *Appl. Catal. B-Environ.* 129 (2012) 13–29.
- [6] H. Shi, T. Zhang, T. An, B. Li, X. Wang, *J. Colloid Interf. Sci.* 380 (2012) 121–127.
- [7] H.G. Yang, G. Liu, S.Z. Qiao, C.H. Sun, Y.G. Jin, S.C. Smith, J. Zou, H.M. Cheng, G.Q. Lu, *J. Am. Chem. Soc.* 131 (2009) 4078–4083.
- [8] X. Wang, S. Sun, Z. Huang, H. Zhang, S. Zhang, *Int. J. Hydrog. Energy* 39 (2014) 905–916.
- [9] D. Dolat, S. Mozia, B. Ohtani, A. Morawski, *Chem. Eng. J.* 225 (2013) 358–364.
- [10] L. Graziani, E. Quagliarini, F. Bondioli, M. D'Orazio, *Build. Environ.* 71 (2014) 193–203.
- [11] L. Liu, S. Lin, J. Hu, Y. Liang, W. Cui, *Appl. Surf. Sci.* 330 (2015) 94–103.
- [12] C.-Y. Chen, J.-C. Weng, J.-H. Chen, S.-H. Ma, K.-H. Chen, T.-L. Horng, C.-Y. Tsay, C.-J. Chang, C.-K. Lin, J.J. Wu, *Powder Technol.* 272 (2015) 316–321.
- [13] W. Cui, W. An, L. Liu, J. Hu, Y. Liang, *Appl. Surf. Sci.* 319 (2014) 298–305.
- [14] A. Kudo, *Catal. Surv. Asia* 7 (2003) 31–38.
- [15] J. Navio, M. Hidalgo, G. Colon, S. Botta, M. Litter, *Langmuir* 17 (2001) 202–210.
- [16] J. Shi, L. Guo, *Progr. Nat. Sci.: Mater. Int.* 22 (2012) 592–615.
- [17] H. Tanaka, M. Misono, *Curr. Opin. Solid State Mater. Sci.* 5 (2001) 381–387.
- [18] A. Bhalla, R. Guo, R. Roy, *Mater. Res. Innov.* 4 (2000) 3–26.
- [19] T.K. Townsend, N.D. Browning, F.E. Osterloh, *Energy Environ. Sci.* 5 (2012) 9543–9550.
- [20] R. Konta, T. Ishii, H. Kato, A. Kudo, *J. Phys. Chem. B* 108 (2004) 8992–8995.
- [21] H.-C. Chen, C.-W. Huang, J.C. Wu, S.-T. Lin, *J. Phys. Chem. C* 116 (2012) 7897–7903.
- [22] H. Kato, Y. Sasaki, N. Shirakura, A. Kudo, *J. Mater. Chem. A* 1 (2013) 12327–12333.
- [23] Y. Jia, S. Shen, D. Wang, X. Wang, J. Shi, F. Zhang, H. Han, C. Li, *J. Mater. Chem. A* 1 (2013) 7905–7912.
- [24] K. Maeda, *ACS Appl. Mater. Interfaces* 6 (2014) 2167–2173.
- [25] H. Zhang, G. Chen, Y. Li, Y. Teng, *Int. J. Hydrog. Energy* 35 (2010) 2713–2716.
- [26] Y. Qu, W. Zhou, Z. Ren, S. Du, X. Meng, G. Tian, K. Pan, G. Wang, H. Fu, *J. Mater. Chem.* 22 (2012) 16471–16476.

- [27] L. Li, Y. Zhang, A.M. Schultz, X. Liu, P.A. Salvador, G.S. Rohrer, *Catal. Sci. Technol.* 2 (2012) 1945–1952.
- [28] L. Ni, M. Tanabe, H. Irie, *Chem. Commun.* 49 (2013) 10094–10096.
- [29] M. Li, J. Zhang, W. Dang, S.K. Cushing, D. Guo, N. Wu, P. Yin, *Phys. Chem. Chem. Phys.* 15 (2013) 16220–16226.
- [30] Z. Zhao, R. Li, Z. Li, Z. Zou, *J. Phys. D: Appl. Phys.* 44 (2011) 165401.
- [31] X. Zhou, J. Shi, C. Li, *J. Phys. Chem. C* 115 (2011) 8305–8311.
- [32] P. Kanhere, P. Shenai, S. Chakraborty, R. Ahuja, J. Zheng, Z. Chen, *Phys. Chem. Chem. Phys.* 16 (2014) 16085–16094.
- [33] M. Marchelek, B. Bajorowicz, P. Mazierski, A. Cybula, T. Klimczuk, M. Winiarski, N. Fijałkowska, A. Zaleska, *Catal. Today* 252 (2014) 47–53.
- [34] X. Liu, J. Lv, S. Wang, X. Li, J. Lang, Y. Su, Z. Chai, X. Wang, *J. Alloys Compd.* 622 (2015) 894–901.
- [35] J. Liu, G. Chen, Z. Li, Z. Zhang, *Int. J. Hydrog. Energy* 32 (2007) 2269–2272.
- [36] H. Shi, X. Li, H. Iwai, Z. Zou, J. Ye, *J. Phys. Chem. Solids* 70 (2009) 931–935.
- [37] Q.-P. Ding, Y.-P. Yuan, X. Xiong, R.-P. Li, H.-B. Huang, Z.-S. Li, T. Yu, Z.-G. Zou, S.-G. Yang, *J. Phys. Chem. C* 112 (2008) 18846–18848.
- [38] G. Li, T. Kako, D. Wang, Z. Zou, J. Ye, *Dalton Trans.* (2009) 2423–2427.
- [39] R. Konta, H. Kato, H. Kobayashi, A. Kudo, *Phys. Chem. Chem. Phys.* 5 (2003) 3061–3065.
- [40] Y. Sang, L. Kuai, C. Chen, Z. Fang, B. Geng, *ACS Appl. Mater. Interfaces* 6 (2014) 5061–5068.
- [41] K. Parida, K. Reddy, S. Martha, D. Das, N. Biswal, *Int. J. Hydrog. Energy* 35 (2010) 12161–12168.
- [42] S. Thirumalaairajan, K. Girija, N.Y. Hebalkar, D. Mangalaraj, C. Viswanathan, N. Ponpandian, *RSC Adv.* 3 (2013) 7549–7561.
- [43] Z.-X. Wei, Y. Wang, J.-P. Liu, C.-M. Xiao, W.-W. Zeng, *Mater. Chem. Phys.* 136 (2012) 755–761.
- [44] F. Gao, X. Chen, K. Yin, S. Dong, Z. Ren, F. Yuan, T. Yu, Z. Zou, J.M. Liu, *Adv. Mater.* 19 (2007) 2889–2892.
- [45] Y.-N. Feng, H.-C. Wang, Y.-D. Luo, Y. Shen, Y.-H. Lin, *J. Appl. Phys.* 113 (2013) 146101.
- [46] C. Madhu, M.B. Bellakki, V. Manivannan, *Indian J. Eng. Mater. Sci.* 17 (2010) 131–139.
- [47] D.Q. Fei, T. Hudaya, A.A. Adesina, *Catal. Commun.* 6 (2005) 253–258.
- [48] M. Misono, *Catal. Today* 144 (2009) 285–291.
- [49] M. Misono, *Studies in Surface Science and Catalysis*, in: M. Makoto (Ed.), Elsevier, 2013, pp. 67–95.
- [50] L.G. Tejuca, J.L.G. Fierro, J.M.D. Tascón, in: D.D. Eley, Herman Pines, Paul B. Weisz (Eds.), *Advances in Catalysis*, Academic Press, 1989, 2015, pp. 237–328.
- [51] J. Zhu, H. Li, L. Zhong, P. Xiao, X. Xu, X. Yang, Z. Zhao, J. Li, *ACS Catal.* 4 (2014) 2917–2940.
- [52] P. Kanhere, Z. Chen, *Molecules* 19 (2014) 19995–20022.
- [53] R.K. Nath, M. Zain, A.A.H. Kadhumi, *Adva. Nat. Appl. Sci.* 6 (2012) 1030–1035.
- [54] G. Parravano, *J. Chem. Phys.* 20 (1952) 342–343.
- [55] G. Parravano, *J. Am. Chem. Soc.* 75 (1953) 1497–1498.
- [56] U. Lüders, Q.-R. Li, R. Feyerherm, E. Dudzik, *J. Phys. Chem. Solids* 75 (2014) 1354–1360.
- [57] S. Acharya, J. Mondal, S. Ghosh, S. Roy, P. Chakrabarti, *Mater. Lett.* 64 (2010) 415–418.
- [58] J. ZHU, N. ZHANG, J.-I. ZHONG, S.-s. TONG, *Ind. Catal.* 3 (2006), 011.
- [59] W. Zhang, J. Tang, J. Ye, *J. Mater. Res.* 22 (2007) 1859–1871.
- [60] W. Zhang, J. Tang, J. Ye, *Chem. Phys. Lett.* 418 (2006) 174–178.
- [61] Z.-X. Wei, Y.-Q. Xu, H.-Y. Liu, C.-W. Hu, *J. Hazard. Mater.* 165 (2009) 1056–1061.
- [62] M. Biswas, *J. Alloys Compd.* 480 (2009) 942–946.
- [63] Y. Li, S. Yao, W. Wen, L. Xue, Y. Yan, *J. Alloys Compd.* 491 (2010) 560–564.
- [64] R. Maiti, S. Basu, D. Chakravorty, *J. Magn. Magn. Mater.* 321 (2009) 3274–3277.
- [65] P. Dhanasekaran, N. Gupta, *Int. J. Hydrog. Energy* 37 (2012) 4897–4907.
- [66] S. Tijare, S. Bakardjieva, J. Subrt, M. Joshi, S. Rayalu, S. Hishita, N. Labhsetwar, *J. Chem. Sci.* 126 (2014) 517–525.
- [67] Y. Zhang, J. Yang, J. Xu, Q. Gao, Z. Hong, *Mater. Lett.* 81 (2012) 1–4.
- [68] L. Jia, J. Li, W. Fang, *J. Alloys Compd.* 489 (2010) L13–L16.
- [69] N. Kondo, H. Itoh, M. Kurihara, M. Sakamoto, H. Aono, Y. Sadaoka, *J. Alloys Compd.* 408 (2006) 1026–1029.
- [70] S. Thirumalaairajan, K. Girija, I. Ganesh, D. Mangalaraj, C. Viswanathan, A. Balamurugan, N. Ponpandian, *Chem. Eng. J.* 209 (2012) 420–428.
- [71] C. Mao, X. Wu, J.-J. Zhu, *J. Nanosci. Nanotechnol.* 8 (2008) 3203–3207.
- [72] L. Mai, L. Xu, Q. Gao, C. Han, B. Hu, Y. Pi, *Nano Lett.* 10 (2010) 2604–2608.
- [73] D. Aman, T. Zaki, S. Mikhail, S. Selim, *Catal. Today* 164 (2011) 209–213.
- [74] A. Giannakas, A. Ladavos, P. Pomonis, *Appl. Catal. B-Environ.* 49 (2004) 147–158.
- [75] F.-t Li, Y. Liu, R.-h Liu, Z.-m Sun, D.-s Zhao, C.-g Kou, *Mater. Lett.* 64 (2010) 223–225.
- [76] L. Gan, L. Zhang, H. Chan, C. Chew, B. Loo, *J. Mater. Sci.* 31 (1996) 1071–1079.
- [77] M. Popa, J. Frantti, M. Kakihana, *Solid State Ionics* 154 (2002) 437–445.
- [78] D. Wang, X. Chu, M. Gong, *Nanotechnology* 17 (2006) 5501.
- [79] H.-T. Fan, X.-J. Xu, X.-K. Ma, T. Zhang, *Nanotechnology* 22 (2011) 115502.
- [80] S. Nakayama, *J. Mater. Sci.* 36 (2001) 5643–5648.
- [81] N.A. Tien, O. Almjashveha, I.Y. Mittova, O. Stognei, S. Soldatenko, *Inorg. Mater.* 45 (2009) 1304–1308.
- [82] Z. Yuan, Y. Wang, Y. Sun, J. Wang, L. Bie, Y. Duan, *Sci. China Ser. B* 49 (2006) 67–74.
- [83] S. Wang, M. Lu, G. Zhou, Y. Zhou, A. Zhang, Z. Yang, *J. Alloys Compd.* 432 (2007) 265–268.
- [84] C.W. Lee, D.W. Kim, I.S. Cho, S. Park, S.S. Shin, S.W. Seo, K.S. Hong, *Int. J. Hydrog. Energy* 37 (2012) 10557–10563.
- [85] P. Tang, Y. Tong, H. Chen, F. Cao, G. Pan, *Curr. Appl. Phys.* 13 (2013) 340–343.
- [86] P. Tang, H. Chen, F. Cao, G. Pan, *Catal. Sci. Technol.* 1 (2011) 1145–1148.
- [87] P. Junpoy, S. Thongtem, T. Thongtem, *Superlattices Microstruct.* 57 (2013) 1–10.
- [88] X. Lü, J. Xie, H. Shu, J. Liu, C. Yin, J. Lin, *Mater. Sci. Eng.: B* 138 (2007) 289–292.
- [89] T. Takei, R. Haramoto, Q. Dong, N. Kumada, Y. Yonesaki, N. Kinomura, T. Mano, S. Nishimoto, Y. Kameshima, M. Miyake, *J. Solid State Chem.* 184 (2011) 2017–2022.
- [90] R. Ramachandran, M. Sathiy, K. Ramesha, A. Prakash, G. Madras, A. Shukla, *J. Chem. Sci.* 123 (2011) 517–524.
- [91] D. Chen, J. Ye, *Chem. Mater.* 19 (2007) 4585–4591.
- [92] C. Li, Y. Zhu, S. Fang, H. Wang, Y. Gui, L. Bi, R. Chen, *J. Phys. Chem. Solids* 72 (2011) 869–874.
- [93] J. Ren, W. Wang, M. Shang, S. Sun, L. Zhang, J. Chang, *J. Hazard. Mater.* 183 (2010) 950–953.
- [94] P. Ju, H. Fan, B. Zhang, K. Shang, T. Liu, S. Ai, D. Zhang, *Sep. Purif. Technol.* 109 (2013) 107–110.
- [95] R.V. Shpanchenko, V.V. Chernaya, A.A. Tsirlin, P.S. Chizhov, D.E. Sklovsky, E.V. Antipov, E.P. Khlybov, V. Pomjakushin, A.M. Balagurov, J.E. Medvedeva, *Chem. Mater.* 16 (2004) 3267–3273.
- [96] J. Xu, C. Hu, Y. Xi, B. Wan, C. Zhang, Y. Zhang, *Solid State Sci.* 14 (2012) 535–539.
- [97] M. Humayun, A. Zada, Z. Li, M. Xie, X. Zhang, Y. Qu, F. Raziq, L. Jing, *Appl. Catal. B-Environ.* 180 (2016) 219–226.
- [98] K. Van Benthem, C. Elsässer, R. French, *J. Appl. Phys.* 90 (2001) 6156–6164.
- [99] H. Zhang, G. Chen, X. He, J. Xu, *J. Alloys Compd.* 516 (2012) 91–95.
- [100] W. Dong, D. Wang, L. Jiang, H. Zhu, H. Huang, J. Li, H. Zhao, C. Li, B. Chen, G. Deng, *Mater. Lett.* 98 (2013) 265–268.
- [101] J. Lu, Y. Jiang, Y. Zhang, J. Huang, Z. Xu, *Ceram. Int.* 41 (2015) 3714–3721.
- [102] X. Tang, K.-a. Hu, *J. Mater. Sci.* 41 (2006) 8025–8028.
- [103] J. Joseph, T. Vimala, V. Sivasubramanian, V. Murthy, *J. Mater. Sci.* 35 (2000) 1571–1575.
- [104] M.S. Hassan, T. Amna, M.-S. Khil, *Ceram. Int.* 40 (2014) 423–427.
- [105] Y.-J. Lin, Y.-H. Chang, G.-J. Chen, Y.-S. Chang, Y.-C. Chang, *J. Alloys Compd.* 479 (2009) 785–790.
- [106] Y. Xin, C.-I. Zhao, Y.-I. Zhou, Z.-j. Wu, J.-m. Yuan, W.-s. Li, *Trans. Nonferrous Metals Soc. China* 25 (2015) 2272–2278.
- [107] H. Eskandarloo, A. Badiei, M.A. Behnadjady, A. Tavakoli, G.M. Ziarani, *Ultrason. Sonochem.* (2015).
- [108] D.P. Dutta, A. Singh, A. Tyagi, *J. Environ. Chem. Eng.* 2 (2014) 2177–2187.
- [109] M. Ahtee, C.N.W. Darlington, *Acta Crystallogr. B36* (1980) 1007–1014.
- [110] C.-C. Hu, H. Teng, *Appl. Catal. A: Gen.* 331 (2007) 44–50.
- [111] H. Wang, F. Wu, H. Jiang, *J. Phys. Chem. C* 115 (2011) 16180–16186.
- [112] T. Zhang, K. Zhao, J. Yu, J. Jin, Y. Qi, H. Li, X. Hou, G. Liu, *Nanoscale* 5 (2013) 8375–8383.
- [113] S.Y. Wu, X.Q. Liu, X.M. Chen, *Ceram. Int.* 36 (2010) 871–877.
- [114] A. Postnikov, V. Caciuc, G. Borstel, *J. Phys. Chem. Solids* 61 (2000) 295–299.
- [115] I. Shein, V. Kozhevnikov, A. Ivanovskii, *arXiv preprint cond-mat/0504286* (2005).
- [116] I. Shein, V. Kozhevnikov, A. Ivanovskii, *Solid State Sci.* 10 (2008) 217–225.
- [117] S. Kittaka, K. Matsuno, H. Akashi, *J. Solid State Chem.* 142 (1999) 360–367.
- [118] S.-y Yan, Y. Xie, T. Liu, H.-t Yu, *J. Phys.: Condens. Matter* 22 (2010) 125501.
- [119] Y. Ueda, N. Nakayama, *Solid State Ionics* 108 (1998) 303–306.
- [120] A. Tsvetkov, F. Mena, P. Van Loosdrecht, D. Van Der Marel, Y. Ren, A. Nugroho, A. Menovsky, I. Elfimov, G. Sawatzky, *Phys. Rev. B* 69 (2004) 075110.
- [121] T. Kako, Z. Zou, M. Katagiri, J. Ye, *Chem. Mater.* 19 (2007) 198–202.
- [122] N. Kumada, N. Kinomura, A. Sleight, *Mater. Res. Bull.* 35 (2000) 2397–2402.
- [123] S. Ishiwata, M. Azuma, M. Takano, E. Nishibori, M. Takata, M. Sakata, K. Kato, *J. Mater. Chem.* 12 (2002) 3733–3737.
- [124] M. Cai, G. Yang, X. Tan, Y. Cao, L. Wang, W. Hu, Y. Wang, *Appl. Phys. Lett.* 91 (2007) 101901.
- [125] T. Kako, N. Kikugawa, J. Ye, *Catal. Today* 131 (2008) 197–202.
- [126] D.J. Singh, Q. Xu, K.P. Ong, *Appl. Phys. Lett.* 104 (2014) 011910.
- [127] J. Henriques, E. Caetano, V. Freire, J. da Costa, E. Albuquerque, *J. Phys.: Condens. Matter* 19 (2007) 106214.
- [128] P. Liu, J. Nisar, B. Pathak, R. Ahuja, *Int. J. Hydrog. Energy* 37 (2012) 11611–11617.
- [129] P. Li, S. Ouyang, G. Xi, T. Kako, J. Ye, *J. Phys. Chem. C* 116 (2012) 7621–7628.
- [130] Y. Zhu, Y. Dai, K. Lai, Z. Li, B. Huang, *J. Phys. Chem. C* 117 (2013) 5593–5598.
- [131] T. Alammari, I. Hamm, M. Wark, A.-V. Mudring, *Appl. Catal. B-Environ.* 178 (2015) 20–28.
- [132] N. Wang, D. Kong, H. He, *Powder Technol.* 207 (2011) 470–473.
- [133] K. Sayama, K. Mukasa, R. Abe, Y. Abe, H. Arakawa, *J. Photochem. Photobiol. A: Chem.* 148 (2002) 71–77.
- [134] C. Cen, S. Thiel, J. Mannhart, J. Levy, *Science* 323 (2009) 1026–1030.
- [135] A. Santander-Syro, O. Copie, T. Kondo, F. Fortuna, S. Pailhes, R. Weht, X. Qiu, F. Bertran, A. Nicolaou, A. Taleb-Ibrahimi, *Nature* 469 (2011) 189–193.
- [136] T. Sun, M. Lu, *Appl. Phys. A* 108 (2012) 171–175.
- [137] S. Burnside, J.-E. Moser, K. Brooks, M. Grätzel, D. Cahen, *J. Phys. Chem. B* 103 (1999) 9328–9332.

- [138] Y. Hu, O. Tan, J. Pan, H. Huang, W. Cao, *Sens. Actuators B: Chem.* 108 (2005) 244–249.
- [139] T. Hara, T. Ishiguro, *Sens. Actuators B: Chem.* 136 (2009) 489–493.
- [140] K. Domen, A. Kudo, T. Onishi, N. Kosugi, H. Kuroda, *J. Phys. Chem.* 90 (1986) 292–295.
- [141] U. Sulaeman, S. Yin, T. Sato, *Appl. Catal. B-Environ.* 105 (2011) 206–210.
- [142] H. Yu, J. Wang, S. Yan, T. Yu, Z. Zou, *J. Photochem. Photobiol. A: Chem.* 275 (2014) 65–71.
- [143] J. Wang, S. Yin, M. Komatsu, T. Sato, *J. Eur. Ceram. Soc.* 25 (2005) 3207–3212.
- [144] T. Cao, Y. Li, C. Wang, C. Shao, Y. Liu, *Langmuir* 27 (2011) 2946–2952.
- [145] J. Liu, G. Chen, Z. Li, Z. Zhang, *J. Solid State Chem.* 179 (2006) 3704–3708.
- [146] W. Xuewen, Z. Zhiyong, Z. Shuixian, *Mater. Sci. Eng.: B* 86 (2001) 29–33.
- [147] T. Klaytae, P. Panthong, S. Thoutom, *Ceram. Int.* 39 (2013) S405–S408.
- [148] U. Selvaraj, A. Prasadara, S. Komarneni, R. Roy, *Mater. Lett.* 12 (1991) 311–315.
- [149] H. Xu, S. Wei, H. Wang, M. Zhu, R. Yu, H. Yan, *J. Cryst. Growth* 292 (2006) 159–164.
- [150] J. Xu, Y. Wei, Y. Huang, J. Wang, X. Zheng, Z. Sun, L. Fan, J. Wu, *Ceram. Int.* 40 (2014) 10583–10591.
- [151] M.-H. Um, H. Kumazawa, *J. Mater. Sci.* 35 (2000) 1295–1300.
- [152] S. Zhang, J. Liu, Y. Han, B. Chen, X. Li, *Mater. Sci. Eng.: B* 110 (2004) 11–17.
- [153] L.F. Da Silva, L.J.Q. Maia, M.I.B. Bernardi, J. Andres, V.R. Mastelaro, *Mater. Chem. Phys.* 125 (2011) 168–173.
- [154] E. Leite, J. Varela, E. Longo, C. Paskocimas, *Ceram. Int.* 21 (1995) 153–158.
- [155] S. Zanetti, E. Longo, J. Varela, E. Leite, *Mater. Lett.* 31 (1997) 173–178.
- [156] C.-H. Chang, Y.-H. Shen, *Mater. Lett.* 60 (2006) 129–132.
- [157] H. Tagawa, K. Igarashi, *J. Am. Ceram. Soc.* 69 (1986) 310–314.
- [158] Q. Pang, J. Shi, M. Gong, *J. Am. Ceram. Soc.* 90 (2007) 3943–3946.
- [159] L.Y.-F.L. Qiong-Yu, Chin. *J. Inorg. Chem.* 6 (2005) 027.
- [160] Z. Zheng, B. Huang, X. Qin, X. Zhang, Y. Dai, *J. Colloid Interface Sci.* 358 (2011) 68–72.
- [161] W. Dong, X. Li, J. Yu, W. Guo, B. Li, L. Tan, C. Li, J. Shi, G. Wang, *Mater. Lett.* 67 (2012) 131–134.
- [162] S.-T. Huang, W.W. Lee, J.-L. Chang, W.-S. Huang, S.-Y. Chou, C.-C. Chen, *J. Taiwan Inst. Chem. Eng.* 45 (2014) 1927–1936.
- [163] K.-Y. Chen, Y.-W. Chen, *Powder Technol.* 141 (2004) 69–74.
- [164] T. Sreethawong, S. Yoshikawa, *Catal. Commun.* 6 (2005) 661–668.
- [165] T. Sreethawong, Y. Suzuki, S. Yoshikawa, *J. Solid State Chem.* 178 (2005) 329–338.
- [166] T. Sreethawong, Y. Yamada, T. Kobayashi, S. Yoshikawa, *J. Mol. Cat. A: Chem.* 241 (2005) 23–32.
- [167] M.M. Yusuf, H. Imai, H. Hirashima, *J. Sol-gel Sci. Technol.* 28 (2003) 97–104.
- [168] K. Cassiers, T. Linssen, K. Aerts, P. Cool, O. Lebedev, G. Van Tendeloo, R. Van Grieken, E.F. Vansant, *J. Mater. Chem.* 13 (2003) 3033–3039.
- [169] T. Puangpetch, T. Sreethawong, S. Yoshikawa, S. Chavadej, *J. Mol. Cat. A: Chem.* 287 (2008) 70–79.
- [170] L. Chen, S. Zhang, L. Wang, D. Xue, S. Yin, *J. Cryst. Growth* 311 (2009) 746–748.
- [171] H. Kato, A. Kudo, *J. Phys. Chem. B* 106 (2002) 5029–5034.
- [172] T. Ishii, H. Kato, A. Kudo, *J. Photochem. Photobiol. A: Chem.* 163 (2004) 181–186.
- [173] H. Yu, S. Ouyang, S. Yan, Z. Li, T. Yu, Z. Zou, *J. Mater. Chem.* 21 (2011) 11347–11351.
- [174] T. Ohno, T. Tsubota, Y. Nakamura, K. Sayama, *Appl. Catal. A: Gen.* 288 (2005) 74–79.
- [175] J. Wang, S. Yin, M. Komatsu, Q. Zhang, F. Saito, T. Sato, *Appl. Catal. B-Environ.* 52 (2004) 11–21.
- [176] J. Wang, S. Yin, M. Komatsu, T. Sato, *J. Eur. Ceram. Soc.* 25 (2005) 3207–3212.
- [177] J. Wang, S. Yin, Q. Zhang, F. Saito, T. Sato, *J. Mater. Chem.* 13 (2003) 2348–2352.
- [178] J. Wang, S. Yin, Q. Zhang, F. Saito, T. Sato, *Solid State Ionics* 172 (2004) 191–195.
- [179] T. Umabayashi, T. Yamaki, H. Itoh, K. Asai, *J. Phys. Chem. Solids* 63 (2002) 1909–1920.
- [180] T. Puangpetch, S. Chavadej, T. Sreethawong, *Energy Convers. Manage.* 52 (2011) 2256–2261.
- [181] R. Niishiro, S. Tanaka, A. Kudo, *Appl. Catal. B-Environ.* 150 (2014) 187–196.
- [182] H. Kato, A. Kudo, *J. Phys. Chem. B* 105 (2001) 4285–4292.
- [183] Z. Zou, J. Ye, H. Arakawa, *Chem. Phys. Lett.* 332 (2000) 271–277.
- [184] H. Kato, A. Kudo, *Chem. Phys. Lett.* 295 (1998) 487–492.
- [185] A. Kudo, H. Kato, *Chem. Phys. Lett.* 331 (2000) 373–377.
- [186] H. Kato, K. Asakura, A. Kudo, *J. Am. Chem. Soc.* 125 (2003) 3082–3089.
- [187] D.G. Porob, P.A. Maggard, *J. Solid State Chem.* 179 (2006) 1727–1732.
- [188] R. Abe, M. Higashi, Z. Zou, K. Sayama, Y. Abe, H. Arakawa, *J. Phys. Chem. B* 108 (2004) 811–814.
- [189] R. Abe, M. Higashi, K. Sayama, Y. Abe, H. Sugihara, *J. Phys. Chem. B* 110 (2006) 2219–2226.
- [190] C. Reitz, K. Brezesinski, J. Haetge, J. Perlich, T. Brezesinski, *RSC Adv.* 2 (2012) 5130–5133.
- [191] F.E. Osterloh, *Chem. Mater.* 20 (2007) 35–54.
- [192] X. Li, J. Zang, *J. Phys. Chem. C* 113 (2009) 19411–19418.
- [193] D. Xu, S. Yang, Y. Jin, M. Chen, W. Fan, B. Luo, W. Shi, *Langmuir* 31 (2015) 9694–9699.
- [194] Y. Lee, T. Watanabe, T. Takata, J.N. Kondo, M. Hara, M. Yoshimura, K. Domen, *Ceram. Mater.* 17 (2005) 2422–2426.
- [195] P. Kanhere, Y. Tang, J. Zheng, Z. Chen, *J. Phys. Chem. Solids* 74 (2013) 1708–1713.
- [196] T. Grewe, K. Meier, H. Tüysüz, *Catal. Today* 225 (2014) 142–148.
- [197] Y. He, Y. Zhu, N. Wu, *J. Solid State Chem.* 177 (2004) 3868–3872.
- [198] M. Zhang, G. Liu, D. Zhang, Y. Chen, S. Wen, S. Ruan, *J. Alloys Compd.* 602 (2014) 322–325.
- [199] B. Wang, P.D. Kanhere, Z. Chen, J. Nisar, B. Pathak, R. Ahuja, *J. Phys. Chem. C* 117 (2013) 22518–22524.
- [200] G. Hitoki, T. Takata, J.N. Kondo, M. Hara, H. Kobayashi, K. Domen, *Chem. Comm.* (2002) 1698–1699.
- [201] H. Bouafia, S. Hiadsi, B. Abidri, A. Akriche, L. Ghalouci, B. Sahli, *Comput. Mater. Sci.* 75 (2013) 1–8.
- [202] P.D. Kanhere, J. Zheng, Z. Chen, *J. Phys. Chem. C* 115 (2011) 11846–11853.
- [203] X. Li, J. Zang, *Catal. Commun.* 12 (2011) 1380–1383.
- [204] L.M. Torres-Martínez, A. Cruz-López, I. Juárez-Ramírez, M.E. Meza-de la Rosa, *J. Hazard. Mater.* 165 (2009) 774–779.
- [205] L. Torres-Martínez, R. Gómez, O. Vázquez-Cuchillo, I. Juárez-Ramírez, A. Cruz-López, F. Alejandro-Sandoval, *Catal. Commun.* 12 (2010) 268–272.
- [206] D.-R. Liu, C.-D. Wei, B. Xue, X.-G. Zhang, Y.-S. Jiang, *J. Hazard. Mater.* 182 (2010) 50–54.
- [207] H. Fu, S. Zhang, L. Zhang, Y. Zhu, *Mater. Res. Bull.* 43 (2008) 864–872.
- [208] Y.-X. Zhao, D.-R. Liu, F.-F. Li, D.-F. Yang, Y.-S. Jiang, *Powder Technol.* 214 (2011) 155–160.
- [209] D.-R. Liu, Y.-S. Jiang, G.-M. Gao, *Chemosphere* 83 (2011) 1546–1552.
- [210] L. Xu, C. Li, W. Shi, J. Guan, Z. Sun, *J. Mol. Cat. A: Chem.* 360 (2012) 42–47.
- [211] P.L. Han, X.J. Wang, Y.H. Zhao, C.H. Tang, *Adv. Mater. Res.* (2009) 1245–1248, Trans Tech Publication.
- [212] W.-H. Lin, C. Cheng, C.-C. Hu, H. Teng, *Appl. Phys. Lett.* 89 (2006), 211904–211904–211903.
- [213] F.-F. Li, D.-R. Liu, G.-M. Gao, B. Xue, Y.-S. Jiang, *Appl. Catal. B-Environ.* 166 (2015) 104–111.
- [214] W. Yang, G. Tan, H. Ren, A. Xia, Y. Luo, L. Yin, *J. Mater. Sci.: Mater. Electron.* 25 (2014) 3807–3815.
- [215] Z. Li, Y. Wang, J. Liu, G. Chen, Y. Li, C. Zhou, *Int. J. Hydrog. Energy* 34 (2009) 147–152.
- [216] X. Wang, H. Bai, Y. Meng, Y. Zhao, C. Tang, Y. Gao, *J. Nanosci. Nanotechnol.* 10 (2010) 1788–1793.
- [217] A. Iwase, H. Kato, A. Kudo, *Appl. Catal. B-Environ.* 136 (2013) 89–93.
- [218] L.M. Torres-Martínez, L.L. Garza-Tovar, M.E. Meza-de la Rosa, A. Martínez-de la Cruz, A. Cruz-López, *Mater. Sci. Forum* (2007) 103–106.
- [219] D. Xu, M. Chen, S. Song, D. Jiang, W. Fan, W. Shi, *CrystEngComm* 16 (2014) 1384–1388.
- [220] B. Bajorowicz, A. Cybula, M.J. Winiarski, T. Klimczuk, A. Zaleska, *Molecules* 19 (2014) 15339–15360.
- [221] W.-P. Tai, J.-G. Kim, J.-H. Oh, C. Lee, D.-W. Park, W.-S. Ahn, *J. Mater. Sci.: Mater. Electron.* 15 (2004) 25–28.
- [222] Y. He, Y. Zhu, N. Wu, *J. Solid State Chem.* 177 (2004) 2985–2990.
- [223] Y. Zou, Y. Hu, H. Gu, Y. Wang, *Chem. Phys.* 115 (2009) 151–153.
- [224] H. Shi, X. Li, H. Iwai, Z. Zou, J. Ye, *J. Phys. Chem. Solids* 70 (2009) 931–935.
- [225] R. Wang, Y. Zhu, Y. Qiu, C.-F. Leung, J. He, G. Liu, T.-C. Lau, *Chem. Eng. J.* 226 (2013) 123–130.
- [226] Y. Guo, K.-i. Kakimoto, H. Ohsato, *Appl. Phys. Lett.* 85 (2004) 4121–4123.
- [227] Z. Cheng, K. Ozawa, M. Osada, A. Miyazaki, H. Kimura, *J. Am. Ceram. Soc.* 89 (2006) 1188–1192.
- [228] V. Shanker, S.L. Samal, G.K. Pradhan, C. Narayana, A.K. Ganguli, *Solid State Sci.* 11 (2009) 562–569.
- [229] G. Li, T. Kako, D. Wang, Z. Zou, J. Ye, *J. Phys. Chem. Solids* 69 (2008) 2487–2491.
- [230] H. Shi, X. Li, D. Wang, Y. Yuan, Z. Zou, J. Ye, *Catal. Lett.* 132 (2009) 205–212.
- [231] N. Chen, G. Li, W. Zhang, *Phys. B: Condens. Matter* 447 (2014) 12–14.
- [232] X. Li, G. Li, S. Wu, X. Chen, W. Zhang, *J. Phys. Chem. Solids* 75 (2014) 491–494.
- [233] G. Li, N. Yang, W. Wang, W. Zhang, *J. Phys. Chem. C* 113 (2009) 14829–14833.
- [234] J. Lv, T. Kako, Z. Li, Z. Zou, J. Ye, *J. Phys. Chem. C* 114 (2010) 6157–6162.
- [235] G. Li, *Mater. Chem. Phys.* 121 (2010) 42–46.
- [236] B. Zielińska, E. Borowiak-Palen, R.J. Kalenczuk, *J. Phys. Chem. Solids* 72 (2011) 117–123.
- [237] H. Kato, H. Kobayashi, A. Kudo, *J. Phys. Chem. B* 106 (2002) 12441–12447.
- [238] S. Mishra, R. Mittal, V.Y. Pomjakushin, S. Chaplot, *Phys. Rev. B* 83 (2011) 134105.
- [239] H. Shi, T. Wang, J. Chen, C. Zhu, J. Ye, Z. Zou, *Catal. Lett.* 141 (2011) 525–530.
- [240] K. Saito, A. Kudo, *Inorg. Chem.* 49 (2010) 2017–2019.
- [241] Z.-P. Liu, P. Hu, *J. Am. Chem. Soc.* 125 (2003) 1958–1967.
- [242] S. Vollmer, G. Witte, C. Wöll, *Catal. Lett.* 77 (2001) 97–101.
- [243] A. Magrez, E. Vasco, J.W. Seo, C. Dieker, N. Setter, L. Forro, *J. Phys. Chem. B* 110 (2006) 58–61.
- [244] L. Jiang, Y. Qiu, Z. Yi, J. Mater. Chem. A 1 (2013) 2878–2885.
- [245] G. Li, T. Kako, D. Wang, Z. Zou, J. Ye, *J. Solid State Chem.* 180 (2007) 2845–2850.
- [246] L. Yan, J. Zhang, X. Zhou, X. Wu, J. Lan, Y. Wang, G. Liu, J. Yu, L. Zhi, *Int. J. Hydrog. Energy* 38 (2013) 3554–3561.
- [247] H. Hayashi, Y. Hakuta, Y. Kurata, *J. Mater. Chem.* 14 (2004) 2046–2051.
- [248] T. Zhang, W. Lei, P. Liu, J.A. Rodriguez, J. Yu, Y. Qi, G. Liu, M. Liu, *Chem. Sci.* (2015).
- [249] L. Yan, T. Zhang, W. Lei, Q. Xu, X. Zhou, P. Xu, Y. Wang, G. Liu, *Catal. Today* 224 (2014) 140–146.

- [250] J. Lan, X. Zhou, G. Liu, J. Yu, J. Zhang, L. Zhi, G. Nie, *Nanoscale* 3 (2011) 5161–5167.
- [251] Z.-Q. Ma, H. Pan, Z.-S. Wang, P.K. Wong, *Int. J. Hydrog. Energy* 40 (2015) 4766–4776.
- [252] J.-P. Zou, L.-Z. Zhang, S.-L. Luo, L.-H. Leng, X.-B. Luo, M.-J. Zhang, Y. Luo, G.-C. Guo, *Int. J. Hydrog. Energy* 37 (2012) 17068–17077.
- [253] H. Zhang, G. Chen, Y. Li, Y. Teng, *Int. J. Hydrog. Energy* 35 (2010) 2713–2716.
- [254] Q. Fu, J. Li, T. He, G. Yang, *J. Appl. Phys.* 113 (2013) 104303.
- [255] H. Mizoguchi, K. Ueda, M. Orita, S.-C. Moon, K. Kajihara, M. Hirano, H. Hosono, *Mater. Res. Bull.* 37 (2002) 2401–2406.
- [256] X. Shu, J. He, D. Chen, *Ind. Eng. Chem. Res.* 47 (2008) 4750–4753.
- [257] H. Wang, X. Zhang, A. Huang, H. Xu, M. Zhu, B. Wang, H. Yan, M. Yoshimura, *J. Crys. Growth* 246 (2002) 150–154.
- [258] M.E. de Anda Reyes, G. Torres Delgado, R. Castaneda Pérez, J. Márquez Marín, O. Zelaya Ángel, *J. Photochem. Photobiol. A: Chem.* 228 (2012) 22–27.
- [259] G. Li, K. Chao, C. Ye, H. Peng, *Mater. Lett.* 62 (2008) 735–738.
- [260] J. Xu, C. Hu, Y. Xi, B. Wan, C. Zhang, Y. Zhang, *Solid State Sci.* 14 (2012) 535–539.
- [261] L.-C. Chen, G.-T. Pan, T.C.K. Yang, T.-W. Chung, C.-M. Huang, *J. Hazard. Mater.* 178 (2010) 644–651.
- [262] X. Hu, C. Hu, J. Qu, *Mater. Res. Bull.* 43 (2008) 2986–2997.
- [263] S.N. Tijare, M.V. Joshi, P.S. Padole, P.A. Mangrulkar, S.S. Rayalu, N.K. Labhsetwar, *Int. J. Hydrog. Energy* 37 (2012) 10451–10456.
- [264] H. Zhang, P. Song, D. Han, Q. Wang, *Phys. E* 63 (2014) 21–26.
- [265] S. Li, L. Jing, W. Fu, L. Yang, B. Xin, H. Fu, *Mater. Res. Bull.* 42 (2007) 203–212.
- [266] H. Su, L. Jing, K. Shi, C. Yao, H. Fu, *J. Nanopart. Res.* 12 (2010) 967–974.
- [267] W. Wang, S. Li, Y. Wen, M. Gong, L. Zhang, Y. Yao, Y. Chen, *Acta Phys.-Chim. Sin.* 24 (2008) 1761–1766.